Generation and characterization of pair photon source for quantum sensing applications

A THESIS

submitted in partial fulfilment of
the requirements for the degree of

Doctor of Philosophy

by

Sandeep Singh
(Roll No. 18330019)

Under the supervision of

Dr. Goutam K. Samanta
Professor
Atomic, Molecular and Optical Physics Division
Physical Research Laboratory, Ahmedabad, India

DISCIPLINE OF PHYSICS

INDIAN INSTITUTE OF TECHNOLOGY GANDHINAGAR

2023

To

My beloved Parents

DECLARATION

I declare that this written submission represents my ideas in my own words, and where others' ideas or words have been included, I have adequately cited and referenced the original sources. I also declare that I have adhered to all principles of academic honesty and integrity and have not misrepresented or fabricated or falsified any idea/data/fact/source in my submission. I understand that any violation of the above can cause disciplinary action by the Institute and can also evoke penal action from the sources which have thus not been properly cited or from whom proper permission has not been taken when needed.

Signature

Date: Sandeep Singh

(Roll No: 18330019)

CERTIFICATE

It is certified that the work contained in the thesis titled **"Generation and characterization of pair photon source for quantum sensing applications"** by Mr. Sandeep Singh (Roll No. 18330019) has been carried out under my supervision, and this work has not been submitted elsewhere for the award of any degree. I have read this dissertation, and it is, in my opinion, totally suitable in breadth and quality as a dissertation for the degree of Doctor of Philosophy.

Date:

Dr. Goutam K Samanta
Professor,
Atomic, Molecular and Optical Physics Division,
Physical Research Laboratory,
Unit of Department of Space, Govt. of India,
Ahmedabad-380009, India.

(Thesis Supervisor)

Acknowledgments

I feel grateful while writing this meticulous section of acknowledgments, allowing me to encapsulate the important instances of support and encouragement received throughout the course of the Ph.D. Throughout my education, many have blazed a trail for me in my quest to earn a Ph.D., but I could not have come this far without the support of a select few. So, I take this opportunity to greatly appreciate their encouragement and assistance.

To begin with, I would like to express my sincere gratitude to my Ph.D. supervisor, Prof. Goutam K. Samanta, for all his guidance, encouragement, and personal support throughout my entire journey of Ph.D. His continuous analysis of my research progress, insightful comments, constructive criticism, and prompt feedback have played an invaluable role in shaping my thesis work. Despite his hectic schedule, he consistently made time to discuss the progress of the projects and provide on-time suggestions. His meticulous efforts ensured that everything I required for my research projects was readily available on time in the lab, enabling me to complete my thesis on time. His understanding, kindness, and generosity in sharing his knowledge of experimental quantum optics have been the most precious part of my learning as a researcher, and I am eternally thankful to him.

I would also like to acknowledge my area chairperson and DSC member, Prof. R. P. Singh, for his kind support and approachability during all the academic formalities. His constructive feedback during the DSC meetings helped me to get peer review feedback on my research projects. I would also like to express my gratitude to my other two DSC members Prof. Navinder Singh and Dr. Naveen Chauhan for all their feedback and interdisciplinary knowledge, which made my DSC meeting worthwhile.

I would like to extend my gratitude to PRL director Prof. Anil Bhardwaj for his gracious efforts in coordinating our student outreach events. Each of the outreach events has offered me a unique blend of experiences that, on the one hand, aided me in honing my managerial, leadership, and pedagogical abilities while also giving me a chance to explore the cultures of various parts of the neighboring states. In addition, I am grateful for his help in coordinating the Student Conference on Optics and Photonics (SCOP), which allows me to network with peers from all around the world. I would also like to thank the PRL academic committee, administrative staff, and the computer center for their help throughout my Ph.D. tenure.

Even though ups and downs are inevitable throughout the rigorous journey of earning a doctorate degree, having supportive friends by your side makes the road less bumpy. Throughout my stay here at PRL, my pals Supriya, Ayushi, Satvika, and Akanksha have been my rock through thick and thin, and I am eternally grateful to them for their care, love, and support. I also appreciate my lab mates for providing me with the ideal balance of professional and personal interactions. I am thankful to Varun, who familiarized me with the lab's working culture and helped me start my first research project. I am grateful for Vimlesh's openness to help me, especially with labview automation and other basic stuff during projects. I appreciate Saumya, Subith, and Anirban; their company always reminds me that work and friendship among colleagues are not mutually exclusive. Our many frequent visits to Akbar bhai and Masti juice will always be one of the best things I remember about living in Ahmedabad, but at the same, I can't deny the cooking skills of Anirban (one-man culinary army). Our trip to Lonavala, along with Anupam and Kamli (the explorer), will always be a treasured memory. I would like to thank Chahat, Shreya, and Bharath for their common understanding.

Without the assistance and support of my family, none of this would have been feasible. I have succeeded this far hugely due to my parents' unwavering support throughout my life, particularly in my pursuit of higher education. Simply expressing gratitude for my parents' contributions to my life and success would be insufficient. Even the heaviest of words are merely insufficient; moreover, I cannot find the vocabulary rich enough to express my exact emotions, but I truly owe them a huge debt of gratitude.

Abstract

Quantum sensing and metrology have emerged as rapidly growing fields, offering unparalleled precision and accuracy in measuring physical parameters. These quantum-based technologies have surpassed classical physics-based approaches and have enabled the measurement of various key quantities such as electric fields, magnetic fields, temperature, and pressure with unprecedented levels of precision. Among different quantum sensing techniques, Hong-Ou-Mandel (HOM) interferometry has gained significant prominence due to its ease of development, implementation, and sensitivity to photon group delay rather than phase shifts.

The basic principle of HOM interferometry relies on the generation and manipulation of indistinguishable paired photons. Typically, the paired photon is generated through a second-order nonlinear optical process called spontaneous parametric down-conversion (SPDC) and indistinguishable in all degrees-of-freedom incident on a balanced beam splitter, they always bunched together through one of the output ports, resulting in the phenomenon known as the HOM dip. This dip in the interference pattern provides valuable information about the relative optical delay between the photons and allows for measuring various properties, including the group index of dispersive materials. Due to the intrinsic dispersion cancellation, HOM interferometry is utilized to sense the characteristic parameters of a sample material, enabling high-resolution imaging of surface features, depth profiling of different layers, and the measurement of group index variations.

However, for reliable and fast sensing with high accuracy and resolution, the indistinguishable photon source must have high brightness, broad spectral bandwidth, and stability against external perturbations. To address these requirements, we have optimized the generation and coupling of paired photons into single-mode fibers. Carefully selecting the periodically poled KTP (PPKTP) crystal due to their high parametric gain, we have achieved high generation rates of indistinguishable paired photons. The coupling efficiency was optimized by adjusting the spot size of the coupling photons. By

employing a 30 mm long PPKTP crystal, we have coupled paired photons at rates as high as 1692 kHz/mW with a maximum efficiency of 32%. We have also observed that one cannot simultaneously access the highest pair collection efficiency and the highest coincidence counts. Therefore, depending on the need and available resources, one can find the trade-off between the overall coincidence counts and the pair coupling efficiency.

We have also addressed the stability of the paired photon source. The control of phase-matching parameters in the SPDC process allows manipulation of various characteristics of the paired photons but also makes the source sensitive to small changes in pump wavelength, crystal temperature, and axial orientation. To enhance stability, we have devised a novel system architecture by developing a hybrid linear and nonlinear approach. A lens-axicon pair, combined with nonlinear crystals like PPKTP and BiB3O6, we have increased the source's tolerance to environmental perturbations while maintaining spectral brightness. This solution enables robust quantum sources suitable for any quantum optics experiments outside lab conditions.

Having achieved high pair photon coupling efficiency and robustness against external perturbations, we used the robust paired photon source in HOM interferometry-based quantum sensing applications. The resolution of HOM interferometry is determined by the spectral bandwidth of the indistinguishable photons. While ultrafast lasers have traditionally been used to achieve broad spectral bandwidth, they are not suitable for in-field applications. To overcome this limitation, we have used a single-frequency continuous-wave diode laser to generate down-converted photons with broad spectral bandwidth. By adjusting the length of the nonlinear crystal in the SPDC process, we have controlled the spectral bandwidth of the down-converted photons. This approach enabled high-precision, real-time sensing of static displacements of 60 nm and vibrations with sub-micron amplitudes and frequencies up to 8 Hz. Using Fisher information analysis; we successfully measured the vibrations with nanometer-scale precision limited by the Cramer Rao bound. The high brightness of the paired photon source allowed for faster statistics-driven measurements compared to previous approaches.

With the successful measurement of fast-changing optical delays between pair photons and improved precision and long dynamic range, we used the HOM interferometry technique to measure the temperature-dependent group index of nonlinear crystals. Using a 1 mm PPKTP crystal producing paired photons, we measured the temperature-dependent group index of a PPKTP crystal sample with a precision on the order of 10^{-6} per centimeter of sample length. This precision exceeded previous achievements by over 400%. We enhanced the measurement range without compromising precision by compensating for the temperature-induced changes in the group index using an optical delay stage. Experimentally we have measured the group index variation of PPKTP with a precision of approximately 10^{-6} over a temperature variation up to 200°C. These findings have implications for quantum optical coherence tomography, enabling high-precision and long-range measurements in this field.

Keywords: Nonlinear optics, spontaneous parametric down-conversion, quantum sensing, Hong-Ou-Mandel interferometry, quantum optical coherence tomography

Abbreviations

BS	Beam Splitter
PBS	Polarisation Beam Splitter
QWP	Quarter Wave Plate
HWP	Half Wave Plate
SMF	Single Mode Fiber
MMF	Multi Mode Fiber
FC	Fiber Coupler
SPDC	Spontaneous Parametric Down Conversion
EMMCD	Electron Multiplying Charged Coupled Device
ICCD	Intensified Charged Coupled Device
QKD	Quantum Key Distribution
EPS	Entangled Photon Source
HOMI	Hong Ou Mandel Interference
QPM	Quasi-Phase Matching
BPM	Birefringence-Phase Matching
PPKTP	Periodically-Poled Potassium Titanyl Phosphate
PPLN	Periodically-Poled Lithium Niobate
QKD	Quantum Key Distribution
SPCM	Single Photon Counting Module
SPS	Single Photon Source
HSPS	Heralded Single Photon Source
SLM	Spatial Light Modulator
FI	Fisher Information
MLE	Maximum Likelihood Estimator
CRB	Cramér Rao Bound
PEA	Piezo Electric Actuator
QOCT	Quantum Optical Coherence Tomography

Contents

List of Publications

Journal Publications

Included in thesis

1. **S. Singh***, V. Kumar, V. Sharma, D. Faccio, G. K. Samanta, “Near-Video Frame Rate Quantum Sensing Using Hong–Ou–Mandel Interferometry”. Adv Quantum Technol. 2023, 6, 2300177.

2. **S. Singh***, V. Kumar, A. Ghosh, A. Forbes, G. K. Samanta, “A Tolerance-Enhanced Spontaneous Parametric Downconversion Source of Bright Entangled Photons”. Adv Quantum Technol. 2023, 6, 2200121.

3. **S. Singh***, V. Kumar and G. K. Samanta,“Fast measurement of group index variation with ultimate precision using Hong-Ou-Mandel interferometry”, ***arXiv:2401.11853 [quant-ph]***

4. **S. Singh***, V. Kumar and G. K. Samanta,“Photon pair coupling efficiency in quasi-phase-matched non-linear crystal”, ***Under preparation***

Not included in thesis

1. V. Kumar, V. Sharma, **S. Singh**, S. Chaitanya Kumar, A. Forbes, M. Ebrahim-Zadeh, and G. K. Samanta, *“Imaging inspired characterization of single-photon carrying orbital angular momentum”* AVS Quantum Sci. 4, 015001 (2022)

Selected Conference papers

1. **S. Singh***, V. Kumar, V. Sharma, D. Faccio, and G. K. Samanta, "Hong-Ou-Mandel interferometry for high precision sensing of real-time vibrations," in Frontiers in Optics + Laser Science 2023 (FiO, LS), Technical Digest Series (Optica Publishing Group, 2023), paper JTu5A.58.

2. **S. Singh***, V. Kumar, A. Ghosh, G.K. Samanata, *"Generation of downconverted photons in a "perfect" annular ring insensitive to the change in phase-matching"*, in Frontiers in Optics / Laser Science 2022 (FIO, LS), Technical Digest Series (Optica Publishing Group, 2022), paper JW5A.29.

3. **S. Singh***, V. Sharma, V. Kumar, and G. K. Samanta, *"Variation of the Hong-Ou-Mandel interference dip with crystal length"*, 2021 Conference on Lasers and Electro-Optics Europe & European Quantum Electronics Conference. (CLEO/Europe-EQEC), 2021, pp. 1-1,

4. V. Kumar*, V. Sharma, **S. Singh**, and G. K. Samanta, *"Direct observation of topological charge of a single photon using a tilted-lens commonly used for classical vortex beams"*, in Frontiers in Optics / Laser Science, B. Lee, C. Mazzali, K. Corwin, and R. Jason Jones, eds., OSA Technical Digest (Optica Publishing Group, 2020), paper JTu1A.27.

5. V. Kumar*, V. Sharma, **S. Singh**, and G. K. Samanta, *"Divergence of single photons with different orbital angular momentum"*, in 2021 Conference on Lasers and Electro-Optics Europe and European Quantum Electronics Conference, OSA Technical Digest (Optica Publishing Group, 2021), paper eb_p_27.

List of Figures

List of Tables

Chapter 1

Introduction

The field of optics, however, dates back centuries, but we really began to appreciate the behavior of light in the 19th century when a British physicist James Clerk Maxwell, presented it in a very concise manner in the form of four partial differential equations, now famously known as Maxwell equations [1]. In these equations, the electric and magnetic fields appear as continuous variables dependent on each other, suggesting a wave nature of light. However, at the beginning of the 20th century, the experimental observations of the photoelectric effect made by Albert Einstein proposed the need to consider light as if it is made of some sort of particle. These are not the usual material particles we observe in our daily life but some kind of compromise between the wave and particle character [2]. Later these particles of light were termed photons by G. N. Lewis [3]. The formal treatment of quantizing the electromagnetic field performed by P. A. M. Dirac suggested the photon be the fundamental excitation of the quantized electromagnetic field [4]. The aspect of optics fundamentally utilizes the quantized electromagnetic field known as the field of quantum optics. In 1935, Albert Einstein, Boris Podolsky, and Nathan Rosen questioned the quantum mechanical description of physical reality as this theory led to the origin of quantum entanglement. Rather unsatisfied with the non-deterministic behavior of nature proposed by quantum theory, the trio proposed the idea of hidden variables which can provide a deterministic behavior of natural phenomenons. The idea of hidden variables was put forward as a possible way to explain the apparent randomness and non-locality observed in quantum phenomena [5].

However, in 1965 John Stewart Bell, through his mathematical formulation, found that the outcomes proposed by the hidden variable theory were completely incompatible with the quantum theory [6]. He proposed a mathematical inequality now famously known as Bell's inequality, which involves a set of measurements to be performed on the entangled particles to confirm the non-local correlations between them. Inspired by Bell's inequality in 1969, Clauser et. al. performed experiments using atom spin systems and demonstrated the violations of hidden variable theory experimentally [7, 8]. The work on the experimental tests on quantum entanglement and its applications in various fields was further demonstrated by Alain Aspect [9] and Anton Zellinger [10]. One of the most widely known approaches to preparing correlated photons in various degrees-of-freedom is spontaneous parametric down-conversion (SPDC) in a second-order nonlinear optical medium. Recent technological advancements have significantly improved the quantum efficiencies of single-photon detectors and non-linear crystals with higher coefficients of non-linearity and have spurred the applications of SPDC in various fields of quantum information processing such as quantum communication [11], quantum imaging [12], to test fundamental laws of quantum mechanics [13], quantum cryptography [14].

One of the frontier fields of quantum information processing, utilizing the extreme sensitivity of quantum systems against environmental perturbations to achieve measurement precision better than the classical methods, is quantum sensing. In connection with Hong-Ou-Mandel interferometry and paired photon generated from SPDC, quantum sensing gives rise to the emerging field of quantum optical coherence tomography (QOCT). It is a technique used for high-resolution imaging of biological specimens or a dispersive medium. Empowered with the dispersion cancellation features of SPDC photons, QOCT outperforms its classical counterpart, which has a measurement resolution no higher than 10^{-3}. It is observed experimentally that the measurement outcomes of QOCT are significantly influenced by the properties of the paired photons employed in the experiment. For optimal performance of QOCT, it is essential for an all-complete pair photon source to possess a combination of three key characteristics: a high photon count rate, superior measurement resolution, and high stability. However, previous methodologies have solely focused on addressing these challenges individually, failing to provide a comprehensive solution that simultaneously satisfies all three requirements [15–17]. In this thesis, we attempted to address all three key problems.

1.1 Thesis structure

The primary objective of this thesis is to generate and characterize SPDC-based pair-photon sources for various quantum sensing applications. This thesis is organized into seven chapters; to accomplish the goal of better quantum sensing using pair photons generated through the SPDC process. We have individually addressed all three aforementioned issues present in the earlier configuration of quantum sensing. Figure 1.1 shows the flowchart of the approach involved in the thesis to achieve an all-completer solution of pair photon source for quantum sensing applications. To provide a better perspective on the field, we have discussed the fundamental principles and theoretical framework to understand non-linear optics, spontaneous parametric down-conversion, pair photon source, and Hong-Ou-Mandel interferometry in the second chapter.

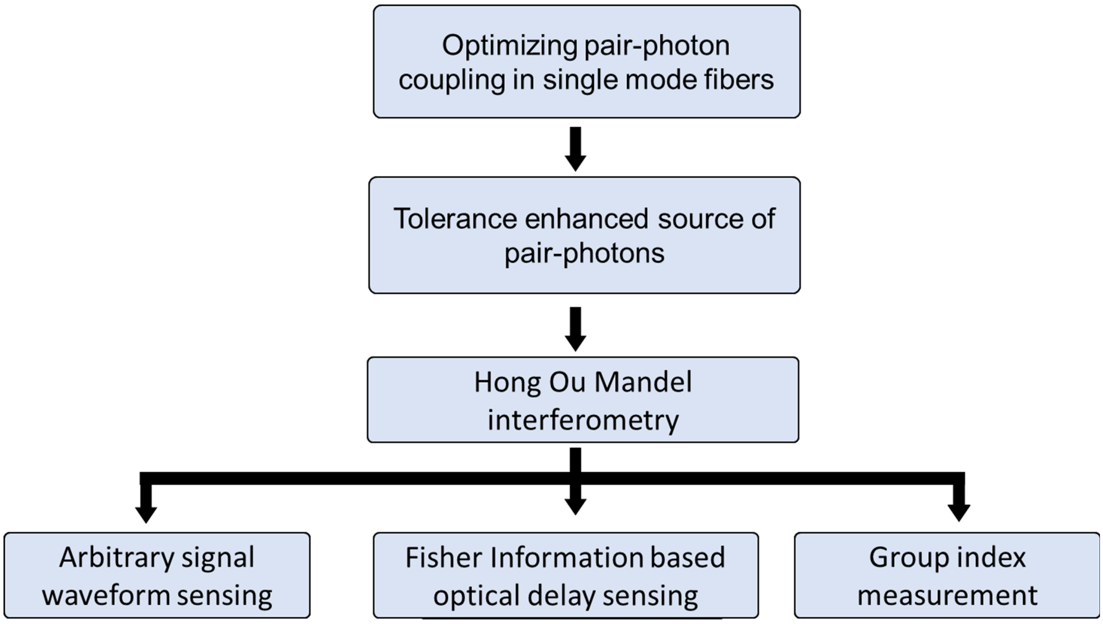

Figure 1.1: Flow chart of thesis structure

Chapter 3 is dedicated to meeting the first objective of improving the pair photon rate and their coupling efficiency into single-mode fibers. We have first studied various parameters affecting the pair photon rate and photon pair coupling efficiency in periodically-poled non-linear (e.g., PPKTP) crystal designed for quasi-phase matching criterion. The motivation behind choosing the PPKTP crystal is its high non-linear gain of the PPKTP, but still, there is not much in-depth study on the factors affecting the photon pair coupling efficiency in periodically poled crystals. We have studied how the various parameters of quasi-phase matching conditions, such as crystal temperature, pump beam spot size, and the collection beam spot size, affect the photon pair coupling efficiency. It is observed that both the pump intensity at the crystal center and the divergence of the SPDC photons play a crucial role in the collection of pair photons into single-mode fibers. By controlling these parameters, we can optimize the pair photon pair in single photon fibers. While the pair coupling efficiency is majorly controlled by the divergence of the pump and, thus, the divergence of SPDC photons. The rate of generation of photons does not seem to alter the pair coupling efficiency. This conclusion supports the experimental observation that for a fixed collection beam waist, the pump beam waist providing the maximum pair coupling efficiency is different from the providing maximum coincidence counts. Crystal temperature is another parameter that can be utilized to change the radius of the SPDC ring and, thus, the photon density at the fiber coupler. It is observed that a linear decrease in the radius of the SPDC ring provides a quadratic increase in the pair photon rate collected by single-mode fibers and becomes highest near the collinear geometry of SPDC.

Next, in Chapter 4, we have addressed the issue of the stability of the pair photons. The phase-matching parameters of the SPDC process give the freedom to control the various parameters of the entangled photons. This versatility derives from the simple manipulation and control of the different characteristics of down-converted photons, such as wavelength, polarization, and spatial geometry, by adjusting the phase-matching parameters of nonlinear interactions, such as temperature, crystal inclination, and pump wavelength. Nonetheless, this adaptable control over the various parameters of down-converted photons renders the SPDC process sensitive to small changes in pump wavelength, crystal temperature, and crystal axial orientation. Such intolerance for fluctuating environmental factors prohibits the deployment of SPDC-based sources in non-ideal environments outside of laboratory settings. To address this issue, we developed a novel system architecture based on a hybrid linear and non-linear solution that increases the source's tolerance without diminishing its spectral brightness. This linear solution is a lens-axicon pair, judiciously placed and tested with two common non-linear crystals, quasi-phase-matched periodically-poled KTiOPO4 and birefringent-phase-matched BiB3O6. Such a solution provides a novel approach to deployable high-brightness quantum sources that are environment-resilient, such as in satellite-based quantum applications.

In Chapter 5, we attempted to improve the precision of measurement obtained using Hong-Ou-Mandel interferometry. It is the phenomenon of bunching two indistinguishable photons on a balanced beam splitter. As the photons become completely indistinguishable, the coincidence detection probability of the interfering photons at the two output ports of the balanced beam splitter falls to zero; this decrease in the coincidence counts is referred to in the scientific literature as the HOM dip. The interference dip has an FWHM width proportional to the coherence length of the indistinguishable photons bunching on the beam splitter or inversely proportional to their spectral bandwidth. It is generally accepted that the resolution of any quantum sensing measurement utilizing HOM interference is constrained by the width of the HOM dip. Consequently, the spectral bandwidth of interfering pair photons has a significant impact on the resolution of HOM-based sensors. The requirement of indistinguishable photons is generally fulfilled through the parametric down conversion by employing ultrashort pulse lasers so that the broad spectral bandwidth of the pump photons can be translated to the down-converted photons. However, these lasers are highly expensive and bulky in size, limiting their use in space-constrained environments. We address this issue by using a much more economical and small-sized single-frequency, continuous-wave diode laser to generate down-converted photons with broad spectral bandwidth. Using the length of the non-linear crystal as a control parameter, the spectral bandwidth of the down-converted photons is altered. Later we used broad spectrum indistinguishable photons in connection with HOM interferometry for high-precision, real-time sensing of static displacements and vibrations with sub-micron amplitudes and up to 8 Hz frequency. In addition, we have incorporated the use of Fisher information to measure vibrations with a precision limited by the Cramer Rao bound.

In Chapter 6, the precision-enhanced HOM interference technique developed in the previous study can be used to measure the small optical delays introduced between the interfering indistinguishable photons, which in turn tells us the information of the physical parameter related to the optical delay. One such physical parameter is the group index, which is a characteristic parameter of a dispersive material and a measure of the group velocity of light traveling through it. The group index has a wide range of applications in material characterization, optical coherence tomography, and fiber optics. Specifically, to shape single-mode operation in high-power optical fibers, a precise understanding of the optical properties of the gain medium is required. This necessitates accurate measurements of the group index of the core of the optical fiber and the difference in refractive index (n) between the core and cladding of the fiber. We used HOM interferometry in connection with broadband photons to measure the precise optical delays introduced by the group index of some non-linear crystals, which in turn can be used as a pointer to measure the group index of the material.

Finally, in Chapter 7, we have concluded the thesis by providing an exhaustive and insightful future outlook on the presented research thesis.

Chapter 2

Fundamental Principles

This chapter offers a thorough introduction to the prominent field of heralded single-photon sources (HSPS) based on the spontaneous parametric downconversion (SPDC) process. In the first section, we will explore the fundamental conditions required for the SPDC process and the various important characteristics of the SPDC photons. In addition, we will investigate its application in the design of a robust entangled photon source, as well as the phase-matching parameters that influence both the qualitative and quantitative characteristics of HSPS. In subsequent sections, we will examine the use of HSPS in Hong Ou Mandel (HOM) interferometry. With knowledge of both the qualitative as well as quantitative components of HOM interferometry, we will investigate its application in precision augmented sensing of optical delays.

2.1 Single photon source

A photon is usually defined as the quanta of an electromagnetic (EM) field or a fundamental excitation of the quantized EM field[18]. A single photon originating from the field quantized mode $\nu_{k,\mu}$ has an energy of $h\nu_{k,\mu}$ where h is the Plank's constant and k, μ are the wave-vector and z-component of the photon spin. The monochromatic definition of a photon necessitates the temporal delocalization of single-photon states. But in reality, the single-photon states are localized in both time and space to a certain extent. Such kind of single-photon states can be realized in terms of the superposition of monochromatic photon modes[19]. In the field of experimental quantum optics, the operational definition of a single photon state is defined in the following manner: given a single-photon detector capable of measuring the number of incident single photons (having some finite frequency bandwidth) with a quantum efficiency of unity, a single-photon state (localized to some degree in both space and time) is an excitation of the EM field that the detector counts exactly one photon for each incident state[20]. In other words, a single photon state can be defined as one whose photon number statistics has mean photon number one and variance of zero[21]. However, in realistic conditions, the losses in the measurement procedure must be taken into account while determining the photon number statistics.

The major driving factor for research in the field of single photon sources (SPSs) is the rapid growth in the area of quantum information science over the last few decades[22]. These techniques utilizing quantum information science based on the principle of quantum mechanics are capable of outperforming their classical counterparts. SPSs are one of the key ingredients of the experimental procedures exploring the immense potential of quantum information science. Some of the broad areas of research demanding SPSs are the quantum internet[23, 24], a fundamentally secure global quantum network[25], quantum cryptography[26], quantum random number generators [14, 27], quantum metrology [12, 28]. In addition to the fundamental research in quantum information science, SPSs are also useful in a wide range of applications such as DNA sequencing[29–32], bio-luminescence detection[33], light detection and ranging (LIDAR) for remote sensing[34, 35], picosecond imaging circuit analysis[36, 37], optical time domain reflectometry[38, 39], single-molecule spectroscopy[40, 41] and bio-medical applications such as optical coherence tomography[42].

2.1.1 Deterministic single-photon source

An ideal single-photon source would be one where a single photon can be emitted at any user-defined arbitrary time (one can say that the source is deterministic or ”on-demand”), the probability of emitting a single photon is 100% while of multiple photons is 0%, subsequent photons are completely indistinguishable in nature, and the rate of emission can be set to any speed with an upper limit determined by the temporal with of the photon wave-packets[43]. In realistic situations, the single photon sources usually have some deviations from these ideal traits, which are always taken into account while planning the experimental procedures and the analysis of the outcomes. Depending upon the working mechanism of a single photon source, it can be categorized as either deterministic (or "on demand") or probabilistic in nature. Some of the widely used deterministic single-photon sources are based on quantum dots[44–46], color centers[47, 48], single ions[49], single atoms[50]. However, all of these methods employ a unique material framework but work on almost similar operational principles. When single-photon emission is desired, external control is used to place the system in an excited state that emits a single photon upon relaxation to a lower-energy state. Frequently, optical cavity coupling techniques are used to manipulate the emission characteristics. Though the deterministic SPSs possess high state purity but suffer from lower emissions rates which restricts their use in areas demanding high photon emission rates such as quantum imaging and quantum communication [20, 51].

2.1.2 Probabilistic single-photon source

The other major branch of single-photon sources is the probabilistic single-photon source. It relies on the parametric down-conversion (PDC) in waveguides[52], bulk optical crystals[53, 54], and four-wave mixing methods in optical fibers[55, 56]. In this case, instead of just a single photon but a pair of photons is created probabilistically rather than deterministically. Due to the fact that photons are generated in pairs, one photon (the heralding photon) can be used to confirm the creation of the other photon (the heralded single photon). Although the deterministic and probabilistic single photon sources can be distinguished in principle based on the inherent generation mechanism, however, in practice, this distinction can get a little blurred. Loss in photon extraction from the deterministic source's region of generation is a major contributory factor to this. As these losses increase, the operation of a source that is principally deterministic becomes more probabilistic. However, the deterministic single-photon sources possess high purity of the single photon states; their low photon generation rate puts a hurdle in practical implementation in some key areas of quantum information processing such as quantum key distribution[57, 58] and quantum imaging[12, 59] which demand a high spectral brightness[11]. The most widely used alternative in these areas is spontaneous parametric down-conversion (SPDC) based single photon sources. In the next section, we will have a comprehensive study of SPDC and its implementation in single and entangled photon sources[11, 60].

2.2 Spontaneous parametric down conversion

Spontaneous Parametric Down Conversion (SPDC) is a nonlinear optical process that occurs in a $\chi^{(2)}$ non-linear crystal. In this case, when a $\chi^{(2)}$ non-linear crystal is illuminated by a pump laser, one of the pump photons splits into two lower-energy daughter photons while obeying energy and momentum conservation. Fig. 2.1 a) shows the pictorial representation of the SPDC process, while 2.1 b), c) depict the energy and momentum conservation, respectively. $\omega_{p,s,i}$ and $\boldsymbol{k}_{p,s,i}$ represents the angular frequency and wave-vector of pump, signal, and idler photons, respectively and p,s and i stands for pump, signal, and idler. These low-energy daughter photons are often referred to as signal and idler photons having high and low energy, respectively. The energy and momentum conservation conditions determine the possible relation between the wave vectors of the two downconverted photons, collectively known as phase-matching conditions (see section phase-matching conditions 2.2.1). SPDC is a quantum counterpart of the difference frequency generation process [61]; if the input field contains the field at frequency ω_s, then generation at $\omega_i = \omega_p - \omega_s$ gets stimulated, and it results in a highly efficient process commonly known as optical parametric amplification. However, in the case of SPDC, this stimulation is provided by the vacuum modes present at ω_s owing to quantum vacuum fluctuations, which makes this process very inefficient. Even in state-of-the-art experimental conditions, only 1 out of 10^6 photons gets down converted[62]. Fig. 2.1 (b) depicts the energy level diagram for the SPDC process. A pump photon of frequency ω_p gets absorbed by the non-linear medium and excited to a virtual state. This excited state, later on, gets stimulated by a vacuum mode present

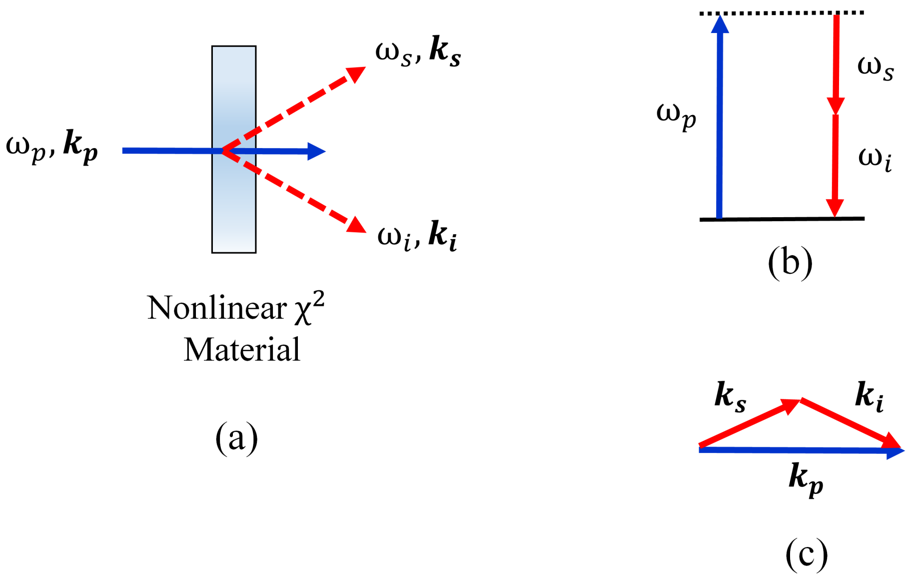

Figure 2.1: a) pictorial representation of the parametric down-conversion process in a $\chi^{(2)}$ non-linear medium, b),c) pictorial representation of the energy and momentum conservation between the pump and down-converted photons

at (ω_s) and decays to the ground state, which results in two down-converted photons. Fig. 2.1 (c) demonstrates the ideal case of momentum conservation between the pump and down-converted photons; however, a momentum mismatch is always observed under experimental conditions. The constraints imposed by energy and momentum conservation entangle the two downconverted particles in various degrees of freedom, including position-momentum [63, 64], angular position-orbital angular momentum [65, 66], polarization [64, 67], and energy-time [68].

First theoretical predictions of SPDC were made by Louisell et al. in 1961 [69], but its application as a source of non-classical light was first suggested by Zeldovich and Klyshko in 1969 [70]. The first experimental observations of SPDC were recorded in 1970 by taking notice of coincidences between the photons produced by an ammonium dihydrogen phosphate crystal pumped by a 325-nm He-Cd laser[71]. However, its potential was only fully realized till the beginning of the 1990s. Since then, this procedure has been at the center of several quantum optics experiments for applications of quantum communication [11, 60], quantum metrology [72], quantum cryptography

[14], and quantum computing [73], to test fundamental laws of quantum mechanics [13], quantum teleportation [10], quantum lithography [74], entangled photon source [60], indistinguishable photons [75].

SPDC process is second order non-linear process which occurs only in $\chi^{(2)}$-non-linear, electrically anisotropic crystals, such as periodically poled potassium titanyl phosphate or commonly known as PPKTP [11, 60]. The interaction of pump photons with the non-linear crystal induces a non-linear polarization wave in the non-linear medium. The instantaneous value of this non-linear polarization can be related to electric displacement vector $\boldsymbol{D}(\boldsymbol{r},t)$[1] inside the non-linear crystal as follows; [62, 76];

$$\boldsymbol{D}(\boldsymbol{r},t) = \varepsilon_{\circ}\boldsymbol{E}(\boldsymbol{r},t) + \boldsymbol{P}(\boldsymbol{r},t) \tag{2.1}$$

where $\boldsymbol{P}(\boldsymbol{r},t)$ is the polarization induced in the medium, $\varepsilon_{\circ}$ is the permittivity of free space, and $\boldsymbol{E}(\boldsymbol{r},t)$ represents the electric field of the pump field in the crystal. In the presence of strong pump field strength in the non-linear crystal, the polarization also has higher order contributions, which can be written as a power series in terms of $\boldsymbol{E}(\boldsymbol{r},t)$ as follows:

$$\begin{aligned}\boldsymbol{P}(\boldsymbol{r},t) &= \varepsilon_{\circ}\chi^{(1)}\boldsymbol{E}(\boldsymbol{r},t) + \varepsilon_{\circ}\chi^{(2)}\boldsymbol{E}(\boldsymbol{r},t)\boldsymbol{E}(\boldsymbol{r},t) + \varepsilon_{\circ}\chi^{(3)}\boldsymbol{E}(\boldsymbol{r},t)\boldsymbol{E}(\boldsymbol{r},t)\boldsymbol{E}(\boldsymbol{r},t) + \ldots \\ &= \boldsymbol{P}^{(1)}(\boldsymbol{r},t) + \boldsymbol{P}^{(2)}(\boldsymbol{r},t) + \boldsymbol{P}^{(3)}(\boldsymbol{r},t) + \ldots\end{aligned} \tag{2.2}$$

where $\chi^{(1)}$ is the linear susceptibility, while $\chi^{(2)}$ and $\chi^{(3)}$ are known as second- and third-order non-linear susceptibilities respectively. Similarly $\boldsymbol{P}^{(1)}$ is the linear polarization while $\boldsymbol{P}^{(2)}$ and $\boldsymbol{P}^{(3)}$ are called as second-order and third-order non-linear polarization respectively. Generally the value of $\chi^{(2)}$ and $\chi^{(3)}$ is 12 and 24 orders of magnitude smaller than the $\chi^{(1)}$, which makes $\chi^{(2)}$ and $\chi^{(3)}$ non-linear effects considerable only at high optical field strengths [62]. In the case of SPDC, we are only concerned with $\chi^{(2)}$ optical non-linearity, so the second-order non-linear polarization can be explicitly

[1] bold symbol is preserved for the vector quantity

written in electric field components of the applied fields as follows;

$$\boldsymbol{P}_l^{(2)} = \varepsilon_\circ \chi^2_{lmn} (\boldsymbol{E})_m (\boldsymbol{E})_n \tag{2.3}$$

Here χ^2_{lmn} is the second-order susceptibility tensor of the crystal medium, while l,m, and n are the cartesian coordinates [77]. Using Eq. 2.3 and Ref. [78, 79], interaction Hamiltonian for the interaction among pump, signal, and idler photons can be written in spherical polar coordinates as follows;

$$H_I(t) = \int_V \chi^2_{lmn} \boldsymbol{E}_p(\boldsymbol{r,t})_l \boldsymbol{E}_s(\boldsymbol{r,t})_m \boldsymbol{E}_i(\boldsymbol{r,t})_n d^3\boldsymbol{r} \tag{2.4}$$

The integration extends over the entire region of the non-linear crystal. Due to the fact that the down-conversion process depends on the polarizations of the pump, signal, and idler fields, the above equation is written employing the vectorial nature of the electric fields. Nevertheless, working with vectorial fields complicates the calculations considerably. So we can first determine the allowed combinations of polarization states for the signal, idler, and pump photons and then calculate the detection probabilities for the down-converted photons using the scalar fields for each combination. In order to do so, the Eq. 2.4 can be rewritten as follows;

$$H_I(t) = \int_V \chi^2 E_p(\boldsymbol{r,t}) E_s(\boldsymbol{r,t}) E_i(\boldsymbol{r,t}) d^3\boldsymbol{r} \tag{2.5}$$

where $E_p(\boldsymbol{r,t})$, $E_s(\boldsymbol{r,t})$ and $E_i(\boldsymbol{r,t})$ represents the scaler electric fields for the permitted combination of polarizations for the pump, signal, and idler fields and χ^2 represents the element of the second-order non-linearity tensor for this combination of polarizations. In the interaction picture of the quantum formalism, Eq. 2.5 can be rewritten as follows

$$\hat{H}_I(t) = \int_V \chi^2 \hat{E}_p(\boldsymbol{r,t}) \hat{E}_s(\boldsymbol{r,t}) \hat{E}_i(\boldsymbol{r,t}) d^3\boldsymbol{r} \tag{2.6}$$

Where $\hat{E}_p$, $\hat{E}_s$ and $\hat{E}_i$ represents the field operators for the pump signal and idler fields. Employing the formalization of complex analytic signal representation, each field operator can be expressed in terms of its positive and negative frequency components[80].

In addition, keeping in view the fact that SPDC is a very weak process, which signifies that the pump intensity is several orders higher than the signal and idler fields, the pump field can be treated classically [81]. In addition, energy conservation permits only particular combinations of these field operators, which ultimately results in the following expression of the interaction Hamiltonian;

$$
\begin{aligned}
\hat{H}_I(t) = \varepsilon_\circ \chi^2 \boldsymbol{A}_p \boldsymbol{A}_s^* \boldsymbol{A}_i^* \int_V d^3\mathbf{r} \iiint d\omega_p d\omega_s d\omega_i \\
\times \iiint d^2\boldsymbol{q}_p d^2\boldsymbol{q}_s d^2\boldsymbol{q}_i V(\omega_p, \boldsymbol{q}_p) \\
\times \exp\left[i(\boldsymbol{q}_p - \boldsymbol{q}_s - \boldsymbol{q}_i)\cdot\boldsymbol{\rho} + i(k_{pz} - k_{sz} - k_{iz})z\right] \\
\times e^{(i(\omega_s)+\omega_i-\omega_p)t}\hat{a}^\dagger(\boldsymbol{q}_s, \omega_s)\hat{a}^\dagger(\boldsymbol{q}_i, \omega_i) + H.c.
\end{aligned}
\tag{2.7}
$$

where $\boldsymbol{A}_{p,s,i}$ is a constant parameter related to the electric field amplitudes for the pump, signal, and idler fields, respectively. $\boldsymbol{k} = (k_x, k_y, k_z) = (\boldsymbol{q}, k_z)$, where $\boldsymbol{q}$ is the projection of wave-vector lying in a plane transverse to the direction of the propagation of the field. $\hat{a}^\dagger(\boldsymbol{q}_s, \omega_s)$ and $\hat{a}^\dagger(\boldsymbol{q}_i, \omega_i)$ are the creation operators for the signal and idler fields respectively. Eq. 2.7 shows a general form of the interaction Hamiltonian for the parametric down-conversion process. Now to derive a general form of the state of the generated photons through the SPDC process, let us consider a $\chi^{(2)}$-non-linear crystal of interaction length L (see Fig. 2.2) interacting with pump field at ω_p. With the assumption that the pump photon begins interacting with the non-linear medium at time t = t_o and at that instant of time, the state $|\psi(-t_0)\rangle$ of the down-converted photons can be expressed in terms of the vacuum modes given by $|\psi(-t_0)\rangle = |vac\rangle_s |vac\rangle_i$. So, the output state of SPDC at time t = 0 can be written as follows;

$$
|\psi(0)\rangle = -\frac{i}{\hbar}\int_{-t_0}^{0} \hat{H}_I(t)dt\,|\psi(-t_0)\rangle \tag{2.8}
$$

Here the third and higher-order perturbation terms representing the states of four- and higher-photon fields are neglected since their generation probability is negligible [81]. Now by substituting Eq. 2.7 in Eq. 2.8, we can derive the expression for the two-photon state of down-converted photons at the output facet of the non-linear crystal, as

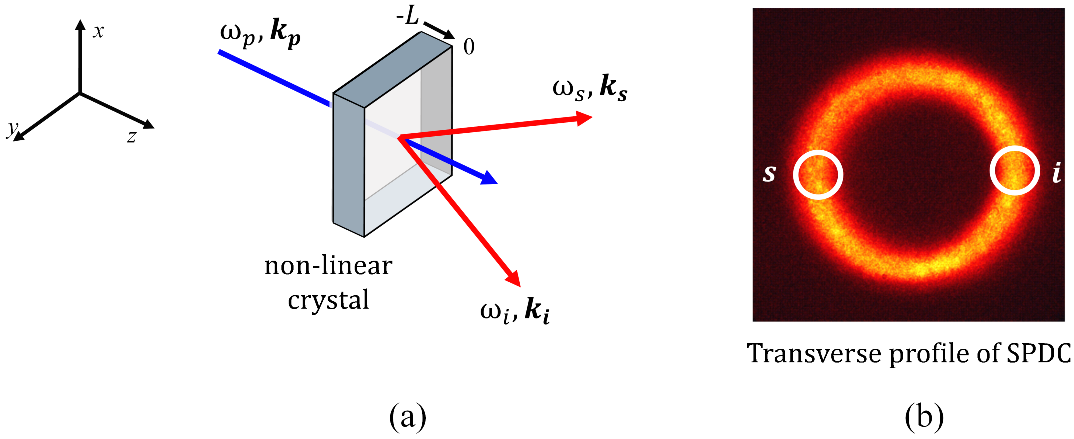

Figure 2.2: a) A conventional experimental configuration for SPDC in a non-linear crystal of interaction length L in the laboratory frame of reference. b) transverse profile of SPDC photons

follows;

$$\begin{aligned} |\psi(0)\rangle = \boldsymbol{A} \iint d\omega_s d\omega_i \iint d^2\boldsymbol{q}_s d^2\boldsymbol{q}_i V(\omega_s+\omega_i, \boldsymbol{s}+\boldsymbol{q}_i) \\ \times \Phi(\omega_s, \omega_i, \boldsymbol{q}_s, \boldsymbol{q}_i) \, |\boldsymbol{q}_s, \omega_s\rangle_s \, |\boldsymbol{q}_i, \omega_i\rangle_i \end{aligned} \tag{2.9}$$

where $A = \frac{\varepsilon_0}{i\hbar}\chi^{(2)}\boldsymbol{A}_p\boldsymbol{A}_s^*\boldsymbol{A}_i^*$. The term $\Phi(\omega_s, \omega_i, \boldsymbol{q}_s, \boldsymbol{q}_i)$ is commonly known as the joint spectral amplitude. In the majority of cases, the pump field is assumed to be a Gaussian beam, and the location of its beam waist is assumed to coincide with the center of the crystal. The spatial and spectral characteristics of the SPDC process are greatly affected by the pump beam parameters, such as the location of the pump beam w.r.t to the center of the crystal, a spatial distribution profile of the pump, effective interaction length of the non-linear crystal [59, 82–85]. Fig. 2.2 (b) demonstrates the transverse profile of SPDC photons generated using a 30mm PPKTP in the laboratory. The two circular white rings on the two diametrically opposite points of the SPDC ring indicate the positions of a correlated signal and idler photons. The radius of the SPDC ring can be altered by adjusting crystal parameters, such as crystal temperature. [60].In the following section, we will discuss the phase-matching conditions of the SPDC procedure in greater depth.

2.2.1 Phase matching

The constraints imposed by the conservation of energy and momentum, as appear in Eq. 2.10 and 2.11, govern the generation and emission directions of SPDC photons, customarily known as phase-matching conditions [62].

$$\hbar\omega_p = \hbar\omega_s + \hbar\omega_i \tag{2.10}$$

$$\boldsymbol{k}_p = \boldsymbol{k}_s + \boldsymbol{k}_i \tag{2.11a}$$

$$\Delta\boldsymbol{k} = \boldsymbol{k}_p - \boldsymbol{k}_s - \boldsymbol{k}_i \tag{2.11b}$$

On the basis of the propagation direction of the pump and down-converted photons, it is essentially divided into collinear and non-collinear phase matching categories. In collinear phase matching (Fig. 2.3(a)), the signal and idler photons propagate in the same direction as the pump photon, while, in non-collinear phase matching (Fig. 2.3(b)), the signal and idler photons propagate in different directions w.r.t the pump photons. In principle, momentum conservation imposes that Eq.2.11a has to be satisfied for the SPDC to occur. But in realistic experimental conditions, there is always a finite amount of momentum mismatch, $\Delta\boldsymbol{k}$, between the pump and down-converted photons (Eq. 2.11b), which must be taken into account while designing an experiment. The phase-matching diagrams in the light of finite momentum-mismatch between the pump and down-converted photons can be depicted as shown in Fig. 2.3 (c) and (d). This finite amount of $\Delta\boldsymbol{k}$ results in a finite width of the spatial distribution (Gaussian in collinear and annular in non-collinear case) of downconverted photons, as can be verified from Fig. 2.3(e) and (f). These images depict the experimental observations of the intensity profiles of the SPDC ring generated using a 30mm PPKTP crystal.

These phase-matching constraints are both advantageous and restrictive at the same time. The emitted SPDC photons are highly directional (can be predicted from the

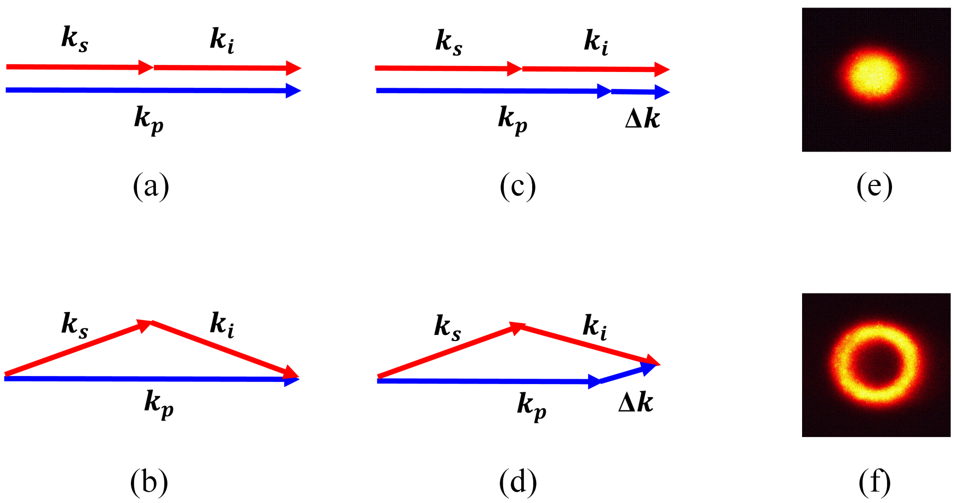

Figure 2.3: (a) and (c) represent ideal and experimental phase-matching diagrams for collinear emission geometries, while (c) and (d) represents the same for non-collinear emission geometries. (e) and (f) represents the experimental observations of the transverse profile of the down-converted photons in collinear and non-collinear geometries.

momentum conservation), which is advantageous for the majority of applications in which optical alignment plays a highly crucial role [11, 60]. Disadvantageous in that the inherent dispersion of transparent non-linear crystal is generally intractable, thereby limiting the spatial and spectral properties of down-converted photons [86]. These phase-matching constraints can be surmounted in different methods, which can broadly be classified into birefringence [81] and quasi-phase matching techniques [11, 60, 87]. There are three types of polarization phase-matching techniques possible in SPDC; type-I, where both down-converted photons have the same polarization but orthogonal to the pump photons, type-II, where the down-converted photons have orthogonal polarization and type-0, where all the three photons(pump, signal, idler) have the same polarization. However, it is to be noted that type-0 phase-matching can only be achieved using specially engineered periodically poled crystals[62]. From Eq. 2.9, it can be deduced that for a non-linear crystal of length L, the intensity distribution of the downconverted photons may be shown as follows;

$$I_{SPDC} \approx Sinc^2(\Delta kL/2) \tag{2.12}$$

It can easily be inferred from Eq. 2.12 that intensity of the SPDC process will be maximum only when $\Delta k = 0$, i.e., when all the interacting waves are in phase with each other, also shown in Fig. 2.4(a) shows the dependence of the gain of the SPDC process on the total mismatch ($\Delta kL/2$).This momentum mismatch is caused by the wavelength dependence of the index of refraction, which results in different phase velocities for various wavelengths within the medium. It inevitably results in oscillations of the relative phase between the pump and down-converted photons, which in turn results in the oscillations of SPDC intensity (see 2.4(b)) with the crystal length.

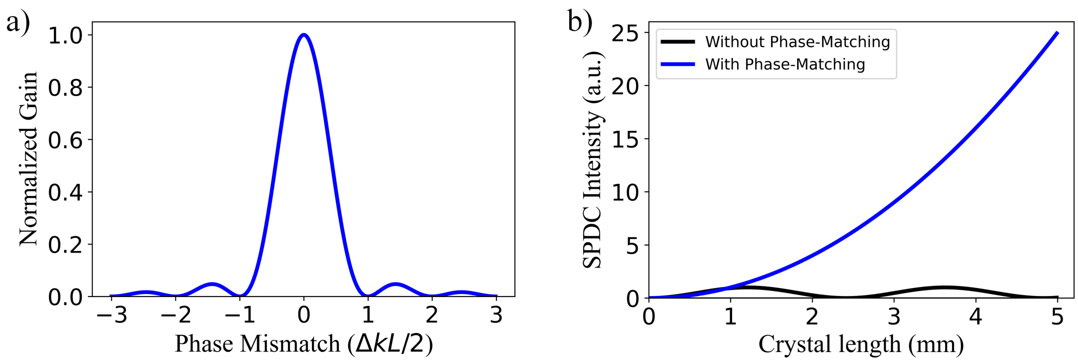

Figure 2.4: Variation of SPDC efficiency with respect to phase mismatch $\Delta kL/2$ (b) Comparison of SPDC efficiency with and without phase-matching conditions

Birefringence phase-matching

Now we have learned that the perfect phase-matching ($\Delta k = 0$) can only be obtained by matching the refractive index for pump and SPDC photons, i.e. ($n_\omega = n_{\omega/2}$). Normal dispersion, wherein the material's refractive index rises with frequency, makes phase matching difficult in the majority of non-linear interactions. Birefringence, on the other hand, could be advantageous in this situation, which states that the refractive index for a polarized wave depends upon its direction of propagation inside the material. So, in the case of BPM, the interacting waves of different frequencies are polarized differently so that their respective phase velocities can be altered using a unique propagation direction in the crystal while their wave vectors satisfy phase-matching conditions [62]. Nonlinear crystals may be uniaxial (one optical axis) or biaxial (two optical axes), depending on the number of anisotropy axes present. All EM waves polarized in a plane transverse to the optical axis and traveling along it will have the same refractive index. We will only consider uniaxial crystals to comprehend BPM for simplicity's sake. Birefringence can be formalized in a uniaxial crystal by designating two distinct refractive indices: the ordinary refractive index (n_o) and the extraordinary refractive index (n_e). The EM wave polarized perpendicular to the optical axis will always experience the ordinary refractive index (n_o), regardless of the direction of propagation, and is known as the ordinary wave. On the other hand, the EM wave polarized orthogonally to the ordinary wave, lying in the plane swept by the optical axis, known as an extra-ordinary wave, will endure a refractive index, $n_e(\theta)$, which depends upon its projection on the optic axis. The refractive index for an extraordinary wave propagating at an angle (θ) w.r.t. optic axis can be written as follows;

$$\frac{1}{\mid n_e(\theta) \mid^2} = \frac{cos^2(\theta)}{n_o^2} + \frac{sin^2(\theta)}{n_e^2} \tag{2.13}$$

The index ellipsoids for positive ($n_o < n_e$) and negative ($n_o > n_e$) uniaxial crystals are shown in Fig. 2.5 a) and b), respectively. Fig. 2.6 a) shows that there exists

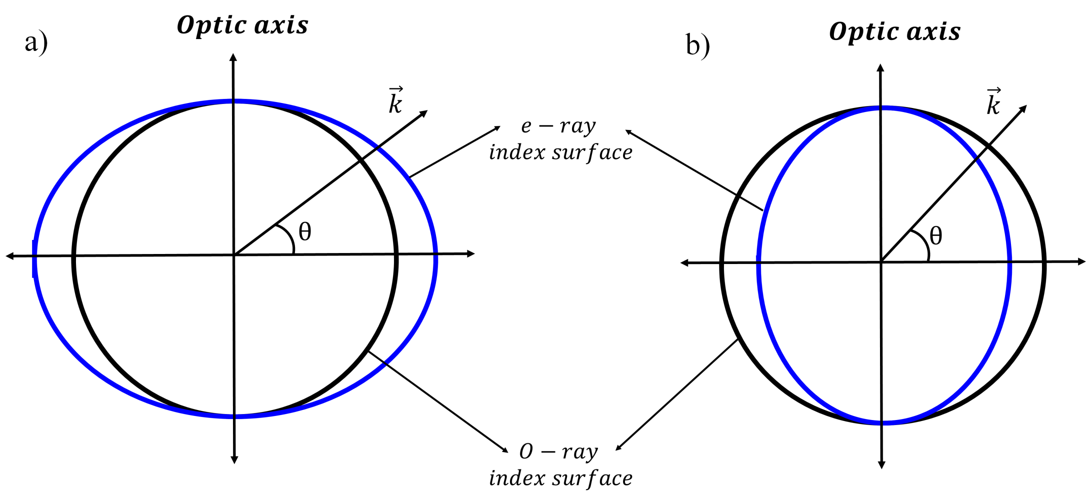

Figure 2.5: Index ellipsoids for (a) positive uniaxial crystals and (b) negative uniaxial crystals.

a propagation direction at an angle (θ) where the refractive index (n_ω^o) of an ordinary wave at frequency, ω, becomes equal to the refractive index ($n^e_{\omega/2}$) of the extraordinary wave at frequency, $\omega/2$. The point of intersection of the index ellipsoid is denoted by a red dot to facilitate comprehension. The same can be inferred from 2.6 b) regarding the BPM for negative uniaxial crystals. The most commonly used $\chi^{(2)}$ non-linear crystals for SPDC generation using BPM are BBO negative (beta barium borate, BaB_2O_4) [81] and BIBO (Bismuth Borate, Bi_3BO_6) [88].

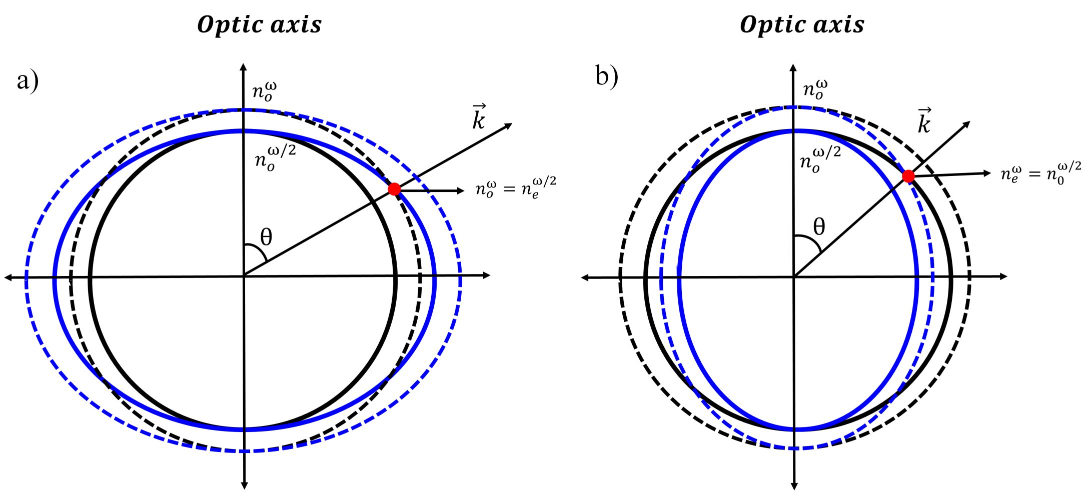

Figure 2.6: An illustration of the BPM for a) positive and b) negative uniaxial crystals.

Quasi phase-matching

Quasi-phase-matching (QPM), developed by Armstrong et al. in 1962 [89], is an alternate method to BPM for correcting the phase mismatch brought on by the chromatic dispersion of the nonlinear crystal. The commonly used crystals for SPDC generation using QPM are potassium titanyl phosphate ($KTiOPO_4$) [11, 60], lithium niobate ($LiNbO_3$) [90]. Unlike BPM, QPM phase matching is not ideal phase-matching technique, as it allows for some phase mismatch between the interacting waves. In the course of interaction in the crystal, as the interacting waves propagate, a distance equivalent to their coherence length (L_c), the phase difference between them becomes π (leads to zero parametric gain) an additional phase difference of π is introduced between the interacting waves, which makes them come into phase once again. This technique maintains gradual power flow from the pump beam to downconverted photons. This extra phase of π is introduced by periodical reversal of the ferroelectric domains of the non-linear crystal [11, 91], which in turn alters the coefficient of nonlinearity of the medium with a period (Λ_g, commonly known as poling period) of twice the coherence length, as shown in Fig.2.7. For an optimum duty factor of 50 %, the effective nonlinearity factor of a first-order QPM is represented as follows; [62]

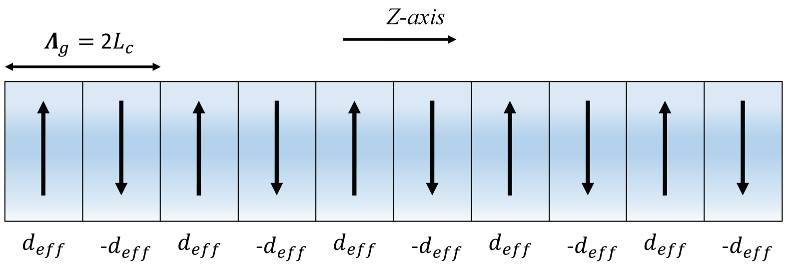

Figure 2.7: side profile of a periodically poled non-linear crystal showing periodic reversion of nonlinear coefficient

$$d_{eff} = \frac{2}{\pi m} d_{ijk} \tag{2.14}$$

In fact, the possibility of all interacting waves being polarized in the same direction outweighs the theoretic decrease of the nonlinear coefficient as it enables access to the largest nonlinear tensor element of the data. The main advantage of QPM is that it can be used for material with minimal birefringence, which can not be used with birefringence phase-matching (BPM). In fact, QPM can be used for non-critical phase matching for any non-linear interaction permitted within the transparency range of the non-linear crystal used.

2.3 Entangled photon source

The SPDC process can be used to produce heralded single-photon source as well as an entangled photons source. The entanglement between the idler and signal photons is primarily caused by vacuum fluctuations and conservation principles. Entanglement is a vital resource for quantum computing and communications and may be produced in a variety of degrees of freedom, including polarization [11, 64, 67], position-momentum [63, 64], energy and time [68], and orbital angular momentum [66, 92], depending on the configuration of the generation process. The signal and idler photons must be generated in at least a two-mode state, such as with horizontal and vertical polarization, to obtain entanglement.

2.3.1 Polarization entanglement

The polarization basis is the most preferred choice to generate entangled pairs due to the relatively easy architecture of the generation and detection techniques of entangled pairs in polarization basis. It can be written in terms of horizontal, $|H\rangle$ and vertical, $|V\rangle$ polarization or right circular, $|R\rangle$ and left circular,$|L\rangle$ polarization or diagonal,$|D\rangle$ and anti-diagonal,$|A\rangle$ polarization. A simple qubit can be written in the polarization bases as follows;

$$|\Psi\rangle = \frac{1}{\sqrt{2}}(|H\rangle + |V\rangle) = \frac{1}{\sqrt{2}}(|R\rangle + |L\rangle) = \frac{1}{\sqrt{2}}(|D\rangle + |A\rangle) \tag{2.15}$$

and their corresponding maximally entangled Bell states can be written as follows;

$$\left|\Phi^{\pm}\right\rangle = \frac{1}{\sqrt{2}}(|HH\rangle \pm |VV\rangle) = \frac{1}{\sqrt{2}}(|RR\rangle \pm |LL\rangle) = \frac{1}{\sqrt{2}}(|DD\rangle \pm |AA\rangle) \tag{2.16a}$$

$$\left|\Psi^{\pm}\right\rangle = \frac{1}{\sqrt{2}}(|HV\rangle \pm |VH\rangle) = \frac{1}{\sqrt{2}}(|RL\rangle \pm |LR\rangle) = \frac{1}{\sqrt{2}}(|DA\rangle \pm |AD\rangle) \tag{2.16b}$$

All four Bell states violate the CHSH Bell's inequality. For entanglement verification of a prepared polarization entangled state, the value of Bell's parameter, S ≥ 2 with an upper bound of $2\sqrt{2}$, while for a separable state S ≤ 2.

2.3.2 Entanglement generation

For type-0 and I SPDC [11, 60], the signal and idler photons are consistently generated with the same polarization, so the output is as follows;

$$|\psi\rangle = |H\rangle_s |H\rangle_i \tag{2.17}$$

However, several experimental configurations, such as a Sagnac cavity [11, 60], can be employed to produce a Bell state out of this state. In contrast, for type II SPDC [93], signal and idlers are generated with orthogonal polarizations, making it possible to acquire an entangled state, which can be written as follows;

$$|\psi\rangle_{ent} = |H\rangle_s |V\rangle_i + |V\rangle_s |H\rangle_i \tag{2.18}$$

Several entanglement-based protocols such as E91 [57], BB92 [94] have been put forward to utilize the potential of quantum entanglement in quantum cryptography through QKD, where 'two parties each share a component of a bipartite entangled state. By exploiting the collapse of the wave function following measurement, which is experimentally measured by an increase in the quantum bit error rate, eavesdropping can be detected. Primarily, the entangled pair is considered to be the most secure method of information transfer because: (i) it is impossible to measure the quantum state of a system without disturbing it; (ii) a single photon cannot be measured partly due to its status as the utmost quanta of electromagnetic radiation (iii) it is impossible to perfectly clone an unknown quantum state as suggested by no-cloning theorem [95, 96]. The amount of information that each qubit can carry during the QKD process increases with the dimensionality of the entangled state. For this goal, other degrees of freedom have also been studied to have information capacity, including space [97], time [98], frequency [99], and orbital angular momentum [66].

2.4 Hong Ou Mandel interferometry

Hong-Ou-Mandel (HOM) interference is a phenomenon in which two indistinguishable photons, incident on the two separate input ports of a balanced beam splitter (50:50), interfere and then emerge out together through one of the output ports [100]. The experimental demonstration of the two-photon interference finds its origin in the profound understanding of the action of a beam splitter (BS), which leads to the coupling between the input and output modes of a BS through a unitary transformation [101, 102]. However, this phenomenon is famously known as Hong-Ou-Mandel interference, but it was reported by Fearn et al. [103] and experimentally observed by Rarity et al. [92, 104] at nearly the same time. To under the basic action of a balance BS, let's denote its two input and output ports a, b and c, d, respectively, as shown in Fig. 2.8 a). By employing the second field quantization formalism, a unitary transformation between the input and output modes can be made as follows;

$$\begin{cases} \hat{a} = \dfrac{\hat{c}+\hat{d}}{\sqrt{2}} \\ \hat{b} = \dfrac{\hat{c}-\hat{d}}{\sqrt{2}} \end{cases} \tag{2.19}$$

Let us consider two photons completely indistinguishable in all degrees of freedom except for their time of arrival, separated by a time τ at the BS. Then using Eq. 2.19 to implement the action of the BS, the output state from the BS can be written as follows;

$$\begin{aligned} \hat{a}_t^\dagger \hat{b}_{t+\tau}^\dagger |0\rangle &\xrightarrow{BS} \frac{1}{2}(\hat{c}_t^\dagger + \hat{d}_t^\dagger)(\hat{c}_{t+\tau}^\dagger - \hat{d}_{t+\tau}^\dagger)|0\rangle \\ &= \frac{1}{2}(\hat{c}_t^\dagger \hat{c}_{t+\tau}^\dagger - \hat{c}_t^\dagger \hat{d}_{t+\tau}^\dagger + \hat{d}_t^\dagger \hat{c}_{t+\tau}^\dagger - \hat{d}_t^\dagger \hat{d}_{t+\tau}^\dagger)|0\rangle \end{aligned} \tag{2.20}$$

Now from Eq. 2.20, we can infer that there are four possibilities of interaction on the BS as shown in Fig. 2.8 b); the first and last terms correspond to the case where both photons emerge out of the same output port, known as bunching, while the middle two terms of Eq. 2.20 refers to the case when the two photons emerge out of the different output ports, known as anti-bunching. The HOM interference occurs only when the

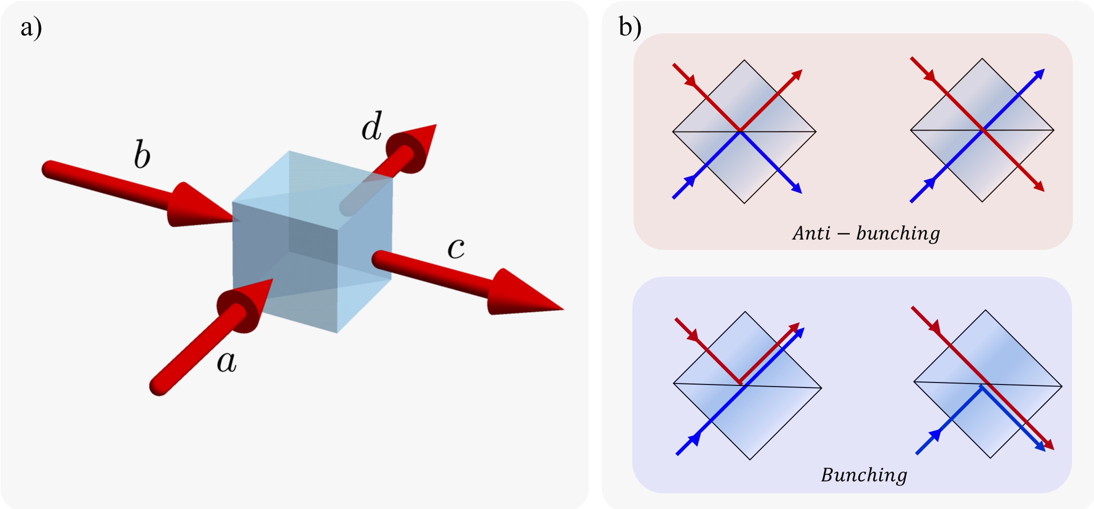

Figure 2.8: a.) A balanced beam splitter with input ports designated a and b, and output ports designated c and d. ,b.) Four possibilities of interaction of two photons at the input ports of BS

two photons are completely indistinguishable in all degrees of freedom, including their time of arrival at the BS. Therefore setting $\tau = 0$ in Eq. 2.20 and using the standard bosonic commutation relations, we get the following expression;

$$\begin{aligned} \hat{a}_t^\dagger \hat{b}_t^\dagger |0\rangle &\xrightarrow{BS} \frac{1}{2}(\hat{c}_t^\dagger \hat{c}_{t+}^\dagger - \cancel{\hat{c}_t^\dagger \hat{d}_t^\dagger} + \cancel{\hat{c}_t^\dagger \hat{d}_t^\dagger} - \hat{d}_t^\dagger \hat{d}_t^\dagger)|0\rangle \\ &= \frac{1}{\sqrt{2}}(|2\rangle_c - |2\rangle_d) \end{aligned} \tag{2.21}$$

The preceding equations lay the groundwork for the Hong-Ou-Mandel (HOM) interference. Physically distinct from the interference of a single photon or classical fields, it is the interference of the two-photon states as a whole that occurs [92, 103]. In this case, we witness destructive interference between the two-photon states that correspond to photons departing through opposite output ports and constructive interference between the two-photon states that correspond to photons exiting through the same output ports [101]. In spite of this, destructive and constructive interference can be modified by modifying the degree of symmetry of the overall two-photon input state [12]. In practical situations, a photon wave packet is localized in space and time to some extent, or in other words, the temporal mode function of the photon has some finite width [20], which can further be related to the coherence time of the interfering photons at the BS.

So, in actual practice, HOM is characterized by a fall in the coincidence probability of the indistinguishable photons at the output of the BS; when the difference between the time of arrival of the photons at the BS is less than the coincidence time of the photon wave packets. This sharp fall in the coincidence counts is famously known as the HOM

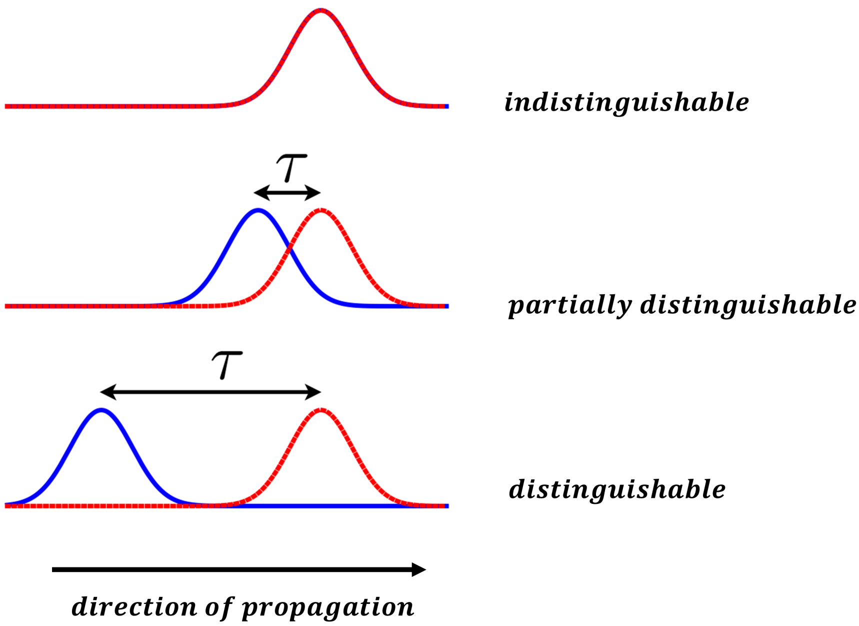

Figure 2.9: Demonstration of the temporal distinguishability of the photon wave-packets having finite temporal widths

dip [100]. The coincidence probability for two photons interfering on the BS is given as follows;

$$P_c = \frac{1}{2} - \frac{1}{2} \int d\omega_1 \mid \phi(\omega_1) \mid^2 e^{-i\omega_1\tau} \int d\omega_2 \mid \phi(\omega_2) \mid^2 e^{i\omega_2\tau} \tag{2.22}$$

Where $\phi(\omega_{1,2})$ and $\omega_{1,2}$ represent the spectral amplitudes functions and the angular frequencies of the two photons, while τ is the temporal gap between the two photons. In case both the photon spectral amplitude function modeled by Gaussian function of equal width, the Eq.2.22 can be simplified as follow [105];

$$P_c = \frac{1}{2} - \frac{1}{2} e^{\frac{\sigma^2\tau^2}{2}} \tag{2.23}$$

Figure 2.10 shows how the coincidence detection rate falls as the photons are made indistinguishable in their time of arrival (in femtoseconds) at the BS ($\tau = 0$). Experimental observations (black dots) are well approximated by the inverted Gaussian profile (solid red line), indicating the temporal mode profile of the photons. The width of the HOM curve is found to be σ = 147.2 femtoseconds.

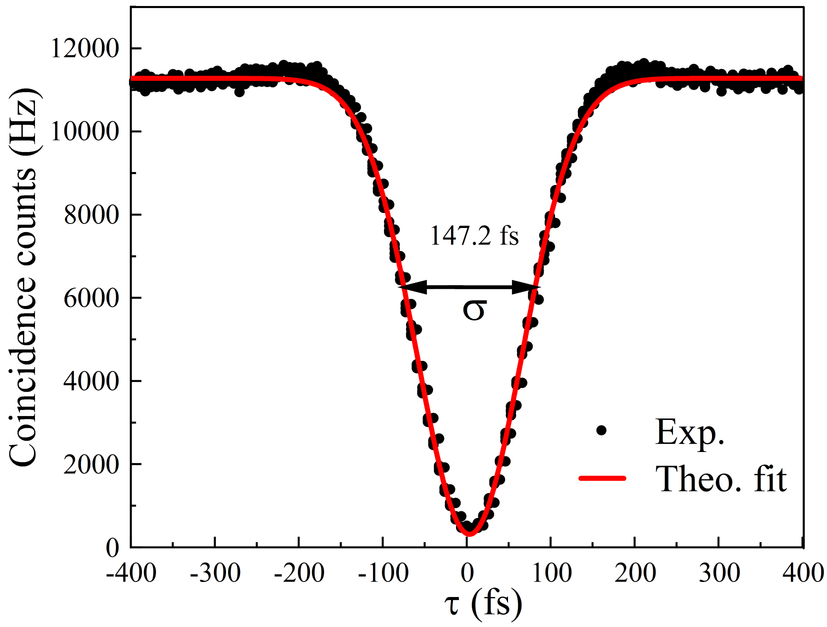

Figure 2.10: Experimental observation of the HOM curve profile

Interference visibility for this HOM curve is 96%; another characteristic parameter related to the mode purity of the interfering photons is the visibility of the interference, which can be calculated using Eq. 2.24.

$$V_{HOM} = \frac{C_{max} - C_{min}}{C_{max}} \tag{2.24}$$

HOM is used in a plethora of applications, including quantum information processing[106–108], plasmonics [109], quantum key distribution [110, 111], quantum metrology [65, 112, 113], precision timing measurements [114–117], quantum optical coherence tomography [118–121], quantum imaging [12, 59], quantum communication

[122], quantum computing [123–126].

2.5 HOM-based quantum sensing

The study of optical phase measurements, as well as other physical parameters related to the optical delay, is covered within the discipline of photonic quantum sensing. It encompasses all those quantum protocols of estimating physical parameters using the laws of quantum physics that can outperform precision and accuracy achieved using any classical techniques[28]. It makes use of crucial quantum phenomena, including squeezed states, single-photon states, and quantum entanglement, which greatly increase the accuracy and precision of measurement. Basically, it exploits the extreme sensitivity of quantum systems to their environmental perturbations. HOM interference is widely used in the field of photonic quantum sensing through the measurement of optical delays with higher precision than its classical counterparts.

Chapter 3

Characterization of spontaneous parametric down-conversion for optimum paired photon rate

3.1 Introduction

In the last two decades, spontaneous parametric down-conversion (SPDC) has emerged as a pivotal tool for generating heralded single photons and entangled photon pairs [127]. It provides a comprehensive solution to produce entangled pairs in various degrees-of-freedom (DOFs) of the photon pairs, such as polarization [11, 60], energy-time [68], position-momentum [64], and angular momentum [66]. This underlying versatility of the SPDC process enables it to be an all-encompassing method to cater to the demand for entangled photon pairs across diverse areas of quantum information processing such as quantum communications [128], quantum sensing [129], quantum imaging [59], and quantum random number generation [130]. The effective implementation of entangled photon sources based on the SPDC process in the aforementioned fields necessitates the requirement of not only high fidelity of the entangled state [131] but also of a substantially high photon rate to attain high signal-to-noise ratio (SNR) [23]. For instance, in the context of free-space quantum key distribution, the high photon rate becomes one of the imperative prerequisites to counterbalance the scattering loss in photon rate caused by atmospheric turbulence [132]. The high photon count also provides an upper hand in achieving fast quantum sensing of subtle optical delays using Hong-Ou-Mandel interferometry [129], fast scanning in quantum optical coherence tomography (QOCT) [133], and better signal-to-noise ratio (SNR) in fast quantum imaging techniques [12, 59].

The final goal of achieving a high rate of paired photons generation based on the SPDC can broadly be addressed through two distinct tasks: first, achieving a high generation rate of down-converted paired photons by playing with the optical gain of the non-linear process, and second, efficient collection of these generated photon pairs by the single-photon detectors. As far as the generation part is concerned SPDC process only takes place in non-centrosymmetric non-linear materials possessing χ^2 non-linearity. The most commonly employed non-linear crystals to generate paired photons are birefringence phase-matched (BPM) β-bismuth borate (BBO) and barium borate (BIBO). These crystals require an additional phase compensating mechanism to generate entangled photon pairs with high quantum state fidelity, which is a somehow achievable task. The major drawback of these crystals is the low generation rate [127]. This is primarily due to their inherent lower nonlinearity coefficient ($d_{eff} \sim 2.2$ - 3.4 pm/V) and the restriction on the increase of effective interaction length due to the spatial walk-off effects [134, 135]. Despite the immense efforts aimed at enhancing the collection of generated photon pair, no considerable improvement has been observed in the effective photon pair rate (see ref. [136]). However, In recent years, an alternative to BPM, quasi-phase-matching (QPM) based periodically poled nonlinear crystals (periodically poled potassium titanyl phosphate (PPKTP) and periodically poled lithium niobate (PPLN), has gained notable interest due to the ease of accessing higher non-linearity coefficients using QPM amid the absence of a spatial walk-off effect. These two key features collectively lead to a substantial increase in the generation rate of paired photons while simultaneously relaxing the restriction on the effective interaction length of the non-linear crystal leading to a further increase in the rate of generation of paired photons with high spectral indistinguishability [11, 60, 137, 138]. Keeping in view

the availability of single photons detectors with high quantum efficiency in the visible region, PPKTP crystal-based type-0, non-collinear, degenerate phase-matching geometry has been demonstrated to provide high photon generation rate along with high quantum state fidelity of the entangled photons. This specific configuration is able to achieve a high non-linear gain for SPDC majorly due to the large effective non-linearity coefficient ($d_{eff} \sim 16.9$ pm/V) of the PPKTP crystal involved[11].
However, having high non-linear gain through the utilization of a specific phase-matching configuration is not enough to ensure a paired photons source with large counts. It is equally important to employ an optimally efficient photon collection mechanism. Again optimal coupling varies with the phase-matching configuration used for photon generation. For example, the experimental conditional for the optimal collection of paired photons generated by birefringent crystals given their spatial walk-off might not be an optimal condition for paired photons generated through type-0, non-collinear phase-matching in PPKTP crystals [127]. While efforts have been made to find optimal conditions to improve generation rate and overall collection efficiency for paired photon sources based on birefringent crystals, no comprehensive study has been conducted to determine the experimental conditions for optimal coupling of generated paired photons in quasi-phase-matched crystals into single mode fibers. Here we present a comprehensive study conducted to examine the effect of pump beam waist (ω_p) and collection beam waist (ω_c) on the coincidence count rate and the paired photon coupling efficiency for type-0, PPKTP crystal based degenerate source. We observed a maximum number of collected coincidence counts of 1692.3 ± 4.1 kHz/mW for ω_p = 42 µm and ω_c = 57 µm at a crystal temperature of 29.5°C. However, the maximum coupling efficiency of 32.1 ± 0.6 % is observed for ω_p = 84 µm and ω_c = 109 µm.

3.2 Collection mechanism

A general approach for the collection of paired photons is achieved through the coupling of photons into fiber through the use of a coupler, basically an objective lens of high numerical aperture housed within a mechanical mount. The single-mode fibers (SMFs) are observed to be a preferred choice, owing to their ability to support the propagation of only a specific spatial mode, known as the fundamental mode. The SMFs maintain high spatial purity of the paired photons as required in certain quantum information processing tasks, including Hong-Ou-Mandel interferometry-based quantum sensing [129], and quantum imaging [23]. Typically the optical fibers are defined in terms of the mode-field diameter (MFD), the width of an irradiance distribution across the end face of a single-mode fiber. To attain high coupling of pair photons into the fiber, the effective diameter of the photon beam must match the MFD of the fiber. To accomplish this goal, the crystal center (region of the crystal having the highest rate of generation of pair photons) needs to be properly imaged on the core of SMF with an appropriate 2f-2f imaging mechanism, comprising of f_2 and f_3, as depicted in Fig. 3.1. Since an SMF has a small enough MFD ($\sim$ 5 µm at 810 nm) to restrict the propagation of higher-order spatial mode, this also necessitates the SMF to have a low numerical aperture (NA, 0.13 at 810 nm). So, it becomes essential that the pair photons to be coupled should be within the numerical aperture of the SMF in order to ensure efficient coupling. In practical scenarios, as shown in Fig. 3.1, the clear aperture of the

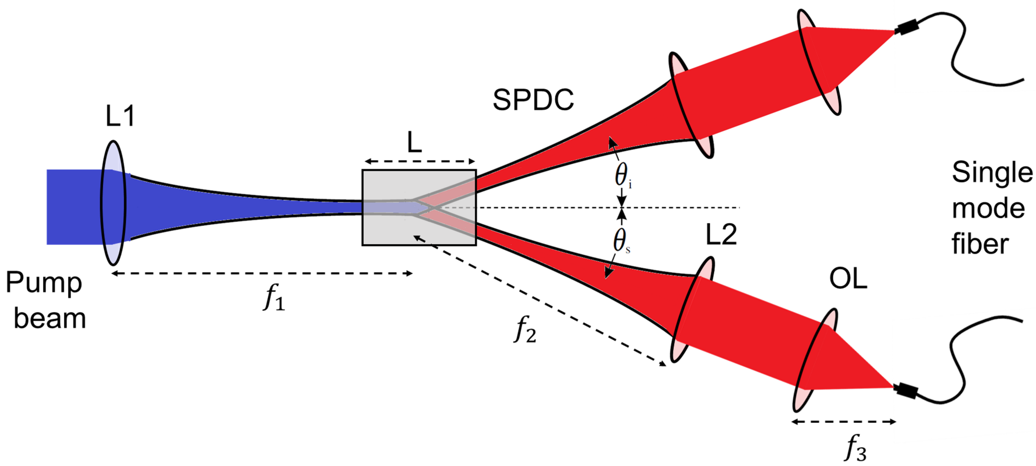

Figure 3.1: Pictorial representation of the generation and collection mechanism of pair photons in a non-linear crystal of length, L.

objective lens, OL, (f_3) is quite smaller ($\sim$ 5 mm) in comparison to the other lens, L2, ($\sim$25.4 mm and focal length, f_2) due to its small focal length. Therefore, it is essential to ensure the SPDC beam size is well within the clear aperture of the objective lens.

Since the fiber is placed at the back focal plane of the objective lens, the incident SPDC should have a collimated spatial distribution. Such collimation is controlled through the proper choice of the focal length of the pump focusing lens, L1 (focal length, f_1), and the collimating lens, L2 (focal length, f_2), i.e., by controlling the pump beam waist, ω_p and the collection beam waist, ω_s.

The pair photon coupling efficiency (η_c) is a measure of the fraction of coincidence counts for a given number of singles count. It is calculated using the following expression,

$$\eta_c = N_c/\sqrt{N_s N_i} \tag{3.1}$$

where, N_c is the coincidence count rate, while N_s and N_i are single photon count rates for signal and idler photons, respectively.

3.3 Experimental setup

The schematic diagram of the experimental setup used for optimum paired photon coupling is shown in Fig. 3.2. A 405 nm continuous wave (CW) laser having a maximum output power of 100 mW and linewidth < 8 MHz is used as a pump laser. To ensure the spatial mode of the laser output is in TE_{00}, a spatial filtering unit comprised of two fiber couplers, C1, C2, and an SMF, is employed. A half-wave plate ($\lambda/2$ plate) and a polarising beam splitter cube (PBS) are collectively used to control the pump power supplied to the non-linear crystal. The second half-wave plate $\lambda/2$ is used to adjust the polarization of the pump beam in accordance with the poling direction of the non-linear crystal to achieve optimal phase-matching. The plano-convex lens, L1, of focal length $f_1 = 50$ mm, is used to focus the pump beam at the center of the crystal to a beam waist radius (full width at half maximum) of ~ 25 µm. C is a periodically-poled potassium titanyl phosphate (PPKTP) crystal of 30 mm interaction length and having a single grating period of 3.425 µm. To ensure the optimal criteria of quasi-phase matching, the PPKTP crystal is housed in an oven with the temperature stability of $\pm$ 0.1°C. The pump photons, upon interaction with the PPKTP crystal, get downconverted into two daughter photons having a transverse profile in the form of an annular ring owing to the

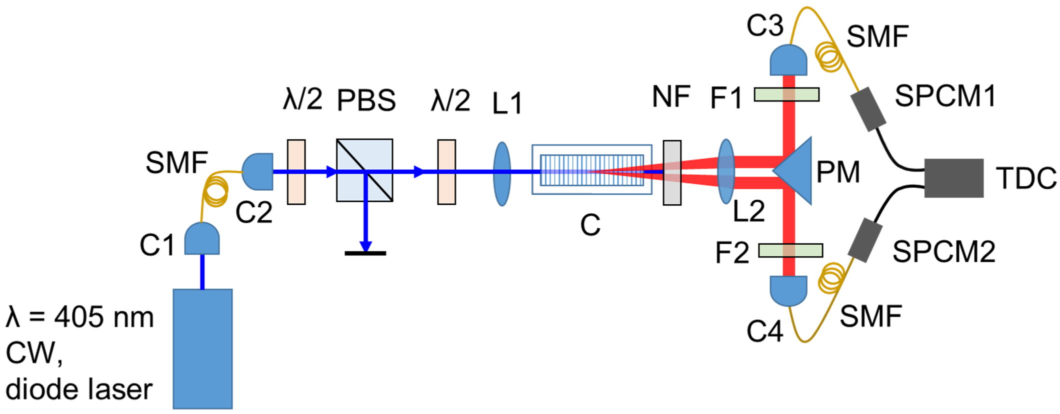

Figure 3.2: Schematic of the experimental setup. C1-4: fiber couplers, SMF: single-mode fiber, $\lambda/2$: half-wave plate; PBS: polarizing beam splitter cube; L1-2: plano-convex lenses, PPKTP: periodically poled KTP crystal; NF: Notch filter; PM: prism mirror, f_1-2: interference filter; SPCM1-2: single-photon counting modules; TDC: time to digital converter.

type-0 (e $\rightarrow$ e + e), degenerate, non-collinear phase-matching configuration. Any two diametrically opposite points of the annual ring possess the correlated pair of signal and idler photons. After removing the residual pump beam from the down-converted photons using a notch filer (NF), the SPDC ring is further collimated using another plano-convex lens L2 of focal length f = 50 mm. The signal and idler photons from the two diametrically opposite points of the SPDC ring are separated using a prism-shaped mirror PM and subsequently collected by fiber couplers C3 and C4. Each of the fiber couplers has an objective lens (OL, Thorlabs PAF2-7B) of focal length of f_3 = 7.5 mm, clear aperture of $\sim$ 4.5 mm, and numerical aperture of 0.3, enabling coupling of pair photons into the SMF of mode field diameter of $\sim$ 5 µm at 850 nm and a numerical aperture of 0.13. The interference filters (F1,2) act as narrow bandpass filters centered at 810 nm to remove residual photons. The SMFs are connected to the single photon counting modules SPCM (AQRH-14-FC, Excelitas). The output of the SPCMs are connected to a time-to-digital converter (TDC, idquantique-id800) for photon counting.

3.4 Results and Discussions

In order to investigate the effect of the pump beam waist (ω_p) and collection beam waist (ω_s) on the effective collection of pair photons, a systematic study has been carried out. The experimental observation for coincidence counts coupling to SMF is recorded using an interference filter of 810 $\pm$ 3.2 nm and at a coincidence window of 1.6 nanoseconds for various combinations of the pump (ω_p) and collection beam waist (ω_c) measured and estimated at the crystal center. The pump beam waist at the crystal center ω_p was varied from 25, 30, 42, 53, 71, and 84 µm by employing the lens L1 of different focal lengths, f_1 = 50, 100, 150, 200, 300, and 400 mm, respectively.

3.4.1 Coincidence counts coupling

Keeping the fixed collection lens, L2 of focal length f_2 = 50 mm, corresponding to the collection beam waist radius of ω_c = 29 µm is achieved at the crystal center, we varied the pump beam waist radius, ω_p, from 25 µm to 84 µm with the appropriate choice of the focal length of L1. The crystal temperature is kept fixed at 26°C. The coincidence counts as a function of the pump beam waist is shown in Fig. 3.3. As evident from Fig. 3.3, for a fixed collection beam waist radius, ω_c = 29 µm, the optimized coincidence count (black dots) decreases from the maximum value of 481.8 $\pm$ 3.6 kHz/mW to 105 $\pm$ 2.4 kHz/mW with the increase of ω_p from 25 µm to 84 µm. Such decrease in coincidence counts with the increase of pump beam waist radius, ω_p, can be attributed to the decrease of the parametric gain due to the decrease of pump intensity with the increase of pump waist radius ω_p for a fixed pump power and crystal parameters. On the other hand, the increase of the pump beam waist radius for a fixed de-magnification factor of the collection system (f_3/f_2 = 7.5/50 = 0.15) results in the beam waist radius of the collected photons exceeding the MFD of the SMF. As a result, the number of photons falling within the MFD of the SMF decreases with the increase of pump beam waist radius and overall coupling efficiency.

Next, to understand the effect of collection beam waist radius (ω_c) on paired photon

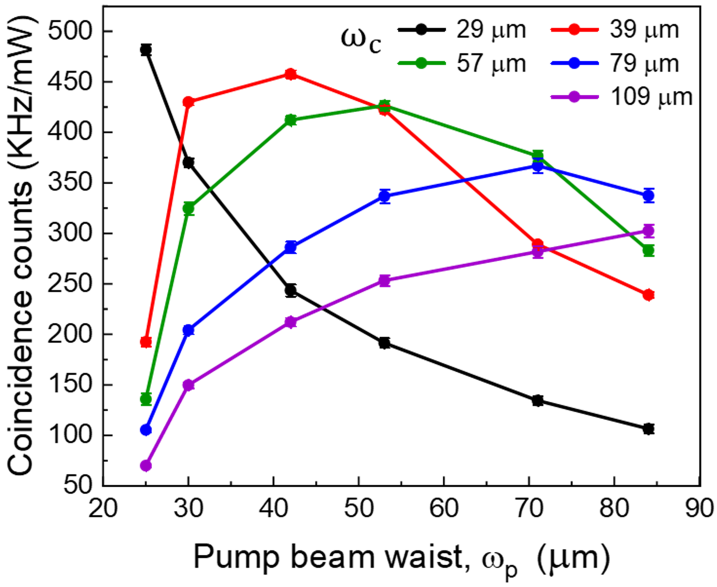

Figure 3.3: Variation of coincidence counts as a function of pump beam waist radius for different collection beam waist radius.

coupling, we have increased ω_c to 39 µm (f_2 = 100 mm) and repeated the measurement of coincidence counts with varying pump beam waist radius. As evident from Fig. 3.3, the coincidence counts (red dots) vary from 192.6 ± 4.5 kHz/mW for ω_p = 25 µm, to 239.2 ± 2.9 kHz/mW corresponding to ω_p = 84 µm clearly showing a maximum coincidence counts of more than 450 ± 4.5 kHz/mW for ω_p = 42 µm. Such variation can be understood as follows. The tighter focusing increases the divergence of the pump beam at the center of the nonlinear crystal (focal plane of the lens) and, thus, the divergence of the paired photons owing to the momentum conservation between the pump and down-converted pairs. As a result, the tighter focusing reduces the effective interaction length of the nonlinear crystal generating paired photons and increases of divergence of the pair photons missing the NA of the collecting fiber. On the other hand, the increase of the pump beam waist radius for a fixed pump power and crystal length decreases the generation rate of the paired photons. Therefore, there is a certain range of pump beam waist radius for the fixed collection beam waist radius, pump power, and crystal parameters providing the optimum coincidence counts. As expected, we observed a similar trend in coincidence counts for higher values of ω_c

as shown by green, blue, and purple dots. However, it is interesting to note that the increasing waist radius, ω_c, of the collection beam results in maximum coincidence counts at higher pump beam waist radius, ω_p. From Fig. 3.3, it is evident that the optimum coupling is observed for the ratio of ω_p, and ω_c close to unity, however, the maximum coincidence counts (see the peak of each curve of Fig. 3.3) decreases with the increase of pump beam waist.

These optimized values of the coincidence counts, as presented in Fig. 3.3, are achieved amid the various types of losses involved in the experimental setup. To keep things in perspective, the interference filter used for extraction of paired photons from the background photons has a transmission of ~ 90 %. On the other hand, the single-photon detectors have a maximum quantum efficiency of ~ 55 % at 810 nm. Additionally, the non-deal anti-reflection coating at the surface of optical components (dielectric mirrors and lenses) also contributes to the overall losses to the system. Apart from these losses, the coupling of paired photons into SMF encounters losses due to the mismatch in the numerical aperture of the objective lens of fiber couplers. Therefore, properly selecting all the components to minimize the overall loss can provide coincidence counts higher than the presented values.

3.4.2 Pair coupling efficiency

The pair coupling efficiency is a metric indicating the percentage of coincidence counts registered by the counter relative to single counts. It is also known as heralding efficiency [139]. The Fig. 3.4 shows the experimental observations of pair coupling efficiency of pair photons coupling into SMFs for various combinations of pump and collection beam waist, ω_p and ω_c, respectively. As evident from Fig. 3.4, the pair coupling efficiency for $\omega_c = 29$ μm (shown by black dots) remains almost unchanged (~ 22 %) for the entire available range of ω_p from 25 μm to 84 μm. Contrary to the decrease of coincidence counts with pump beam waist radius (as shown by black dots of Fig. 3.3), the constant pair coupling efficiency implies the decrease of single photon coupling due to the lower generation rate of paired photons as explained in sec. 3.4.1.

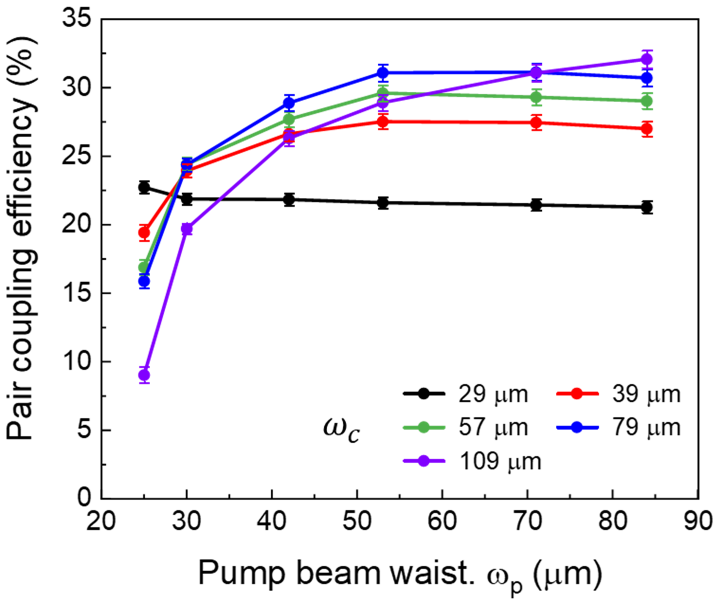

Figure 3.4: variation of the pair coupling efficiency to single-mode fiber for various combinations of pump and collection beam waist at the center of the crystal

However, for higher values of ω_c = 39 (red dots), 57 (green dots), 79 (blue dots), and 109 µm (purple dots), we observe the increase of pair coupling efficiency up to their respective pump waist radius providing maximum coincidence counts. Further increase of pump beam waist radius does not increase the pair coupling efficiency. It is also interesting to note that even though the overall maximum coincidence counts decrease with the increase of the waist radius of the coupled photons, as shown in Fig. 3.3, we observe an overall increase in the maximum pair coupling efficiency (η_c) from $\sim$ 9 % to $\sim$32 % for the increase of coupled photon beam waist radius, ω_c, from 29 µm to 109 µm. Such observation confirms that one can get a higher pair collection efficiency with loose focusing of the pump beam, however, at the cost of a lower paired photon number. Therefore, one has to find a trade-off between the required number of paired photons and the overall pair coupling efficiency depending upon the applications, as both these parameters can not be made high simultaneously.

3.4.3 Effect of crystal temperature on photon coupling

Knowing the effect of the pump beam waist radius and the coupled beam waist radius on the overall coincidence counts and pair coupling efficiency, we have studied the effect of phase-matching temperature of the crystal producing paired photons on pair coupling efficiency, and coincidence counts. It is known that the radius of the annular ring of the paired photon distribution generated through type-0, degenerate, non-collinear phase-matching of PPKTP crystal depends on the crystal temperature [140] as explained in chapter 2. The inset images of Fig. 3.5 show the transverse intensity profile of the SPDC ring recorded using an EMCCD camera with the change in crystal temperature. Using the transverse intensity profile of the SPDC ring, we measured the change of the SPDC ring radius from 6.75 $\pm$ 0.03 mm to 1.03 $\pm$ 0.03 mm for the crystal temperature variation from 20°C to 29.5°C. Again, for a fixed pump power and crystal parameters, the generation rate of the degenerate paired photons is constant irrespective of the crystal temperature for non-collinear phase-matching. As in the case of the PPPKTP crystal, the decrease of crystal temperature below the degenerate collinear phase matching temperature increases the radius of the annular ring, we expect the decrease of paired photon density over the fixed collection area [140]. Keeping the pump and collection beam waists, ω_p = 42 μm (f_1 = 150 mm) and ω_c = 57 μm μm (f_2 = 150 mm) fixed, we measured the coincidence counts and pair coupling efficiency with the results shown in Fig. 3.5. At every step of change in crystal temperature, we have optimized values of the coincidence count and pair coupling efficiency.

As evident from Fig. 3.5, the coincidence counts (black dots) increase quadratically from 160.9 $\pm$ 3.3 kHz/mW to 1692.3 $\pm$ 4.1 kHz/mW for the increase of crystal temperature from 20°C to 29.5°C, showing a 10 $\times$ enhancement in the overall coincidence counts rate. The red dot on the coincidence counts data corresponding to a crystal temperature of 26°C is the observation point for experimental observations discussed in the previous section. However, a further increase in the crystal temperature sharply reduces the overall coincidence counts as the spectrum of the generated photons goes beyond the transmission window of the interference filter ($\pm$ 3.2 nm centered at 810

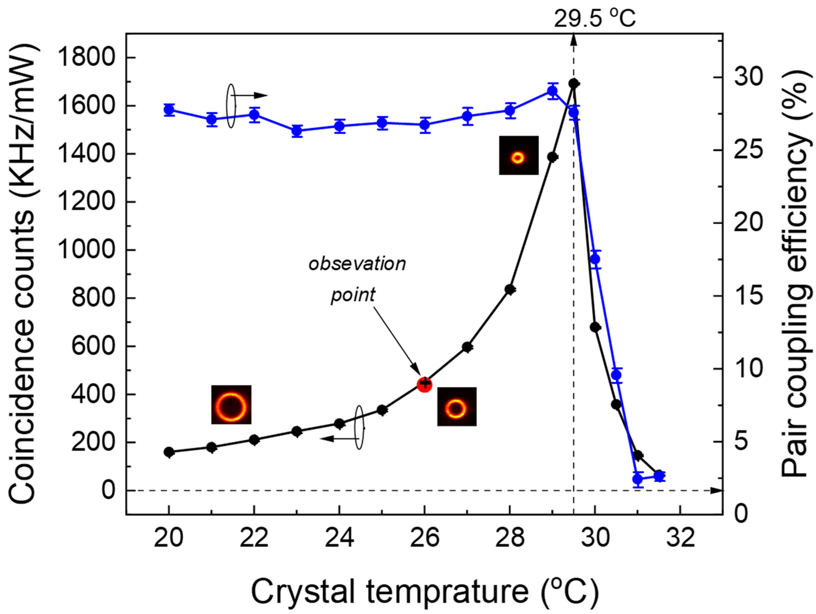

Figure 3.5: variation in the coincidence count (black dots, left axis) and pair photon coupling efficiency (blue dots, right axis) with the change in crystal temperature

nm). Therefore, we need to keep the crystal temperature below 29.5°C for any practical purpose. On the other hand, despite the substantial increase in the overall coincidence count with crystal temperature towards degenerate phase-matching temperature, the pair coupling efficiency (blue dots) remains almost unchanged at $\sim 28\%$. Such observation confirms that the pair coupling efficiency depends only on the focusing parameters of the pump and collection beams. Again, beyond the degenerated phase-matched temperature, the collection efficiency sharply decreases, similar to the variation of the coincidence counts (black dots). Such observation confirms the possibility of generation and subsequent collection of paired photons, enabling the development of bright paired photon sources for any practical application in quantum communication and quantum sensing.

3.5 Conclusions

In conclusion, we have successfully demonstrated the effect of the pump beam waist (ω_p) and the collection beam waist (ω_c) on the coincidence count collection and the pair coupling efficiency to single mode fibers to develop high brightness paired photon source. Using the optimized parameters for generation and detection, we achieved a maximum coincidence count of 1692.3 $\pm$ 8.5 kHz/mW for ω_p = 42 µm (f_1 = 150 mm) and ω_c = 57 µm µm (f_2 = 150 mm) at a crystal temperature of 29.5°C. We have observed a maximum coupling efficiency of 32.1 $\pm$ 0.6 % for the optimum combination of waist radius of pump, ω_p = 84 µm and collected photons, ω_c = 109 µm at a crystal temperature of 26°C. It is observed that both the pump intensity at the crystal center and the divergence of the SPDC photons play a crucial role in the overall brightness of the paired photons source. We have also observed that one can not access both the highest pair collection efficiency and the highest coincidence counts. Therefore, depending on the need and available resources, one can find the trade-off between the overall coincidence counts and the pair coupling efficiency. Such a study sets the foundation for the current thesis.

Chapter 4

Improving the performance of the spontaneous parametric down-conversion based source to the external perturbations

Spontaneous parametric down-conversion (SPDC) in nonlinear optical materials has evolved as the primary resource of photonic quantum entangled states but suffers from a strong dependence on the intrinsic phase matching condition. This makes it susceptible to changes in factors such as the pump wavelength, crystal temperature, and crystal axes orientation, with improved stability often at the expense of spectral brightness. This intolerant to changing environmental factors prohibits its deployment in non-ideal environments outside controlled laboratories. Here, we report on a novel system architecture based on a hybrid linear and non-linear solution that we show makes the source tolerance enhanced without sacrificing brightness. Our linear solution is a lens-axicon pair, judiciously placed, which we test together with two common non-linear crystals, quasi-phase-matched periodically-poled KTP, and birefringent-phase-matched BIBO. We show that despite variations of the SPDC output, the hybrid system's performance remains nearly constant across extreme environmental condition changes. Our approach has the benefit of simultaneous tolerance to the environment and high brightness, which we demonstrate by using the proposed architecture as a stable entangled photon source and report a spectral brightness as high as 22.58±0.15 kHz/mW with a state fidelity of 0.95±0.02, yet requiring a crystal temperature stability of only ±0.8°C, a 5× enhanced tolerance as compared to the conventional high brightness SPDC configurations. Our solution offers a new approach to deployable high brightness quantum sources that are robust to their environment, for instance, in satellite-based quantum applications.

4.1 Introduction

The most prominent manifestation of non-locality proposed by quantum mechanics, commonly known as quantum entanglement [141], has found its implications in various domains, including quantum information, quantum communication, quantum metrology, and quantum computation [10, 11, 14, 73, 142–145]. The central point of convergence of all these quantum technologies is to enhance information security by establishing a global-scale network of quantum internet [23, 142] interconnected through different nodes and channels at various locations of the earth while accessing the advantage of quantum communication. Quantum communication, such as quantum key distribution (QKD) [10, 143, 146], is considered superior to its classical counterpart due to the encryption of the information through the use of the resourcefulness of photonic entanglement. Core to QKD is the need for an entangled photon source (EPS)[127, 147–149] with high state fidelity, while long-distance QKD networks through optical fiber or free-space channels demand high brightness EPSs. One of the straightforward approaches to achieve this is to enhance the brightness of the EPS based on spontaneous parametric down-conversion (SPDC) in $\chi^{(2)}$ nonlinear optical crystals [11, 69, 71, 127, 147, 148]. Efforts in this regard include replacing critically phase-matched crystals [127, 147, 149] with quasi-phase-matched periodically poled crystals [11, 90], including Potassium Titanyl Phosphate (PPKTP) crystals in a type-II phase-matching geometry [150–152], as well as in a type-0 phase-matching geometry [137]. Among all the nonlinear crystals, PPKTP crystals in type-II phase-matching geometry have been used widely for entangled photon sources [152] despite exploring the full benefits of long interaction length and the high nonlinear coefficient as achieved in type-0 phase-matching geometry. This is due to the practical limitations in separating and detecting collinear, co-polarized paired photons of the same wavelength individually. Unfortunately in such crystals the refractive index is strongly dependent [81, 153, 154] on temperature, the wavelength of the interacting radiation, and the angle of the optic axis, so that the key SPDC features such as cone angle and the ring radius of the SPDC photons changes with any of these physical parameters. As a result, typical laboratory based SPDC experiments have careful selection of the laser, stringent stabilization of the pump wavelength to avoid mode hopping and mode jitter, and dynamic control of the crystal temperature (for quasi-phase matched crystals) or precise angle control (for birefringent phase matched crystals). Although these stringent requirements are easily addressable in laboratory conditions, deploying such sources outside the laboratory is hindered by the complexity of the solution, for example, satellite-based applications demands a stringent mass and power budget [155] so a wish-list of solutions is not viable. Therefore, it is essential to develop entangled photon sources with relaxed tolerance to such environmental factors.

Here, we report on a hybrid linear and non-linear solution for a stable and bright quantum source with relaxed tolerances in the stabilization of the crystal temperature, mode hopping, and jitter of the pump laser, as well as the angle of the nonlinear crystal. To verify the concept we have used both PPKTP crystal and BIBO (bismuth borate) crystals producing non-collinear, degenerated down-converted photons through quasi-phase-matching (QPM) and birefringent phase-matching (BPM), respectively, and transformed the annular SPDC ring into what we call a perfect ring using an axicon and Fourier transforming lens. We show that while the SPDC output varies tremendously with changing conditions, the hybrid system produces a stable output across a wide variation in external factors. The result is a bright entangled photon source that is tolerance-enhanced, making this approach suitable for deployable quantum sources in non-ideal environments.

4.2 Theory and Experiment

The intensity distribution of the downconverted photons for a nonlinear crystal of length, L, can be represented as

$$I_{\text{SPDC}} \sim \operatorname{sinc}^2(\Delta k L/2) \tag{4.1}$$

where the momentum mismatch Δk for the non-collinear, degenerate photons for type-0, first order quasi-phase matching, and type-I birefringent phase matching are given as

$$\Delta k = k_p - k_s\cos(\phi) - k_i\cos(\phi) - \frac{2\pi}{\Lambda} \tag{4.2}$$

and

$$\Delta k = k_p - k_s\cos(\phi) - k_i\cos(\phi) \tag{4.3}$$

Here, $k_{p,s,i} = \dfrac{2\pi n_{p,s,i}}{\lambda_{p,s,i}}$ is the wavevector and $n_{p,s,i}$ is the refractive index of the medium for the pump, λ_p, signal, λ_s, and idler, λ_i, wavelengths. Λ is the period of the periodically poled nonlinear crystal and ϕ is the angle the signal and idler wave vectors make with the pump wave vector along the propagation direction. For degenerate (λ_s = λ_s = 2λ_p), non-collinear, type-0 ($e\rightarrow e+e$) and type-I ($o\rightarrow e+e$) phase matching, the cone angle, ϕ, of the down-converted photons can be represented using Eq. (4.2) and Eq. (4.3) as

$$\phi_{\text{QPM}} = \arccos\left(\frac{n_p^e}{n_s^e} - \frac{\lambda_p}{n_s^e\Lambda}\right) \tag{4.4}$$

and

$$\phi_{\text{BPM}} = \arccos\left(\frac{n_p^o}{n_s^e(\theta)}\right) \tag{4.5}$$

where QPM and BPM refer to quasi-phase matching and birefringent phase matching, respectively. Here, θ is the angle of the optic axis with the propagation direction. We plot the effect of this in 4.1 with the help of the dispersion relations of PPKTP

[156] and BIBO [157] crystals, clearly showing how the environmental factors influence cone angle and thus the shape and size of the SPDC output. To circumvent this

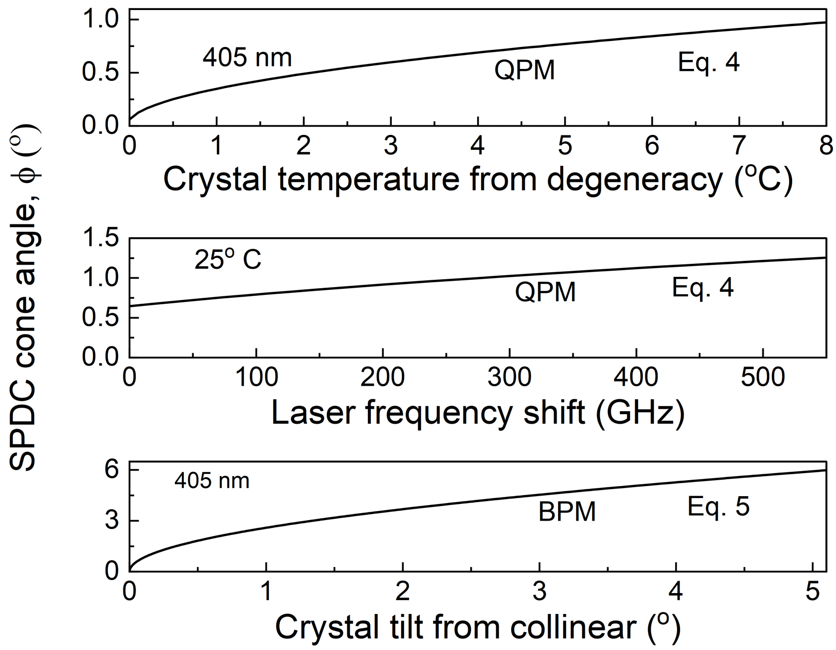

Figure 4.1: Variation of the SPDC cone angle, ϕ, with the crystal temperature (top panel) and laser frequency shift (middle panel) for the quasi phase matching condition (QPM) given in Eq. (4.4). In the bottom panel the results are shown for the birefringent phase matching (BPM) condition given by Eq. (4.4), here as a function of crystal tilt angle.

we adopt the approach illustrated in 4.2(a). The core idea is to treat the SPDC ring as similar to a hollow Gaussian beam (HGB): a dark core beam with annular intensity distribution and plane wavefront. What happens when such a beam is incident on an axicon? The answer is that it forms a displaced Bessel beam, the displacement determined by the annular ring radius [158]. Interestingly, the Bessel beam itself remains unchanged with ring size as its radial structure is determined by the cone angle of the axicon. On the other hand, it is well known that the Fourier transformation of a Bessel beam results in a perfect annular intensity distribution with a ring radius that depends on the radial wavevector of the Bessel beam [140, 159]. Therefore, for a fixed radial distribution of the Bessel beam, the position and size of the perfect ring is constant and independent of the change in the input beam to the axicon. To see how this can be exploited in SPDC experiments, consider the present experiment: a pump photon on propagation through the nonlinear crystal (PPKTP or BIBO) splits into pairs of degenerate daughter photons, obeying conservation of momentum and energy. The generated photons are distributed over an annular ring with an intensity distribution given by Eq. (4.1). After collimation by lens $L1$, the spatial distribution of the photons is transformed into a zero-order Bessel beam of fixed radial wavevector after propagation through the axicon. Given that the Fourier transformation can be possible by putting the object after the lens [160], the lens $L2$ of focal length, f, in combination with the axicon placed at a distance $f-D$ behind the lens Fourier transforms the zero-order Bessel beam into a perfect annular ring at the back focal plane of the lens, independent to the change in the spatial distribution of the generated photons. Here, D is the distance of the axicon from the back focal plane of the lens, $L2$. One can then write the intensity distribution of the perfect annular ring as

$$I_{Perfect} = \frac{w_g^2}{w_D^2} \exp\left(-\frac{2(\rho\frac{f}{D}-\rho_r)^2}{w_D^2}\right) \tag{4.6}$$

where w_g is the beam waist radius of the Gaussian beam confining the Bessel Gauss beam. The perfect annular ring of width, $2w_D = 1.65\ w_0$, (w_0 is the Gaussian beam waist at the focus), is formed at, $\rho = \frac{D}{f}\rho_r$ with a modified ring radius, $\rho_r = D\sin((n-1)\alpha)$, where n and α are the refractive index and the apex angle of the axicon.

As a result, a perfect annular ring of constant width is formed irrespective of the ring size of the SPDC photons generated by the crystals, making the downconverted photons insensitive to the fluctuations of the phase-matching parameters to external environments. To validate our approach, we have devised the experiment shown schematically in 4.2(b). A continuous-wave, single-frequency (linewidth ∼12 MHz) laser providing output power of 50 mW at a wavelength of 405 nm was used as a pump source. The mode filtering system comprised of two fiber collimators, C1 and C2, and a single mode fiber, SMF, was used to transform the laser output in a Gaussian beam. A combination of the $\lambda/2$ plate and the polarizing beam splitter (PBS) cube was used to control the pump power in the experiment. A second $\lambda/2$ plate was used to transform the horizontal polarization state of the pump into a diagonal to maintain equal pump

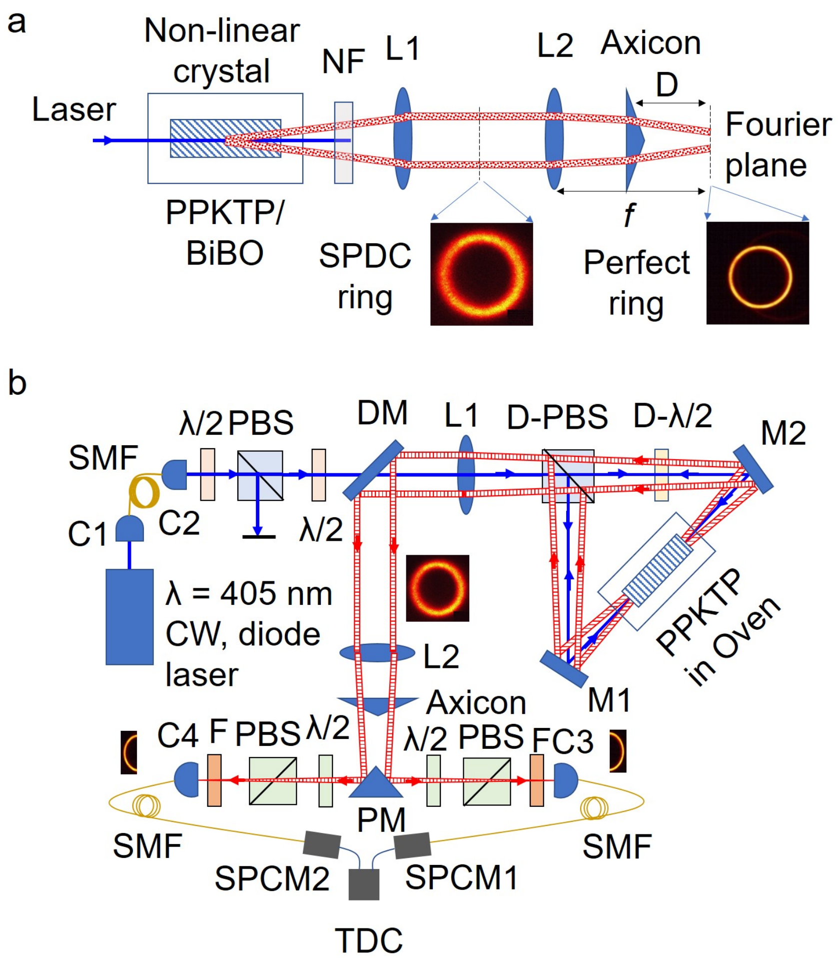

Figure 4.2: (a) Pictorial representation of the basic principle of downconverted photons with "perfect" annular intensity distribution. (b) Schematic of the experimental setup. $\lambda/2$: half-wave plates; PBS: polarizing beam splitter cube; DM: dichroic mirror; L1-2: lenses; M1-2: mirrors; PPKTP: periodically poled KTP crystal; F: interference filter; PM: prism mirror, C1-4: fiber couplers, SMF: single-mode fiber, SPCM1-2: single-photon counting modules; TDC: time to digital converter. (Inset) ICCD image of the spatial profile of single photons.

power of the clock-wise and counter-clockwise beams of the polarization in the Sagnac interferometer, the latter was comprised of a dual-wavelength PBS (D-PBS) and two plane mirrors, M1 and M2. A 20-mm long and 2 x 1 mm^2 PPKTP crystal placed at the center of the Sagnac interferometer between mirrors, M1 and M2, and was pumped from both sides using the plano-convex lens (L1) of focal length, f = 150 mm. The PPKTP crystal had a single grating period, Λ = 3.425 μm, and was housed in an oven with temperature stability of $\pm$0.1°C to produce degenerate down-converted photons at a wavelength of 810 nm owing to type-0 ($e \rightarrow e+e$), non-collinear, phase matching of the pump photons. The dual-wavelength $\lambda/2$ plate (D-$\lambda/2$), at both 405 nm and 810 nm, transformed the polarization of both pump and the down-converted photons from horizontal to vertical and vice versa. The counter-propagating SPDC photons of the polarization Sagnac interferometer on recombination by the D-PBS resulted in a Bell state [11]. After collimation by the lens, L1, and subsequent extraction by the dichroic mirror, DM, the down-converted photons in the annular intensity profile (see inset image) were transformed into an annular ring of fixed diameter using a combination of lens and axicon. The Fourier transform of the Bessel beam generated by the axicon placed after the lens [140, 160] was transformed into an annular ring at the back focal plane of the lens L2, of focal length, f =100 mm. The apex angle of the axicon was 178.4°C. The annular intensity profile of the down-converted photons was divided into two symmetric half rings (see the inset images) using the prism mirror, PM (gold-coated right-angle prism). The pair photons were collected by the fiber couplers, C3 and C4, placed at the focal plane of the lens, L2. The polarization states of the photons were studied using the combination of $\lambda/2$ plate and PBS. The interference filter, F, of spectral width 3.2 nm centered at 810 nm, was used to extract down-converted photons from the background. The single-photon counting modules, SPCM1-2, connected to the fiber couplers, C3 and C4, using single mode fiber (SMF) or multimode fibers, and the time-to-digital converter (TDC) were used to measure the single counts and coincidence counts. The temporal coincidence window for all the measurements was 1.6 ns.

The size of the annular intensity profile and corresponding photon density depends on the position of the axicon from the Fourier plane. However, placing the axicon close to the Fourier plane to increase the overall photon counts adds mechanical constraints to the detection and analyzer systems. In such a case, a 4-f imaging system (not shown here) is used to collect and analyze the down-converted photons. Note that this approach also works with type-0 phase-matching by sandwiching two type-0 crystals with orthogonal poling period direction in a dual-crystal scheme.

4.3 Results

To verify the concept of the SPDC perfect ring, we have measured the spatial distribution of the down-converted photons before the lens, L2, and at it's Fourier plane while varying the pump wavelength, crystal angle, and crystal temperature. The results are shown in 4.3. For this study, we have used the polarization state of the input laser to be either horizontal for BiBO crystal or vertical for PPKTP crystal. As evident from the first column, (a-c), of 4.3, the spatial distribution of the SDPC photons generated by the PPKTP crystal at a temperature of 25°C changes from the collinear Gaussian distribution to the non-collinear annular ring for pump wavelengths 408.96 nm, 405.01 nm, and 405.13 nm. However, the diameter of the "perfect" ring as shown in the second column, (d-f), of 4.3, recorded at the Fourier plane, is the same for all pump wavelengths and independent of the spatial distribution of the SPDC photons. Similarly pumping the BIBO crystal having cut angle, θ = 151.7° (ϕ = 90°) in optical yz-plane for perfect phase-matching of non-collinear type-I ($o \rightarrow e + e$) degenerate down-converted photons at 810 nm, with the laser wavelength λ_p = 405.01 nm, we have varied the crystal angle and recorded the intensity distribution of the SPDC ring and the "perfect" ring as shown in the third column, (g-i), and forth column, (j-l), of 4.3, respectively. As expected, the spatial distribution of the SPDC photons changes from the collinear geometry to non-collinear geometry with increasing diameter of the annular ring for the crystal tilt angle 1°, 3° and 5°, whereas the diameter of the "perfect" ring is constant for all crystal angles. On the other hand, to verify the "perfect" ring for the variation of crystal temperature, we pumped the PPKTP crystal with the laser wavelength of λ_p= 405.01 nm, and recorded the intensity profile of the SPDC ring and the "perfect" ring for crystal temperature 28°C, 27°C, and 25°C. As evident from the fifth column, (m-o), of 4.3, the spatial distribution of the SPDC photons changes from the collinear geometry at 28°C to the non-collinear annular ring of increasing diameter with the crystal temperature 27°C and 25°C. However, the diameter of the "perfect" ring as shown in the sixth column, (p-r), of 4.3 irrespective of the change in the spatial profile of the SPDC photons due to the change in the phase-matching condition. The current results reveal that the position and size of the "perfect" ring of the down-converted photons are insensitive to the physical parameters influencing the phase-matching condition. As a result, the photon collection optics set to couple the pair photons on the diametrically opposite side of the annular ring does not see any effect of the change in the physical parameters responsible for the phase-matching of the nonlinear crystal. Therefore, the present technique enables the use of relaxed phase-matching parameters for the practical implementation of the down-converted photon-based quantum sources.

To gain further insight, we have recorded the spatial profile of the SPDC ring and the

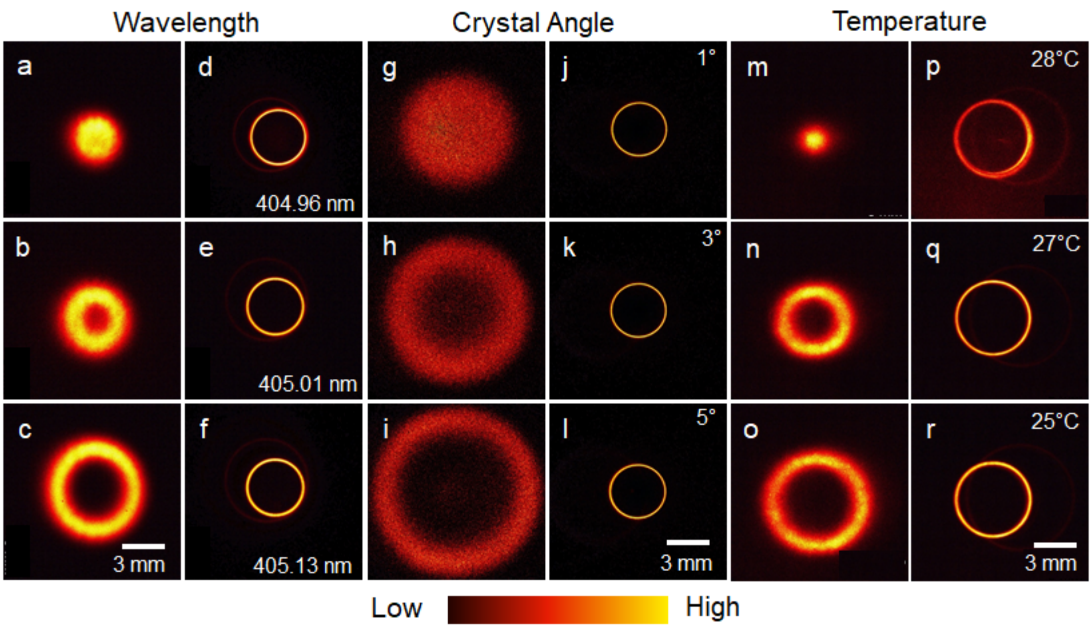

Figure 4.3: Variation of the spatial distribution of the (a-c) SPDC ring and (d-f) perfect ring as a function of pump wavelength for a fixed temperature of 25°C of PPKTP crystal. Dependence of the spatial distribution of the (g-i) SPDC ring and (j-l) perfect ring as a function of phase matching angle of BIBO crystal for a fixed pump wavelength of 405.01 nm. Variation of the spatial distribution of the (m-o) SPDC ring and (p-r) perfect ring as a function of PPKTP crystal temperature for a fixed pump wavelength of 405.01 nm.

perfect ring with the increase of crystal temperature from 21°C with a step of 0.5°C for the PPKTP crystal and the tilt of BIBO crystal and measured the diameter and the width of the rings with results shown in 4.4. As evident from 4.4(a), the radius of the SPDC ring (black squares) increases with the PPKTP crystal temperature, $\Delta T = T_o - T$, away from the degenerate collinear phase-matching temperature, $T_o = 28^\circ$C. However, the radius of the perfect SPDC ring (red circles) remains constant at $\sim$2.73 mm. The variation in the cone angle or the diameter of the annular ring of the SPDC photons with temperature is the same as that of the previous report [11] and closely matches the theoretical fit (black line) based on Eq. (4.4) and the dispersion relation of Ref. [156]. However, the shift in the temperature of the degenerate collinear SPDC photons from 36°C as shown in the report [11] to 28°C can be attributed to the change in the laser wavelength. On the other hand, the width (FWHM) of the SPDC ring (open squares), as shown in 4.4(a), remains constant for all phase matching temperatures, but the width of the perfect SPDC ring (open circles) is constant ($\sim$200 μm) with temperature (up to 3°C) and increases to 380 μm at 7°C. In literature, it is observed that the width of the perfect vortex increases with the order of the input vortex [161]. Therefore, to get a better perspective on the variation of the width of the SPDC perfect ring, we have calculated the vortex ring radius with the order using Eq. (3) of Ref. [162] and fit (blue line) to the experimental results (black square) in 4.4(a). As evident from 4.4(a), the rate of increase of the SPDC ring radius with temperature is faster than that of the vortex ring radius with its order. The change in the SPDC ring radius for the crystal temperature 7°C away from the collinear phase-matching temperature (28°C) is equivalent to the change in the ring radius of the vortex beam for an order increase of 50. Therefore, using the similar analogy of Ref. [161], we can confirm that the increase in the width of the SPDC perfect ring (open circles of 4.4(a)) is due to the increase in the SPDC ring radius with crystal temperature. One can use the similar treatment of Ref. [161] to reduce the width of the SPDC perfect ring by increasing the radius of the perfect ring by simply moving the axicon close to the lens L2. However, such a proposition will reduce the photon number density collected by the fibers and the overall brightness of the paired photon source. Similarly, as evident from 4.4(b), the radius of the SPDC ring (black dots) increases with the tilt angle of BIBO crystal, $\Delta\theta = \theta_o - \theta$, away from the degenerate collinear phase-matching angle, $\theta_o = 152^\circ$. However, the radius of the perfect SPDC ring (red dots) remains constant at $\sim$2 mm. The variation in

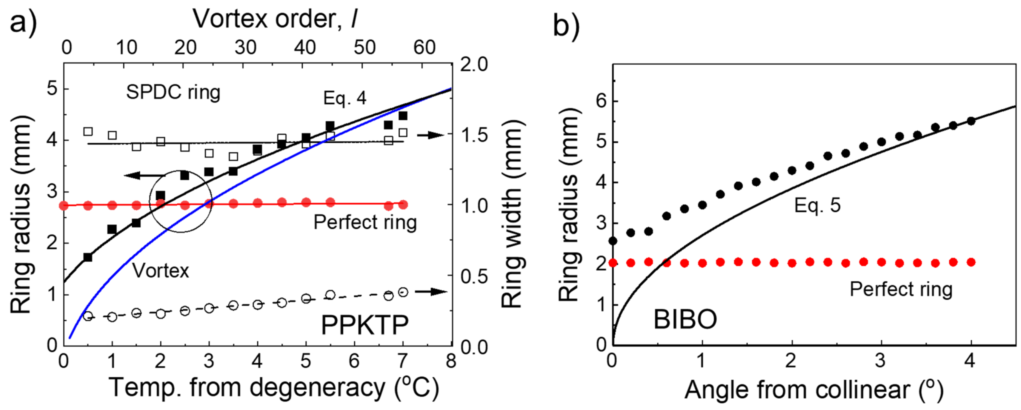

Figure 4.4: (a) Variation of the radius of the SPDC ring (black dots), and the SPDC perfect ring (red dots) with the PPKTP crystal temperature away from degeneracy at T_o=28°C. The black line is the theoretical fit of Eq. (4.4) to the experimental results and the blue line represents the variation of vortex beam radius with its order. Variation of the width of the SPDC ring (open square) and perfect ring (open circle) with the crystal temperature. Lines are guide to eyes. (b) Variation of the radius of the SPDC ring (black dots) and the SPDC perfect ring (red dots) with the tilt in the phase-matching angle of the BIBO crystal away from degenerate collinear phase-matching angle, $\theta_o = 152°$. The black line is the theoretical fit of Eq. (4.5) to the experimental results.

the cone angle or the diameter of the annular ring of the SPDC photons with tilt closely matches the theoretical fit (black line) based on Eq. (4.5) and the dispersion relation of Ref. [157]. On the other hand, due to the unavailability of suitable laser diodes with controlled wavelength variation in the lab, we could not test the current scheme for more wavelengths. However, it is evident from the first and second columns of 4.3 that the radius of the SPDC perfect ring is constant despite the variation of the SPDC ring radius due to the change in the pump wavelength by ±150 GHz making the quantum source insensitive to the mode hop and wavelength jitter of the pump laser.

Proving the generation of the "perfect" SPDC ring insensitive to the external physical parameters influencing the phase-matching process of the nonlinear medium, we have studied the coincidence counts of the photons collected from diametrically two opposite points on the SPDC ring and the perfect ring. The results are shown in 4.5. Keeping the laser wavelength and the crystal temperature constant at 405.01 nm and 25°C, respectively, we have measured the coincidence counts while varying the crystal temperature with the results shown in the first panel of 4.5(a). As evident from 4.5(a), the coincidence counts (red dots) between the pair photons collected using the single-mode fiber from the SPDC ring optimized for a crystal temperature (say, 25°C) decreases for the crystal temperature away from 25°C with a temperature bandwidth (FWHM) of 1°C. However, the coincidence counts for the photons collected using single-mode (black dots) and multimode (blue dots) from the SPDC perfect ring have a temperature bandwidth of 3.2°C and 6.5°C, resulting in a 3.2 and 6.5 times enhancement in the temperature bandwidth. Further analysis reveals that a 10% peak-to-peak fluctuation in the coincidence counts requires the crystal temperature stabilization within ±0.15°C for the SPDC ring. However, the use of the "perfect" SPDC ring relaxes the temperature stability requirement of ±0.8°C, and ±1.25°C for photon collection using single-mode and multimode fibers, respectively. Similarly, pumping the BIBO crystal with a laser wavelength of 405.01 nm, we have measured the coincidence counts for the SPDC ring and the perfect ring while varying the tilt of the BIBO crystal away from degenerate collinear phase-matching angle, θ_o = 152° with the results shown in the second panel of 4.5(a). As evident from 4.5(a), the coincidence counts (black dots) between the pair photons collected using the single-mode fiber from the SPDC ring optimized for a cone angle of 3° vary with the crystal tilt resulting in an angular bandwidth (FWHM) of ∼2.5°. However, under the same experimental condition, the angular bandwidth (FWHM) for the "perfect" ring is ∼6°, more than two times broader than the SPDC ring. Further analysis reveals that a 10% peak-to-peak fluctuation in the coincidence counts requires the crystal angle stabilization within ±22 mrad for the "perfect" ring, almost three times relaxation as compared to the SPDC ring (angle stabilization within ±8 mrad. Using the PPKTP crystal, we have also measured the stability of the coincidence counts of the "perfect" ring, SPDC ring over 15 min with the wavelength jittering of the laser diode with the results shown in 4.5(b). In doing so, we switched off the temperature stabilization of the laser diode and measured the wavelength using the high-resolution wavemeter (HighFinnese). As evident from 4.5(b), the laser diode has a frequency shift of 6 GHz in 15 min. The simultaneous measurement of the coincidence counts reveals that the quantum source based on the "perfect" ring has a counts fluctuation (standard deviation) of 4.8%, 2.5 times better stable than that of the SPDC ring (standard deviation ∼12.6%) for the pump frequency shift of 6 GHz over 15 min. Due to the unavailability of a suitable laser diode with the controlled variation of frequency, we could not characterize the current technique for higher frequency shift. However, using the dispersion relations [156] of PPKTP crystal and the temperature acceptance bandwidth we can estimate the stable performance of the "perfect" ring-based quantum source for the laser frequency shift of ∼100 GHz.

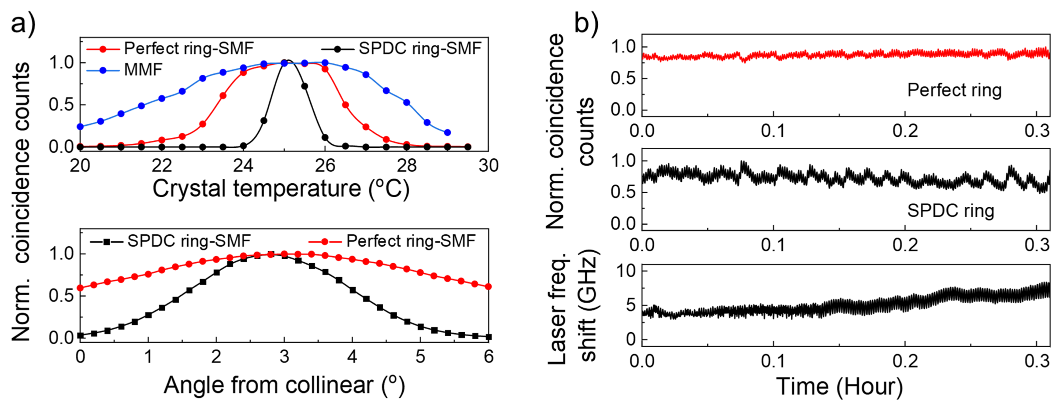

Figure 4.5: (a) Variation of coincidence counts of the paired photons collected from the diametrically opposite points of the SPDC ring and "perfect" ring with PPKTP crystal temperature and the tilt angle of the BIBO crystal. (b) Stability of the coincidence counts of the quantum source based on the "perfect" ring and SPDC ring with the variation of laser frequency over 15 min.

Confirming the performance of the SPDC source of new architecture requiring relaxed constrain in the physical parameters influencing the phase-matching condition, we have designed the polarization-entangled photon source and characterized it using the standard coincidence measurement technique. Keeping the polarization of the pump laser diagonal, we have rotated the polarization state of one of the pair photons using the analyzer and measured the coincidence with its partner photon collected from the diametrically opposite point of the SPDC perfect ring at a fixed polarization state, H (horizontal), D (diagonal), V (vertical), and A (anti-diagonal). The results are shown in 4.6(a). As evident from 4.6(a), we observe a typical quantum interference of the polarized entangled photons for H (black dots), V (blue dots), D (red dots), and A (green dots) projections at the crystal temperature of 25°C. The solid lines are the best fit for the experimental data. The number of detected entangled paired photons have maximum and minimum values of $\sim$2.2 x 10^4 Hz/mW and 7 x 10^2 Hz/mW for all polarization projections. The raw fringe visibility for polarization correlation is 94.2±0.06% in H/V bases and 93.8±0.06% in D/A bases confirming the non-local behavior of quantum entanglement. We also have calculated the Bell's parameter to be S = 2.64±0.03, corresponding to a violation of 21 standard deviations, confirming the generation of high-quality entangled photons. Further, we have measured the quantum

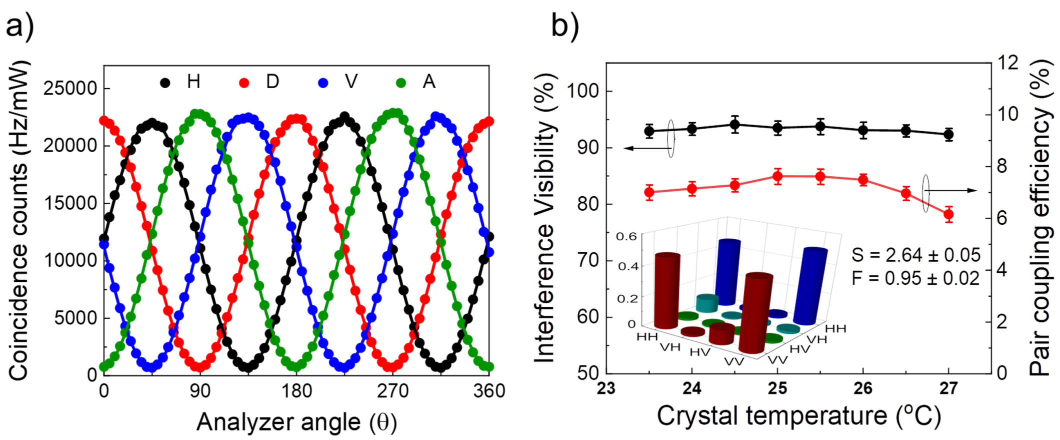

Figure 4.6: (a) Quantum interference of the entangled photons projected at different polarization states, H, D, V, and A. (b) Variation of quantum interference visibility (black dots) and coupling efficiency (red dots) with crystal temperature. (Inset) Graphical representation of the absolute values of the density matrix of the entangled photon states. Lines are the guide to the eyes.

interference visibility and the coupling efficiency (ratio of the coincidence counts to the square root of the product of the singles counts of two detectors) of the source at different crystal temperatures with the results shown in 4.6(b). As evident from 4.6(b), the interference visibility and the coupling efficiency are constant at $\sim$93% and 7%, respectively, for almost the entire temperature range; however, the coupling efficiency decreases with crystal temperature toward the collinear phase-matching.

Since we are using the highest figure-of-merit of the nonlinear process to generate entangled photons, the growing demands of multiple entangled pairs desirable for advanced quantum optics and information experiments can only be addressed by increasing the coupling/collection efficiency. It is evident from the literature [163–165] that the coupling efficiency depends on the size of fibers effectively imaged onto the crystal plane and the crystal length, scaled to the pump beam waist into the crystal. Therefore, by optimizing these parameters, one can increase the overall entangled photon pair rate of the EPS. Such a study in itself is an interesting topic but beyond the scope of the current work as we have mostly focused on the tolerance of the EPS performance to external perturbations. Again, it is worth noting that the current system architecture results in entangled pair counts of $>$ 0.3 MHz/mW without considering the losses in the experiment and the efficiency of the detectors. Since the quality of the generated quantum state does not depend on the collection efficiency, we have measured the degree of entanglement of the photon states using the linear tomographic technique [166]. The results are shown in the inset of 4.6(b). From the graphical representation of the absolute values of the density matrix of the generated states (see inset of 4.6(b)), we determine the state to be, $|\psi >= \frac{1}{\sqrt{2}}(|HH > -|VV >)$, with a state fidelity of 0.95. As explained previously [11], we can transform the generated state to another Bell's state by adjusting the position of the crystal [167] in the Sagnac interferometer.

4.4 Discussion

The approach we have outlined has the benefit of improving the tolerance of EPSs without sacrificing brightness performance, the only approach to allow both to be optimized simultaneously. To see this, consider the comparative analysis of our approach versus other standard approaches based on bulk nonlinear crystals given in Table 1. We see that EPSs based on BPM nonlinear crystals such as bismuth borate (BBO) and BIBO can produce entangled states with high fidelity ($>$ 0.95) but have exceptionally lower spectral brightness ($\sim$ 2 kHz/mW) due to their intrinsic lower nonlinear coefficient ($d_{\mathrm{eff}} \sim 2.2 - 3.4$ pm/V) and small effective interaction length avoiding spatial walk-off effect [134, 135], severely restricting their usefulness for practical applications. Again, the strong dependence of the refractive index on the orientation of the optics axis of such crystal and the wavelength of the interacting radiations demands

	Phase-matching	Nonlinear crystals	Entanglement properties		Tolerance to external parameters		
			Spectral brightness	Fidelity	Temperature	Crystal angle	Pump wavelength
Other studies	BPM	BBO/BIBO [40,41]	Low	High	-	Low	Low
	QPM	PPLN [21, 22, 42-44]	Moderate	High	High	-	Low
		PPKTP [9,19,46]	High	High	Low	-	Moderate
Current study	BPM	BIBO	Low	High	-	High	High
	QPM	PPKTP	High	High	High	-	High

Table 4.1: Qualitative comparison of entanglement properties and the tolerance parameters of entangled photon sources

a tight control in the crystal angle and pump wavelength for stable operation of the EPS. Naturally, efforts have been made to explore QPM-based nonlinear crystals with higher nonlinear coefficients, including periodically poled lithium niobate (PPLN) and PPKTP to improve the spectral brightness of the EPS. However, due to the practical limitation of fabricating a small poling period, the PPLN crystals are used for EPSs in the telecommunication wavelength range [137, 138, 152, 168, 169], where the single photon detectors are either bulky or inefficient. Exploiting the dispersion relations of PPLN crystal in type-II phase-matching, efforts have been made to improve the tolerance in the crystal temperature [152]; however, such efforts are very wavelength selective and not possible to achieve for EPSs of other wavelengths.

On the other hand, to access the benefits of the compact Si-based single photon detectors with a relatively higher quantum efficiency [20], bright EPSs are developed using PPKTP crystals. While type-II phase-matched PPKTP crystals offer advantages in terms of simpler experimental setup and the use of longer interaction lengths lead to high spectral brightness ($>$ 10 kHz/mW), and quantum state fidelity, however, such sources have low to moderate tolerance to the external perturbations including crystal temperature and pump wavelength variation. Additionally, the sources require pre or post phase compensation between the pair photons to maintain high quantum state fidelity [93, 150].

Recently, PPKTP [11] and PPLN [137] crystals in type-0, non-collinear phase-matching configuration have been explored to develop bright EPSs of degenerate photons in simple and compact experimental configuration without the need for any phase-compensation. While these sources have very high spectral brightness due to the use of the highest figure-of-merit of the nonlinear crystal and state fidelity [11, 137], they have low to moderate tolerance to the perturbation of external parameters, including crystal temperature and pump wavelength due to the change in the spatial distribution to the SPDC photons with respect to the fixed photon detection systems. Contrary to all the previous reports on EPSs, the current system architecture enhances the tolerance of the EPS to external perturbations in terms of phase-matching angle, temperature, and pump wavelength while maintaining high spectral brightness and quantum state fidelity. As evident from Table 1, while prior approaches each tick some of the boxes, our approach ticks all the salient boxes.

4.5 Conclusion

In conclusion, we have demonstrated a novel SPDC configuration where a hybrid solution that incorporates a lens-axicon pair, commonly available in an optics laboratory, was shown to have transformed the conventional SPDC annular ring into a new ring that is insensitive to perturbations, including the variation of the crystal temperature and laser wavelength. The generic experimental scheme, useful for the development of entangled photons at any desired wavelength and time scale, relaxes the stringent temperature stabilization of the crystal by five times and mode hopping and wavelength jitter by 100 GHz. Such demonstration opens up a new approach to robust SPDC sources for reliable deployment in the field demonstration of quantum optics experiments.

Chapter 5

Near video frame quantum sensing using Hong-Ou-Mandel interferometry

Hong-Ou-Mandel (HOM) interference, bunching of two indistinguishable photons on a balanced beam-splitter, has emerged as a promising tool for quantum sensing. The interference dip-width, thus the spectral-bandwidth of interfering pair-photons, highly influences the resolution of HOM-based sensors. Typically, the photon-pairs bandwidth, generated through parametric down-conversion, is increased using bulky and expensive ultrafast lasers, limiting their use outside the lab. Here we show the generation of photon-pairs with flexible spectral-bandwidth even using single-frequency, continuous-wave diode laser enabling high-precision, real-time sensing. Using 1-mm-long periodically-poled KTP crystal, we produced degenerate, high-brightness, photon-pairs with spectral-bandwidth of 163.42$\pm$1.68 nm resulting in a HOM-dip width of 4.01$\pm$0.04 μm to measure a displacement of 60 nm, and vibration amplitude of 205 ± 0.75 nm with increment (resolution) of $\sim$80 nm, and frequency of 8 Hz. Deployment of Fisher-information and maximum likelihood estimator enables optical delay measurement as small as 4.97 nm with precision (Cramér-Rao bound) and accuracy of 0.89 and 0.54 nm, respectively. The 17$\times$ enhancement of Fisher-information for the use of 1 mm crystal over 30 mm empowers the HOM-based sensor achieving any arbitrary precision (say ∼5 nm) in small number of iterations (∼3300) and time (19 minutes); establishing it's capability for real-time, precision-augmented, in-field quantum sensing applications.

5.1 Introduction

Quantum sensing and metrology is a rapidly growing field due to its outstanding features in measuring physical parameters with great precision and accuracy, outperforming the pre-existing technologies based on the principles of classical physics [28]. In recent years, quantum sensing has enabled the measurement of several key physical quantities, including the measurement of the electrical field [170], magnetic field [171], vacuum [172], temperature [173], and pressure [174] with unprecedented precision and accuracy. Among various quantum sensors as presented in Ref. [175], Hong-Ou-Mandel (HOM) interferometry, since its discovery [100], has found a large number of applications within quantum optics for a variety of advantages, including easy development and implementation, sensitivity only to photon group delay and not to phase shifts [176].

HOM interference, purely a non-classical phenomenon, is observed for two photons that are identical in all degrees of freedom, including spin, frequency, and spatial mode, when simultaneously entering on a lossless, 50:50 beam splitter through different input ports bunch together into one of the output ports. The coincidence probability between the two output ports shows a characteristic low or zero coincidence, known as the HOM interference dip, directly related to the level of indistinguishability or the degree of purity of the photons [177]. As a result, the change in coincidence counts can be treated as a pointer to estimate the time delay between photon properties, forming the basis of the HOM interferometer-based quantum sensors to sense any physical process influencing the photon delay. As such, efforts have been made to use the HOM-based quantum sensors to characterize the single photon sources [177], precise measurement of time delays between two paths [100, 178, 179], characterization of ultrafast processes[180], measurement of frequency shifts [181, 182] and the spatial shift [12]. On the other hand, the use of Fisher Information (FI), a measure of the mutual information between the interfering photons, has enabled the maximum precision to access a lower limit decided by the Cramér-Rao bound [183, 184]. In fact, the use of peak FI of the HOM interferometer, the point of maximum sensitivity, has enabled five orders of magnitude enhancement in the resolution of time delay measurements [178, 179, 185]. A typical FI-based measurement approach involves tuning the HOM interferometer for the peak FI point and performing iterative measurement to estimate any optical delay between the two photons. However, the number of iterations/measurements and hence the total time needed to reach the targeted precision decreases with the increase of FI value. On the other hand, the FI value can be increased by optimizing the parameters affecting the visibility and the width of the HOM interference dip. Despite the experimental demonstration of nanometer path length (few-attosecond timing) precision [178, 186] and a recent theoretical study on the tailoring of the spectral properties [187, 188] of photon pairs to achieve precision beyond the value reported in the laboratory condition, the width of the HOM interference dip governed by the bandwidth of the pair photons remained the limiting factor for optimal measurement precision [178, 179, 189, 190] in HOM interferometer based dynamic (real-time) or fast sensing applications. As such, ultra-broadband photon sources have long been hailed as a vital prerequisite for ultra-precise HOM interferometry. While the dynamic sensing process requires the single-photon source to have high brightness. On the other hand, a new strategy has been reported very recently where the frequency entangled photons have been used to produce the HOM beating effect [186]. As the frequency of the beating is proportional to the frequency detuning of the entangled photons [179, 186], the HOM beating, in conjunction with FI analysis, enabled the measurement of low-frequency (0.5 - 1 Hz) vibration with a precision of $\sim$2.3 nm using low (18000) number of photons pairs [186]. Despite the commendable precision measurement, such a strategy needs photons at two different wavelengths (one of them in infrared) and corresponding photon detection systems.

Nonlinear spontaneous parametric down-conversion (SPDC) [62, 191] process-based sources, where the annihilation of a high energy pump photon produces two daughter photons simultaneously, have evolved as a workhorse for quantum optics experiments, including HOM based sensors. However, the development of high brightness single-photon source requires a nonlinear crystal with high figure-of-merit (FOM) [192], long crystal length, and high intensity of the pump beam. As such, periodically poled nonlinear crystals can be used due to their high intrinsic FOM. However, the increase in the crystal length reduces the spectral bandwidth of the single-photon source. On the other hand, the increase of input pump intensity and spectral bandwidth of the generated photons using ultrafast laser [15] has its own limitations in terms of expensive and bulky system architecture for any practical on-field uses. Therefore, it is imperative to explore a continuous-wave (CW) pump-based bright single-photon source with high brightness and spectral bandwidth for ultra-precise HOM interferometry.

Recently, we reported a CW pumped high brightness, degenerate single-photon source at 810 nm using periodically-poled potassium titanyl phosphate (PPKTP) crystal in non-collinear, type-0, phase-matched geometry [11, 60]. Using the same phase-matching geometry, here, we report on the experimental demonstration showing the dependence of spectral bandwidth of degenerate SPDC photons and subsequent change in the HOM interference dip width on the length of the PPKTP crystal. Pumping the PPKTP crystal of length 1 mm, using a single-frequency, CW diode laser at 405.4 nm we observed the spectral width of the SPDC photons to be as high as 163.42 ± 1.68 nm producing a HOM interference dip having a full-width-at-half-maximum (FWHM) as small as 4.01 ± 0.04 µm. Using such small HOM interference dip width, we have dynamically measured the threshold vibration amplitude corresponding to the optical delay (twice the vibration amplitude of the piezo mirror) introduced between the photons as small as 205 ± 0.75 nm at a frequency as high as 8 Hz. On the other hand, the reduction of crystal length from 30 mm to 1 mm shows a 17 times enhancement in the magnitude of the peak FI value and achieves a targeted precision (say $\sim$5 nm or $\sim$16.7 attosecond optical delay) for a number of iterations/measurements (or the total experiment time) as low as 3300 (19 minutes).The experimental value of the FI throughout the report, if otherwise not defined, represents the FI of a single measurement/iteration. Completion of each measurement/iteration requires 100 milliseconds.

5.2 Theoretical Background

The spectral brightness of SPDC photons generated from a nonlinear crystal of length, L can be expressed as follows,

$$I_{SPDC} \sim \mathrm{sinc}^2\left(\Delta k L/2\right) \tag{5.1}$$

where Δk is the momentum mismatch among the interacting photons (pump and down-converted pair-photons) given as follows

$$\Delta k = k_p - k_s - k_i - \frac{2\pi m}{\Lambda} \tag{5.2}$$

Here, $k_{p,s,i} = \dfrac{2\pi n_{p,s,i}}{\lambda_{p,s,i}}$ is the wavevector and $n_{p,s,i}$ is the refractive index of the nonlinear crystal for the pump, λ_p, signal, λ_s, and idler, λ_i, wavelengths. Λ is the grating period of the periodically-poled nonlinear crystal to satisfy the quasi-phase-matching (QPM) condition. The odd integer number, m, is the QPM order. For maximum efficiency, we consider m = 1. The momentum mismatch between degenerate photons around the central angular frequency, $\omega_p/2$, can be represented as [193, 194]

$$\Delta k = \Delta k|_{\omega=\omega_p/2} + M|_{\omega=\omega_p/2}\Delta\omega + \frac{1}{2}K|_{\omega=\omega_p/2}\Delta\omega^2 + \ldots. \tag{5.3}$$

Assuming the QPM is achieved at degenerate SPDC photons with angular frequencies of pump, signal, and idler as ω_p, ω_s, and ω_i, respectively, for the grating period, Λ, the first term of the right-hand of Eq. (5.3) can be made zero. In this situation, owing to the energy conservation, $\omega_p = \omega_s + \omega_i$, the spectral bandwidth of the down-converted photons for the fixed pump frequency defined as $\Delta\omega = \Delta\omega_s = -\Delta\omega_i = \omega - \omega_p/2$, is decided by the second term, M = $[\partial k_s/\partial\omega - \partial k_i/\partial\omega]_{\omega=\omega_{p/2}}$, known as group-velocity mismatch. However, for degenerate ($\omega_s = \omega_i = \omega_p/2$), type-0 SPDC process, the group-velocity mismatch term vanishes or has negligible value. Under this condition, the spectral acceptance bandwidth of the SPDC photons is essentially determined by the much smaller third term of Eq. (5.3), commonly known as group-velocity dispersion with a mathematical form $K = \partial^2 k/\partial\omega^2|_{\omega=\omega_{p/2}}$. Under this condition, the spectral bandwidth of the SPDC photons can be written as,

$$\Delta\omega \propto \frac{1}{\sqrt{KL}} \tag{5.4}$$

Thus, one can utilize the length of the nonlinear crystal as the control parameter in the SPDC process to generate paired photons of broad spectral bandwidth near the degeneracy. On the other hand, it is well known that the optical delay range or the width, σ, of the HOM interference is proportional to the coherence length of the photon wave packets [121, 176] or the ensemble dephasing time of SPDC photons [195] bunching on the beam splitter. Although one can find the width, σ, of the HOM interference dip from the Fourier transform of the spectral density function of the paired photons [121, 196], we used the coherence length, L_c, of the photon wave packets and Eq. (5.4) to find the dependence of HOM interference dip width on the crystal length as,

$$\sigma \sim L_c \propto 2\pi c\sqrt{KL} \tag{5.5}$$

where c is the speed of light in vacuum. It is evident from Eq. (5.5) that the width, σ, of the HOM interference dip can be controlled by simply varying the crystal length even in presence of the single-frequency, CW diode laser as the pump.

5.3 Experimental setup

The schematic of the experimental configuration is shown in Fig. 5.1. A single-frequency, CW diode laser providing 20 mW of output power at 405.4 nm is used as the pump laser in the experiment. The spatial mode filtering unit comprised of a pair of fiber couplers (C1 and C2) and a single-mode fiber (SMF1) is used to transform the laser output in a Gaussian (TEM_{00} mode) beam profile. The laser power in the experiment is controlled using a combination of $\lambda/2$ plate (HWP1) and a polarizing beam splitter cube (PBS1). The second $\lambda/2$ plate (HWP2) is used to adjust the direction

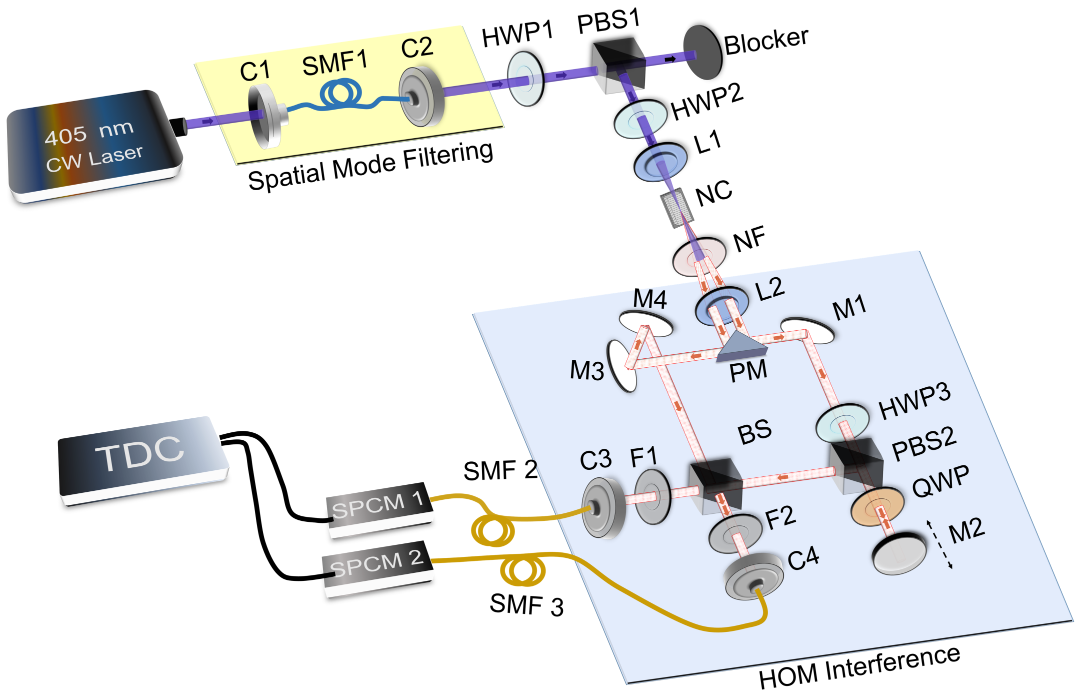

Figure 5.1: Schematic of the experimental setup. **C1-4**: fiber coupler, **SMF1-3**: single-mode fiber, **HWP1-2**: half-wave plate, **PBS1-2**: polarizing beam splitter cube, **L1-2**: lenses, **NC**: PPKTP crystal of grating period = 3.425 µm, **NF**: notch filter, **PM**: prism mirror, **M1-4**: dielectric mirrors, **QWP**: quarter wave plate, **BS**: 50:50 beam splitter cube, **F1,2**: high-pass filter, **SPCM1-2**: single photon counting module, **TDC**: time-to-digital converter.

of linear polarization of the pump laser with respect to the orientation of the crystal poling direction to ensure optimum phase matching conditions. The pump laser is focused at the center of the nonlinear crystal (NC) using the plano-convex lens, L1, of focal length, $f1$ = 75 mm to a beam waist radius of w_o = 58 µm. Periodically poled $KTiOPO_4$ (PPKTP) crystals of 1×2 mm^2 aperture but of five different interaction lengths, L = 1, 2, 10, 20, and 30 mm, are used as the nonlinear crystal (NC) in the experiment. The crystals have a single grating period of Λ = 3.425 µm corresponding to the degenerate, type-0 ($e \rightarrow e + e$) phase-matched parametric down-conversion (PDC) of 405 nm at 810 nm. To ensure quasi-phase-matching, the PPKTP crystals are housed in an oven whose temperature can be varied from room temperature to 200^{o}C with temperature stability of $\pm 0.1^o$C. The down-converted photon pairs, after separation from the pump photons using a notch filter (NF), are collimated using the plano-convex lens, L2 of focal length, $f2$ = 100 mm. Due to the non-collinear phase-matching, the correlated pair (commonly identified as "signal" and "idler") of down-converted photons have annular ring spatial distribution with signal and idler photons on diametrically opposite points. Using a prism mirror (PM), the signal and idler photons are separated and guided in two different paths and finally made to interact on the two separate input ports of a balanced beam splitter (BS). Since we need to vary temporal delay between the photons at the BS, and the translation of the optical component disturbs the alignment, we have devised the alignment preserving delay path consisting of a mirror, M1, $\lambda/2$ plate (HWP3), PBS2, $\lambda/4$ plate (QWP), mirror, M2 on the delay stage, and finally, the beam splitter, BS. The $\lambda/2$ plate rotates the photon's polarization state from vertical to horizontal to ensure complete transmission through PBS2. The $\lambda/4$ having the fast axis at +45^o to its polarization axis transforms the photon polarization (horizontal) into circular (left circular). However, the handedness of the photon polarization gets reversed (right circular) on reflection from the mirror, M2, at normal incidence. On the return pass through the $\lambda/4$ plate, the right circular polarized photons convert into vertical polarized photons and are subsequently reflected from the PBS2 to one of the input ports of the BS. Due to the normal incident of the photons on the moving mirror, M2, the varying delay of the photons does not require tweaking of the experiment. The combination of the piezo-electric actuator (PEA) (NF15AP25), placed on a motorized linear translation stage (MTS25-Z8), is used to provide both fine and coarse optical delay. The range (resolution) of the PEA and motorized linear stage as specified by the product catalog is 25 μm (0.75 nm), and 25 mm (29 nm), respectively. Throughout the report, the optical delay of the photon is twice the displacement of the mirror, M2, if otherwise mentioned. On the other hand, the photons of the other arm are guided using mirrors, M3 and M4, to the second input port of BS such that the optical path length of both arms are the same. The photons from the output ports of the BS, after being extracted by long pass filters (F1, F2), are coupled into the single mode fibers, SMF2 and SMF3, through the fiber couplers, C3, and C4, respectively. The collected photons are detected using the single-photon counting modules, SPCM1-2 (AQRH-14-FC, Excelitas), and counted using the time-to-digital converter (TDC). All optical components used in the experiment are selected for optimum performance at both the pump and SPDC wavelengths. All the data is recorded at a typical pump power of 0.25 mW with a coincidence window of 1.6 nanoseconds.

5.4 Characterization of HOM interference

First, we verified the dependence of HOM characteristics on the length of the non-linear crystal. Keeping the input pump power to the crystal and the temporal coincidence window of the TDC constant at 0.25 mW and 1.6 ns, respectively, we have recorded the variation of coincidence counts as a function of the relative optical delay between the photons. As evident from Fig. 5.2(a), the variation of coincidence counts with the relative optical path delay has the characteristic HOM interference dip profile, approximated by an inverted Gaussian function (owing to the temporal Gaussian profile of signal and idler). However, it is interesting to note that the HOM visibilities calculated using the formula given in [178] remain constant in the range of 86 - 94 % despite appreciable variation in the span of the HOM interference dip profile.

To gain further insights, we measured the FWHM width of the HOM interference dip and estimated the corresponding spectral bandwidth of the photon pairs using Eq. (5.4) and (5.5). The results are shown in Fig. 5.2(b). It is evident from Fig. 5.2(b) that the HOM interference dip has FWHM width (red dots) of 4.01 $\pm$ 0.04, 6.16 $\pm$ 0.05, 13.33 $\pm$ 0.40, 17.32 $\pm$ 0.08 and 21.19 $\pm$ 0.13 μm corresponding to the estimated FWHM spectral bandwidth (black dots) of SPDC photons of 163 $\pm$ 1.68, 106 $\pm$ 0.93, 49 $\pm$ 1.44, 38 $\pm$ 0.20 and 30 $\pm$ 0.18 nm for the crystal lengths of 1, 2, 5, 10, 20, and 30 mm are in close agreement with the Eq. 5.5 (solid black lines). Using the available pump power, we experimentally measured the spectral bandwidth of the SPDC photons using the spectrometer (HR-4000, Ocean Optics) to be $\sim$30 nm, same as our previous report [11] and $\sim$37 nm for 30 mm and 20 mm long crystals, respectively

The relatively low parametric gain has restricted the experimental measurement of the SPDC spectrum for smaller crystal lengths. However, it is important to note that the experimentally measured spectral bandwidth is matching with the estimated spectral

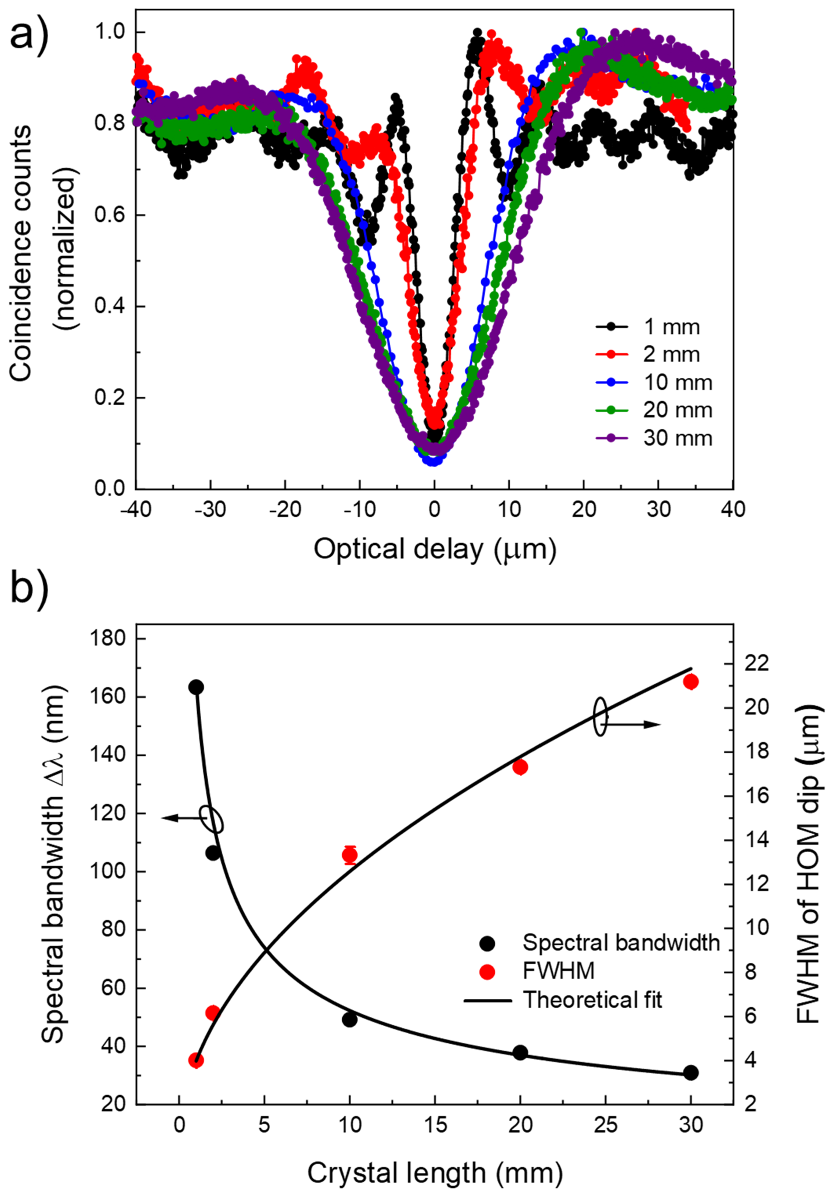

Figure 5.2: a. Variation of HOM interference dip profiles with the length of the non-linear crystals. b. Dependence of spectral bandwidth (black dots) and the FWHM width of HOM interference profile (red dots) of SPDC photons on the length of the non-linear crystal. The solid black line is the theoretical fit to the experimental data.

bandwidth as shown in Fig. 5.2(b). Interestingly, the decrease of crystal length from 30 mm to 1 mm results in a decrease (increase) of HOM interference dip width (spectral width of SPDC photons) by more than five times. As a result, one can see the sharp variation (see black and red dots of Fig. 5.2(a)) in the coincidence counts for the small changes in the optical delay away from the zero-point optical delay for HOM interference with smaller dip width. Such amplification in the rate of change of coincidence counts with optical delay, i.e., the increase of sensitivity of the HOM interferometer with the decrease in crystal length, can be useful for designing HOM interferometer-based sensor to measure any physical process influencing the optical delay between the photons.

To gain further perspective, we have selected half of the HOM curve of Fig. 5.2(a) showing coincidence counts variation from minimum to maximum with positive optical delay for crystal lengths, L = 1, 2, 10, 20 and 30 mm. The results are shown in Fig. 5.3(a). Since the maximum coincidence counts per second at a fixed pump power of the HOM curve directly depend on the pair generation rate and hence the interaction length of the non-linear crystal used, for comparative study of the slopes of HOM curves for different crystal lengths, we have normalized the coincidence counts with their maxima. It is visually evident from Fig. 5.3(a) that the slope of the HOM curve is gradually increasing with the decrease of crystal length from L = 30 mm to 1 mm. However, for quantitative estimation, we have used a linear fit (solid lines) to the experimental data (points) as shown in Fig. 5.3(a), and measured the variation of the HOM dip gradient with crystal length. The results are shown in Fig. 5.3(b). It is evident that the gradient of the HOM curve decreases (red dot and line) with the crystal length from a maximum of 0.215 μm^{-1} for L = 1 mm to 0.051 μm^{-1} for L = 30 mm. Since the slope of the HOM curve reflects the measurement sensitivity, we can conclude that for the measurement of any physical parameter influencing the relative optical delay between the photons with high sensitivity, one needs a HOM interferometer with a shorter nonlinear crystal length.

However, it is well known from the literature [197, 198] that the gain of the parametric process is a function of crystal length. Therefore, a decrease in crystal length to access the higher sensitivity of the HOM-interferometer-based sensor results in a decrease in the generation rate of paired photons. To get a better perspective on the generation rate of paired photons useful for quantum sensing, we have measured the coincidence counts with the change in crystal length while keeping the pump focusing waist radius

(w_p = 29 μm) and waist radius ($w_{i/s}$ = 39 μm) of the collected signal/idler constant. As shown in Fig. 5.3(b), the coincidence counts (black dot and line) for the fixed pump power of 0.25 mW increase from 89.5 kHz to 245.3 kHz for crystal lengths ranging from L = 1 mm to 30 mm with a maximum of 329 kHz for crystal length of L = 10 mm. This is due to the fact that the pump focusing and collection beam waist are optimized for the crystal length, L = 10 mm. While one can access more counts for each crystal length by utilizing the optimum focusing conditions, it is evident from the current study that despite the use of thin crystal lengths (required for the high sensitivity of the quantum sensor), the coincidence counts are sufficiently large for practical applications. In terms of the coincidence counts, the slopes of the HOM curve for 1 mm and 30 mm crystals are found to be 450 μm^{-1} and 260 μm^{-1}, respectively, at a pump power of 0.25 mW and exposure time at 20 ms. Although in the present study, we have collected the photons with a single mode fiber, thus eliminating the photons generated in higher order modes, it is observed in literature [199] that the use of thin crystal can lead to the generation of broadband spatial modes. Therefore, the use of broadband spatial modes generated in the current experiment can lead to additional experiments in the future. On the other hand, here, we have used a CW diode laser to implement the system in outdoor applications. However, using an ultrafast pump laser in combination with the thin crystal for lab-based experiments, one can further enhance the sensitivity of the HOM interferometer due to the increase of overall spectral bandwidth (decrease of HOM interference dip width) of the down-converted photons and pair photon generation rate for small crystal length. Similarly, with the use of periodically-poled crystals with chirped grating, one can use long crystal lengths to generate broadband pair photons with a high generation rate [200].

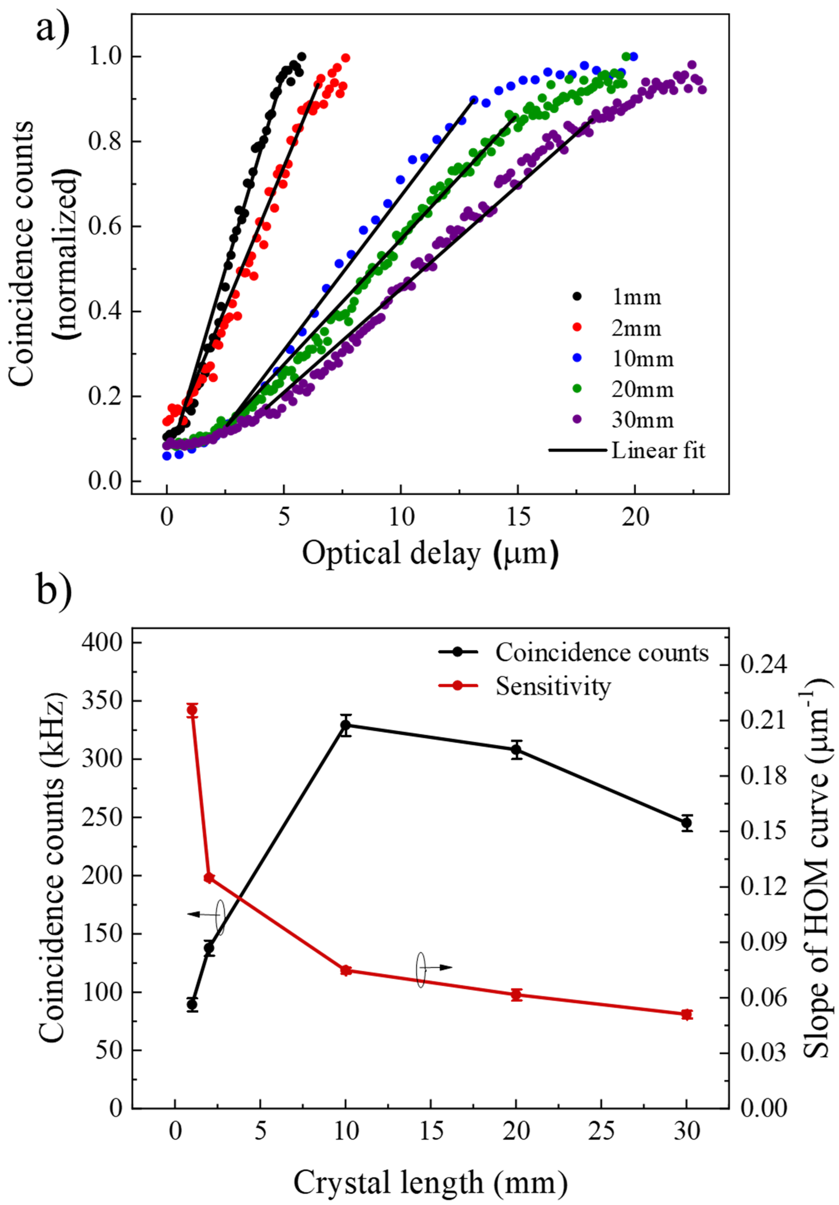

Figure 5.3: a. Crystal length dependent variation in the slope of coincidence counts of HOM interferometer. Solid lines are linear fit to the experimental results (dots). b. Variation of coincidence counts and slope of HOM interferometer as a function of crystal length for a fixed pump and collection beam waist radii and pump power

.

5.4.1 Displacement sensing using HOM interferometer

Knowing the dependence of the sensitivity on the crystal length, we have studied the performance of the HOM interferometer to measure the static displacement of the mirror, introducing an optical delay between the photons. Using the 1 mm long PPKTP crystal resulting in HOM interference dip width of 4.01 ± 0.04 µm, we have moved the mirror using the motorized stage to a displacement of ~ 1.25 µm away from the zero-optical delay position. This translation resulted in a positive optical delay of $\sim$ 2.5 µm corresponding to the region having maximum sensitivity of the HOM region of the sensor. We moved the mirror in a step of 60 nm (resulting optical delay of 200 attoseconds) and measured the coincidence counts. The results are shown in Fig. 5.4. It is evident from Fig. 5.4(a), the displacement of the mirror by 60 nm results in the change of the coincidence counts of more than 50 per 20 ms of integration time. Such a large change in the coincidence count, much higher than the dark count and accidental counts, confirms the possibility of measurement of static displacement as low as 60 nm. Such a change in the coincidence count is easily detectable, confirming the displacement measurement as small as 60 nm. Further, to confirm the reliability of the measurement, we measured the temporal variation of the coincidence counts over 10 minutes for each mirror position. It is evident from Fig. 5.4(b), that the temporal variation (with standard deviation $\sim$ 7.4%) of the coincidence counts due to various parameters, including the laser intensity fluctuation, air current, and local temperature instability in the laboratory, is much smaller than the change in the coincidence counts due to the static displacement of the mirror. The possibility of smaller static displacement can be possible by suitably reducing the fluctuation of the coincidence counts in the experiment.

5.4.2 Calibration of piezo actuator

After successful characterization and static displacement measurement, we used a piezo-electric actuator (PEA) (NF15AP25), having a travel range of 25 µm for the

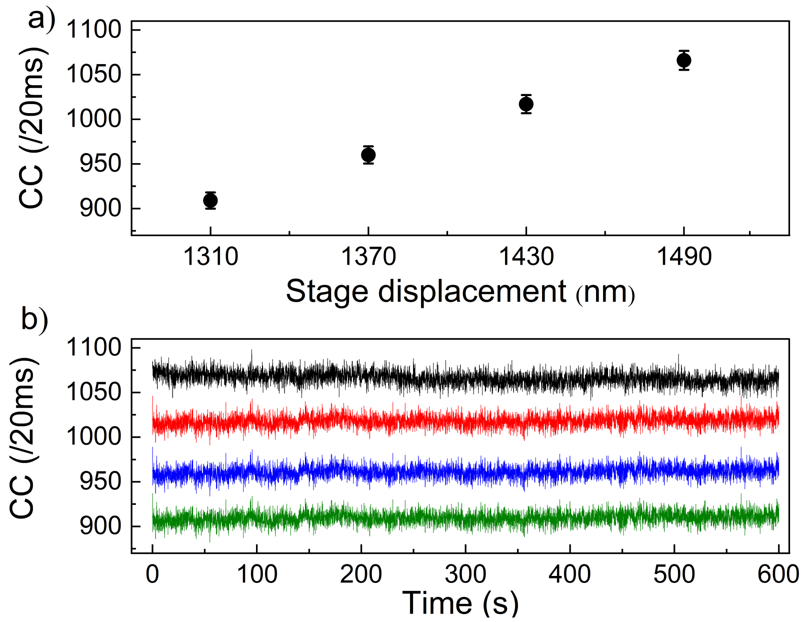

Figure 5.4: a. Variation in the coincidence counts (CC) with nanometer displacement of the optical delay mirror, M2. b. Temporal stability of coincidence counts at different positions of the delay mirror, M2.

applied voltage 0 - 75 V to study the performance of the HOM interferometer for dynamic optical delay or mirror vibration sensing applications. However, due to the unavailability of closed-loop feedback for the PEA, we had to calibrate the PEA to estimate the displacement with the applied voltage. In doing so, we have attached the mirror M2 (see Fig. 5.1) to PEA placed over the motorized linear translation stage (MTS25-Z8). Using a crystal of length 20 mm corresponding to the HOM curve represented by the green dots in Fig. 5.2, we have adjusted the initial position of the linear stage corresponding to a positive delay of $\sim$10 μm so that the coincidence count is 50% of maximum value. We moved the linear stage by $\sim$0.5 μm corresponding to the optical delay of $\sim$1 μm towards the zero-delay point resulting in a change in the coincidence counts. Such change in the coincidence counts is reset by increasing the applied voltage to the PEA. Under this condition, the applied voltage to the PEA makes a displacement corresponding to the displacement of the linear stage in the opposite direction. We have repeated this exercise in steps of $\sim$0.5 μm up to the allowed PEA voltage of 75 V with the results shown in Fig. 5.5. It is evident from Fig. 5.5 that the displacement (blue dots) of the PEA is linear to the applied voltage producing a

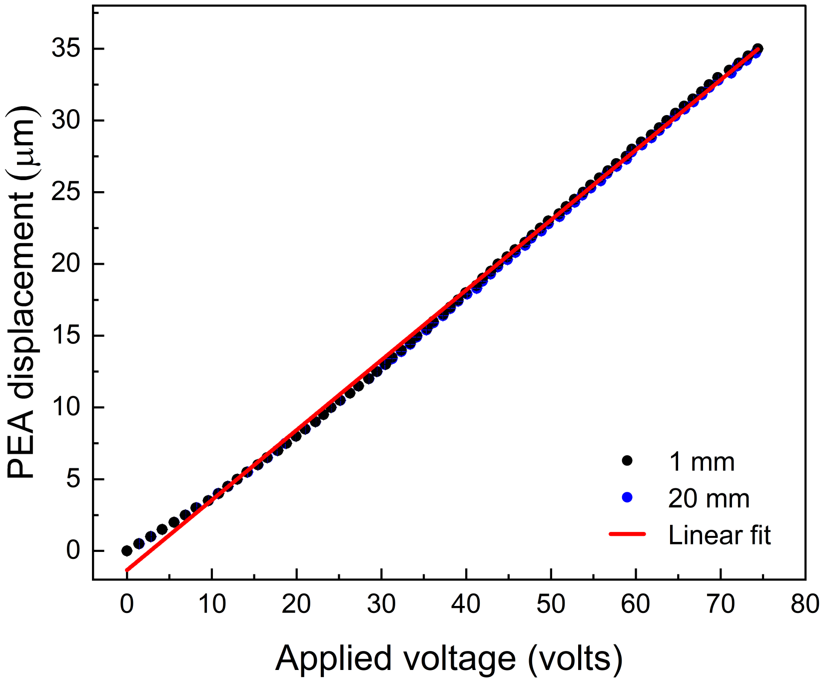

Figure 5.5: Linear displacement of the PEA stage as a function of applied voltage.

maximum displacement of 35 μm, more than the manufacturer's specification (25 μm) for the maximum allowed voltage of 75 V. Using the linear fit (red line) to the experimental data (black dots) we find the displacement of the PEA to be 0.48 ± 0.02 μm per volt. As expected, the calibration of PEA using the HOM interferometer based on a 1 mm long crystal (black dots) coincides with the results obtained using the 20 mm long crystal (blue dots).

5.4.3 Dynamic vibration sensing using HOM interferometer

Having the calibration data for the piezo for static displacement, we have studied the performance of the HOM interferometer for a dynamic signal. In doing so, we have used the 1 mm long PPKTP crystal corresponding to the HOM interference dip width (FWHM) of 4.01 μm and adjusted the initial positive delay by a value of $\sim$3 μm. Driving the PEA with a periodic voltage signal in a triangular wavefront of controllable frequency and amplitude, we have recorded the temporal variation of the coincidence counts of the HOM with the results shown in Fig. 5.6. As evident from Fig. 5.6(a), the vibrations of the PEA with a periodic triangular signal of period 1 Hz and the peak-to-peak voltage of 1 V corresponding to a peak-to-peak optical delay of $\sim$1.0 µm, as estimated from the calibration data of section. 5.4.2), produces a peak-to-peak variation in the coincidence counts of $\sim$400 over the mean value of 960 at a period of 1 Hz, the same as the driving frequency. Further, we changed the peak-to-peak vibration amplitude of PEA from the calibration data of Fig. 5.4.2 and measured the peak-to-peak optical delay from the coincidence counts with the results shown in Fig. 5.6(b). We have repeated this exercise twice and termed the results as set-1 (red data points) and set-2 (blue data points). As evident from Fig. 5.6(b), the peak-to-peak optical delay (which is twice the displacement of the PEA) measured using the change in the coincidence counts of HOM exactly follows the set delay at a slope of 0.835 ± 0.004. Ideally, the slope should have a value of 1 to maintain one-to-one correspondence of the set and measured values. The discrepancy between the experimental slope with respect to the ideal value can be attributed to the error in the coupling of the applied voltage to the PEA and piezo hysteresis [201, 202], which can be minimized by the unidirectional motion of the PEA and allowing sufficient relaxation time to achieve the intended position decided by the input voltage (see the PEA calibration, as shown in Fig. 5.5, having the slope near 1). Since the slope of Fig. 5.6(b) is a very important parameter for dynamic sensing applications, we have taken care of the deviation of the slope value from the ideal value in all experimental measurements throughout the manuscript. While increasing the PEA vibration amplitude through the applied voltage signal, we realized that the threshold (to replicate the shape of the input waveform exactly) peak-to-peak vibration amplitude, which can be measured dynamically using this technique, is found to be 205 ± 0.75. Subsequently, the average maximum attainable resolution between two consecutive vibration amplitudes is found to be $\sim$ 80 nm. However, one can access smaller peak-to-peak vibration amplitude ($<$ 50 nm) (without replicating the shape of the input wavefront) from the peak-to-peak variation of the coincidence counts. As the HOM interferometer deals with single photons, it is essential to integrate the detected coincidence events for a substantial time to get a tangible number of coincidence counts while making any measurement. Again the required integration time is highly influenced by the brightness of the single-photon source. In the current experiment, we used high brightness single photon source based on PPKTP crystal [11, 60]. As a result, we can keep the integration time as low as a few tens of milliseconds. Here, we have also tested the HOM interferometer to measure the vibration frequency of the PEA.

Keeping the experimental parameters the same as previous, we have changed the fre-

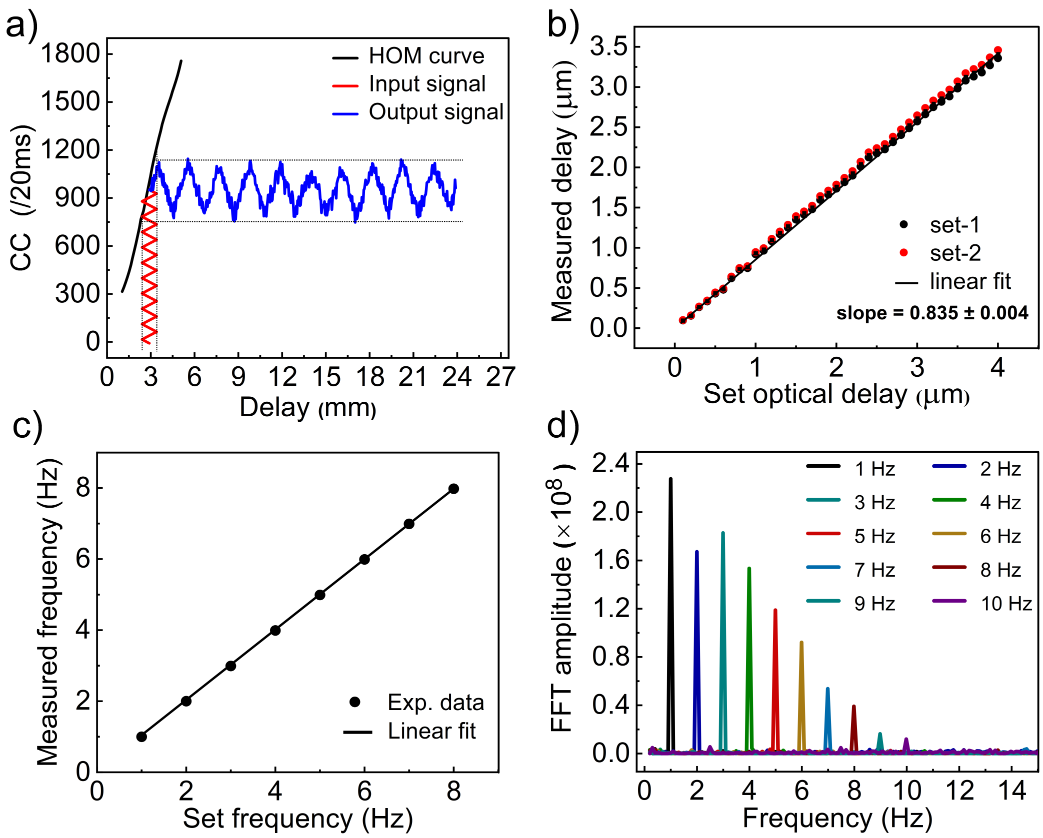

Figure 5.6: Vibration measurement using HOM interferometer sensor. a. Variation of coincidence counts for periodic triangular voltage signal of peak-to-peak amplitude 1 V at 1 Hz applied to the PZT stage. b. Variation of PEA displacement, and c. driving frequency measured from the coincidence counts with respect to the set values. d. Fast Fourier transformation of the time-varying coincidence counts measuring the driving frequency of the applied voltage signal.

quency of the triangular voltage signal to the PEA at the constant peak-to-peak voltage of 1 V corresponding to the optical delay of $\sim$1.00 µm. While we adjusted the set frequency from the function generator, we recorded the temporal variation of the coincidence counts for each driving frequency and performed the fast Fourier transform

(FFT) to experimentally measure the driving frequency. As evident from Fig. 5.6(c), the measured frequency using the coincidence data exactly matches the driving frequency. The linear fit (line) to the experimental data (dots) shows a slope of 1, confirming the reliable measurement of the frequency of the driving field. However, we have restricted our measurement to 8 Hz as the FFT signal amplitude, despite having the peak at the driving frequency, as shown in Fig. 5.6(d), decreases with the increase of the driving frequency. Such a decrease can be understood as follows. In FFT analysis, the accuracy depends on the number of acquired samples from the experimental data. For example, the higher resolution in estimating the driving frequency using FFT analysis requires many data points. Again, the number of samples/data points can be increased by increasing the sampling rate. However, in the present case, the sampling rate is restricted to 50 Hz due to the requirement of a high exposure/integration time of 20 milliseconds limited by the generation rate of the SPDC source and the processing speed of the TDC. Although we have 50 data points to perform FFT analysis for a driving frequency of 1 Hz, the available data points vary inverse to the driving frequency as $M = 50/f$, where M is the number of samples available for FFT analysis and f is the driving frequency. As a result, it becomes difficult to retrace the waveform of the input signal at an increased frequency which leads to the gradual decrease in the FFT signal amplitude (increase in signal-to-noise, SNR, value) and the subsequent appearance of its second harmonic peak. Further, an increase in the driving frequency requires a decrease in data integration time (to achieve a higher sampling rate) through the increase of the photon generation rate of the source and the use of TDC with low data acquisition latency. However, in the best-case scenario, one can, in practice, use HOM interferometer-based sensor to measure dynamic vibration signals of unknown frequency restricted to a few tens of hertz only.

After complete characterization of the HOM interferometer-based quantum sensor in terms of static and dynamic displacement measurement, we verify its performance to measure any arbitrary vibration signal. We adjusted the initial position of the optical delay mirror, M2, like the previous studies, to access the high-sensitivity region of the HOM interference dip based on a 1 mm-long PPKTP crystal. Considering the initial position as the zero displacement point, we drove the PEA with an external voltage signal to the PEA in the triangular waveform of varying amplitude (peak-to-peak voltage range of 0.7 to 2 V) and frequency (1 Hz to 8 Hz). The results are shown in Fig. 5.7. As evident from Fig. 5.7(a), the displacement of the PEA measured from the calibration curve (see Fig. 5.5) shows a temporal variation in both amplitude and frequency, confirming the arbitrary vibration. However, as evident from Fig. 5.5(b), the variation of the coincidence counts recorded for an integration time of 20 ms exactly follows the applied signal. Such observation confirms the possibility of measurement of any arbitrary vibration, for example, low amplitude and frequency seismic S- and P-waves, using a HOM interferometer-based quantum sensor.

The current study establishes the potential of the HOM interferometer as a quan-

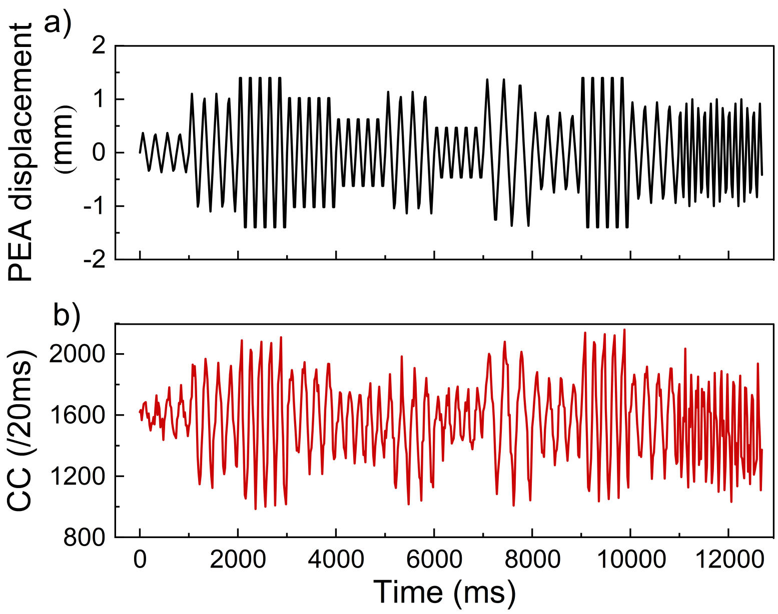

Figure 5.7: a. Temporal variation of PEA displacement and b. corresponding variation in the coincidence counts of the HOM interferometer for the external vibration.

tum sensor for real-time detection of time-varying signals in the frequency ranging from 1 Hz to 8 Hz and any physical process producing optical delays as low as 0.41 ± 0.06 μm with a precision of ∼0.19 μm. While the frequency range can further be increased to tens of hertz by reducing the exposure time of the measurement, the precision in the real-time measurement of lower optical delay is fundamentally limited by the statistical and systematic error, especially at lower variation in coincidence counts

[21]. As such, one needs to explore the statistical concept of Fisher information to attain a precision that has a lower limit governed by the Cramér-Rao bound [178, 179, 185].

5.5 Precision augmented sensing

The ultimate limit on the precision in measurement is decided by the Cramér-Rao bound [183, 184] defined as,

$$Var(\tilde{x}) \geq \frac{1}{NF(x)} \tag{5.6}$$

where $\tilde{x}$ represents an unbiased estimator to estimate the physical parameter and var($\tilde{x}$) is the variance in the measurement. $F(x)$ represents the Fisher information (FI), a metric describing the amount of information available from a probability distribution of an unknown parameter, for estimating the information of the parameter x in a single measurement, and N is the total number of measurements performed in the experiment. In the case of HOM interference, the mathematical form of FI is primarily determined by the temporal mode profile of the signal and idler photons [178]. As the down-converted photons generated through the type-0 SPDC process have a Gaussian spectral profile, the FI can be modeled as,

$$F = \frac{4s^2\alpha^2(\gamma-1)^2(1+\gamma)}{(e^{s^2}-\alpha)(\alpha-\alpha\gamma+e^{s^2}(1+3\gamma))\sigma^2} \tag{5.7}$$

here, α, γ, and σ represent the HOM interference visibility, the rate of loss in photon detection, and the FWHM width of the HOM curve, respectively. $s = \frac{x}{\sigma}$ is the parameter controlling the distinguishability of the photon arriving at the beam splitter.

As evident from Eq. (5.7), keeping all parameters constant, one can increase the magnitude of FI, F by employing the HOM interference of smaller dip width (σ). Again, it is evident from Eq. 5.5 that for a given laser parameter, the dip width of the

HOM interference varies with the square root of the crystal length. Since the crystal length, a physical parameter controllable in the experiment, using Eq. (5.5) in Eq. (5.7), we can derive a general expression for FI in terms of crystal length, L, as,

$$F = \frac{4x^2\alpha^2(\gamma-1)^2(1+\gamma)}{A^4(e^{\frac{x^2}{A^2L}}-\alpha)(\alpha-\alpha\gamma+e^{\frac{x^2}{A^2L}}(1+3\gamma))L^2} \tag{5.8}$$

Here, A is a constant determined by the crystal properties. It is evident from Eq. (5.6) that for a fixed number of measurements/iterations, N, the precision can be enhanced, or for a fixed precision, the number of measurements/iterations, N, can be reduced with the increase of the magnitude of F while saturating the Cramér-Rao bound. Therefore, Eq. (5.8) sets the foundation for our further study of precision augmented quantum sensing.

To get a better perspective on the dependence of FI on the crystal length, we have plotted Eq. (5.8) as the function of optical delay, x while keeping the experimentally measured values of α and γ as constant. We have used crystal lengths, $L = 1$, 2, 10, 20, and 30 mm, as available in our lab. The results are shown in Fig. 5.8(a). As evident from Fig. 5.8(a), the FI has the double-peak profiles for HOM visibility $\alpha < 1$. It has been previously observed [178] that the HOM visibility, α influences the magnitude and the separation between two peaks of FI, respectively. However, in the current experiment, we observed that for a fixed value of HOM interferometer visibility, the shape and peak value of FI depend on the value of HOM interference dip width, σ. As evident from Fig. 5.8(a), the decrease in the width of the HOM interference dip due to the decrease of crystal length (see Eq. (5.5)) not only reduces the separation of the two peaks of FI but also show a substantial increase in their respective peak values. To put things in perspective, using the experimental parameters in Eq. (5.8), we estimated the peak values of FI for crystal lengths 1, 2, 10, 20, and 30 mm. The results are shown in Fig. 5.8(b).

The solid dots represent the peak value of FI, calculated using experimentally measured values of α, γ, and σ for each crystal length. On the other hand, the theoretical fit to the experimental results is calculated using Eq. 5.8 for fixed values of α and γ for

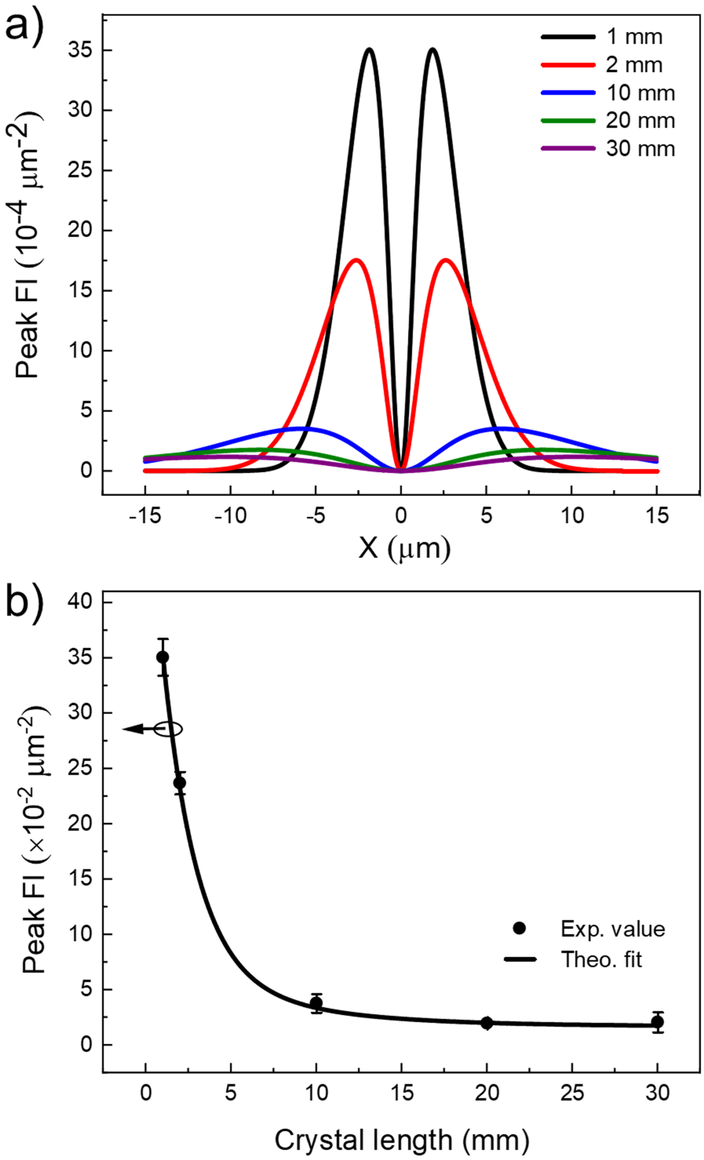

Figure 5.8: a. Variation of Fisher information as a function of optical delay, x, between the signal and idler photons for different crystal lengths. b. Dependence of the peak FI value with the length of the nonlinear crystal. Solid line is the theoretical fit (Eq. 5.8) to the experimental data.

all crystal lengths. It is evident from Fig. 5.8(b) that the peak value of FI (black dots) decreases from 35.06 $\pm$ 1.65) x 10^{-4} μm^{-2} to (2.07 $\pm$ 0.19) x 10^{-4} μm^{-2} for the increase of the crystal length from 1 mm to 30 mm due to the corresponding increase in the FWHM width of the HOM interference dip from 4 μm to 21.2 μm (see Fig. 5.2). Such observation clearly shows the enhancement in peak value of FI (here 17×) by simply reducing the nonlinear crystal length (here 1/30) even using a single-frequency diode laser. It is also interesting to note that the current peak value of FI shows a $\sim 24\times$ enhancement as compared to the FI value under similar measurement conditions using an ultrafast laser [178], with further possibility of enhancement by using an ultrafast laser generating SPDC photons in a thin nonlinear crystal. Such an increase in the peak value of FI can be useful in faster saturation of the Cramér-Rao bound as defined in Eq. (5.6) at the lower number of measurements/iterations to achieving a predefined precision in the measurement of optical delay.

5.5.1 FI based measurement

The precise estimation of a physical parameter such as optical delay, x, can be obtained through the maximum likelihood estimator [178]. In the current study, the estimator of the maximum likelihood function for measuring the optical delay can be defined as,

$$\tilde{x} = \pm\sigma\sqrt{ln\left(\frac{(N_1+N_2)}{N_1-N_2(\frac{1+3\gamma}{1-\gamma})}\right)} \tag{5.9}$$

Here, N_1 and N_2 represent singles and coincidence counts, respectively. The optical delay introduced between the signal and idler photons can be estimated using Eq. (5.9) with the proper knowledge of N_1 and N_2. To perform the FI-based measurements on the small optical delay between the paired photons, we first calibrated the 1 mm long PPKTP crystal-based HOM interferometer to estimate the parameters, α, γ, and σ. We performed 16 scans of the HOM dip to ascertain the precise values of these defining parameters of the HOM interferometer. We tried to resolve between two selected points on the HOM interference curve having the positive optical delays of, say, x_1 and x_2 with a separation of $\sim$5.51 nm apart. The optical delay corresponding to the maximum peak value of FI lies between points x_1 and x_2. We set the voltage to the PEA according to the calibration data shown in Fig. 5.5 to make the back-and-forth movement between the positions x_1 and x_2 and recorded the singles count, N_1, and coincidence counts, N_2 at both points. Although the exposure time for this iterative measurement was set to 50 ms, the electronic response and delay of the Piezo controller and TDC restricted the effective data acquisition frequency to $\sim$6 Hz. Using all the experimental parameters in Eq. (5.9), we have estimated the values of x_1 and x_2 with the results shown in Fig. 5.9. As evident from Fig. 5.9(a), the cumulative estimates for x_1 (black line) and x_2 (red line) with the increase in the number of iterations/measurements show a drift due to the drift in the piezo position over the measurement time. However, the separation between the estimated values of x_1 and x_2, as shown by the inset image of Fig. 5.9(a), remains almost constant. We have estimated the separation between the set points as a function of the number of iterations with the results shown in Fig. 5.9(b). As evident from Fig. 5.9(b), we observe a large uncertainty in estimating the separation between the set positions for the initial measurements, which settles quickly toward the set value with the increase in the number of measurements/iterations. For the set separation value of $\delta x \sim 5.51 \pm 0.75$ nm estimated from the difference in the applied voltage to the PEA, we measured the optical delay to be 4.97 ± 0.89 nm even for the experimental measurements/iterations as low as 3300 (as shown in the inset of Fig. 5.9(b)). The achievable precision for the complete range of the measurements can be calculated as $\sqrt{Var(\delta\tilde{x})/N}$, where N is the total number of independent measurements performed for the cumulative estimation.

The minute drift in the cumulative estimated data (see from Fig. 5.9(a)), due to the drift in the piezo position over the large experiment time (as high as $\sim$ 139 minutes), can easily be mitigated by adjusting the frequency of back-and-forth movement of $\sim$ 6 Hz; a rate much faster than the rate of drift in the position of PEA. Despite such drift, it is to be noted that the PEA position remains well inside the region ($\sim$ 200 nm), having maximum FI value, adding to the reliability of the acquired data. Although we have performed about 25000 independent measurements over an experiment time of $\sim$139 minutes, one can easily notice from Fig. 5.9(b) that the true value has been achieved through the saturation of Cramér-Rao bound for the experimental measurements/iterations as low as 3380 corresponding to the experiment time as low as $\sim$19 minutes. This was possible due to the increase of the peak FI value through manipulating the spectral bandwidth of the SPDC photons. Further reduction in the experiment time

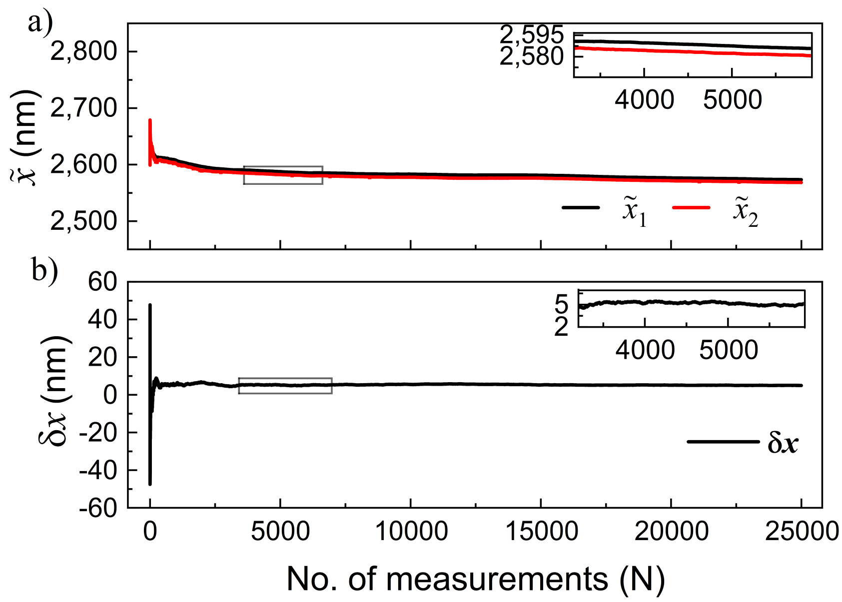

Figure 5.9: Variation of a. cumulative estimates for the PZT positions, x_1 and x_2, and b. the estimated optical delay between signal and idler photons as a function of the number of measurements.

to reach such high sensitivity can be possible by further enhancing the FI using the ultrafast pump laser generating SPDC photons in thin crystals.

We repeated these measurements over a wide range of optical delays using PPKTP crystals of lengths 1, 2, 10, 20, and 30 mm. The estimated optical delays calculated from the cumulative estimates are shown in Fig. 5.10. As evident from Fig. 5.10, the experimental values of the cumulative estimates (solid dots) of the optical delay in the range of ∼3 nm to ∼80 nm measured using different crystal lengths exactly follow the set true value of δx (black line) derived from the peak-to-peak amplitude of the voltage signal applied for the back-and-forth motion of the PEA. It is worth mentioning that we have incorporated the piezo hysteresis as shown in Fig. 5.6 (b) in all the measurement data. The close agreement of the experimental values of the cumulative estimate with the set true values of δx, for all crystal lengths confirms the reliability and robustness of the current experimental scheme.

We further experimentally verify the dependence of the value of FI and the minimum number of required iterations/measurements while achieving a fixed precision. It is evident from Eq. (5.6) and Eq. (5.8) that for a given precision, the increase in

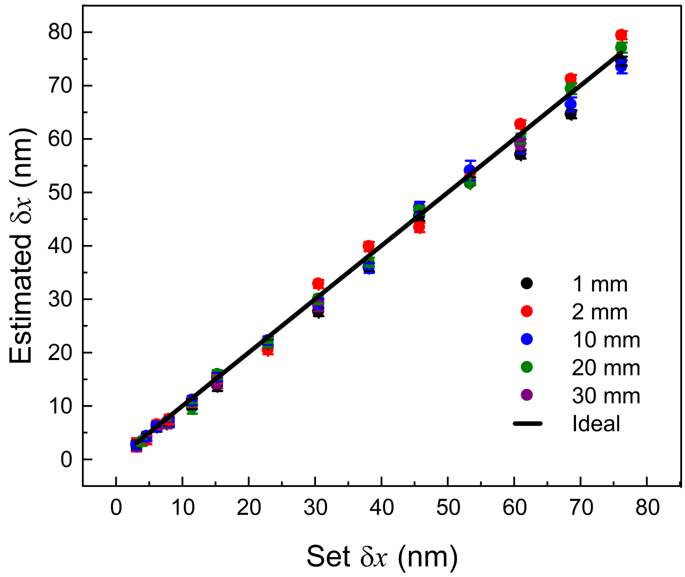

Figure 5.10: Variation of optical delay measured using the FI analysis with the set optical delays for different crystal lengths. Solid line represents the true values.

the value of peak FI reduces the required number of iterations/measurements. For experimental verification, we set, for example, the precision of the optical delay between the pair photons to be ~5 nm and observed the minimum number of measurements/iterations (N) required to achieve this precision for all available PPKTP crystals. The results are shown in Fig. 5.11. For better understanding, we have also shown the variation of the peak value of FI with crystal length. As evident from Fig. 5.11, to achieve a set precision, the number of minimum iterations/measurements (red dots) increases from 3380 to 17500 for the increase of crystal length from 1 mm to 30 mm due to the subsequent decrease of peak FI value (black dots) from ~35 x 10^{-4} to ~2 x 10^{-4} μm^{-2}. It is interesting to note that the inverse of the product of the number of minimum iterations/measurements (N) and the square root of the peak value of FI forming the precision [179] is exactly matching with set precision and independent to the increase of crystal length from 1 mm to 30 mm. The black line is the theoretical fit to the experimental data as reproduced from Fig. 5.8. From this experiment, it is evident that a further increase of the peak value of FI through the increase of spectral bandwidth of the SPDC photon using of ultrafast pump can lead to the realization of FI-based

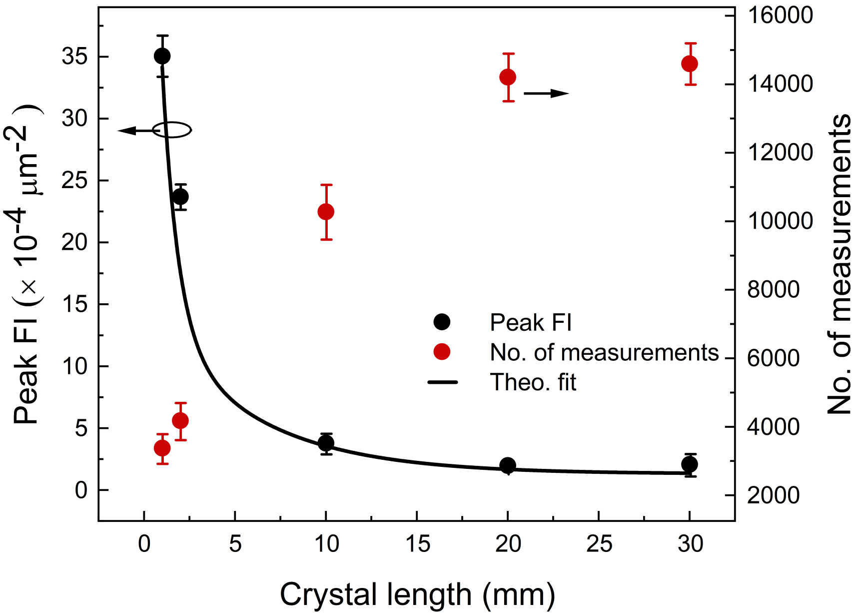

Figure 5.11: Variation of peak FI value and the corresponding number of iterations/measurement required to achieve a fixed precision as a function of crystal length.

ultra-sensitive measurements in real-time applications.

5.6 Conclusions

In conclusion, we have experimentally demonstrated easy control in the spectral bandwidth of the pair-photons through proper selection of the length of the non-linear crystal. Using a 1 mm long PPKTP crystal, we have generated paired photons with spectral width as high as 163.42±1.68 nm even in the presence of a single-frequency, CW, diode laser as the pump. The use of photon pairs with such a high spectral bandwidth in a HOM interferometer results in a narrow-width HOM interference dip enabling sensing of static displacement as low as 60 nm and threshold vibration amplitude as low as ∼205 nm with a resolution of ∼80 nm at a frequency measurement up to 8 Hz. Further, we experimentally observed the dependence of FI on the spectral bandwidth of the pair photons and hence the length of the nonlinear crystal. We observed a 17 times enhancement in the FI value while reducing the crystal length from 30 mm to 1 mm. Such an increase in the peak FI value (35.06 ± 1.65) x 10^{-4} μm^{-2}, which is nearly 24 times higher than the previous study [178], saturates the Cramér-Rao bound to achieve any arbitrary precision (say $\sim$5 nm) in a lower number of iterations ($\sim$ 3300), $\sim$11 times lower than the previous reports. Multiplying the number of coincidence counts by the number of iterations; one can find the total number of photons used in the experiment to achieve such high precision. In our case, this provides 2×10^6 number of photon pairs to achieve the desired precision. This is somewhat higher than the 2×10^4 photons used e.g., in the experiments by Kwait et.al.[186]. However, our total measurement time is still lower thanks to the high photon flux rates, therefore allowing us to achieve overall faster sampling rates and sensitivity to higher vibration frequencies. The accessibility of high precision in lower iterations or time establishes the potential of HOM-based sensors for real-time, precision-augmented, in-field quantum sensing applications. Unlike the use of bulky and expensive ultrafast pump lasers of broad spectral bandwidth to enhance the spectral bandwidth of the down-converted photons, the generation of broadband photons using a single-frequency diode laser in small crystal length is beneficial for any practical applications.

Chapter 6

Measurement of high precision refractive index using Hong-Ou-Mandel interferometer based quantum sensor

Hong-Ou-Mandel (HOM) interferometry has emerged as a valuable tool for quantum sensing applications, particularly in measuring physical parameters that influence the relative optical delay between paired photons. Unlike classical techniques, HOM-based quantum sensors offer higher resolution due to their intrinsic dispersion cancellation property. However, achieving precise measurements of optical delay is crucial for practical applications, and integration of traditional statistical methods with HOM interferometry can be time-consuming. To address this challenge, we recently measured the optical delay with high precision while maintaining fast detection and high photon counts by suitably selecting the length of nonlinear crystal for pair photon generation. Using periodically-poled KTP (PPKTP) crystal of length 1 mm, we report on the measurement of the temperature-dependent group index of nonlinear crystal with a precision in the order of 10^{-6}. Our achieved precision of $\sim 6.75 \times 10^{-6}$ per centimeter of sample length exceeds the previously achieved maximum precision of $\sim 3 \times 10^{-5}$/cm by a remarkable margin of $>400\%$. Although the use of the HOM curve limits the measurement range, compensating the photon delay mediated by the temperature-induced changes in the group index using an optical delay stage, we can enhance the measurement range without compromising precision. For proof-of-principle, we have measured the group index variation of PPKTP over allowed temperature variation up to 200°C crystal with a precision of $\sim 10^{-6}$. The implications of this research extend to quantum optical coherence tomography, opening the avenue for high-precision and long-range measurements in this field.

6.1 Introduction

The deterministic coalescence of two indistinguishable photons on a balanced beam splitter, called Hong-Ou-Mandel interference (HOM) [100], apparently has demonstrated its substantial potential for precise optical delay measurements [178]. It enables high-precision measurements in various fields of quantum metrology such as quantum microscopy [12], quantum optical coherence tomography [121], and displacement vibration sensing [129]. The group index of a dispersive material, a metric that quantifies the velocity of a light pulse or a photon wave packet through the said material [203], can be reliably calculated using HOM interferometry. It is widely used in many areas of research, such as spectral mode shaping in optical fibers [204], quantum optical coherence tomography [118], the free spectral range of cavity resonators[205]. For the fabrication of optical fibers that support only specific modes, the size of the core is a crucial parameter, necessitating the precise determination of the group index of its core with a precision greater than 10^{-4} [203]. Earlier techniques for measuring the high-precision group index did not adequately address the requirement for enhancing the precision of HOM interferometry. To achieve the desired levels of precision, these methodologies frequently suffer from stringent prerequisites, such as the long interaction length of the specimen and subsequent post-processing of large data accumulated iteratively [17]. It not only lengthens the measurement process but, in some cases, such as the case of non-linear crystals, specimens with long interaction lengths are exceedingly fragile and difficult to grow [206]. This challenge necessitates the use of much more sophisticated methods of crystal growth, making them highly cost-intensive [207]. Therefore, it is essential to alleviate the two above-said stringent requirements in order to maximize cost and time efficiency while simultaneously enhancing measurement precision..

We address the issue of lower precision of a HOM interferometer by employing indistinguishable photons with broad spectral bandwidth generated through parametric down-conversion in periodically-poled potassium titanyl phosphate (PPKTP) crystal with short interaction length. We used a 1 mm long PPKTP crystal to generate down-converted 162 $\pm$ 1.12 nm and then employed them in the HOM interferometer to produce HOM curves with full width at half maxima (FWHM) of 4.05 $\pm$ 0.03 µm. Using these HOM curves, we measured the group indices of different sample materials by measuring the group delay introduced by them. We observed that the resolution of group index measurement increases from $\sim 8.2 \times 10^{-4}$ to $\sim 8 \times 10^{-5}$ when the spectral bandwidth of down-converted photons increases from 3.2 $\pm$ 0.01 nm to 162 $\pm$ 1.12 nm. We further used the increased slope of this narrow HOM curve and obtained a maximum achievable resolution of $\sim 2.25 \times 10^{-6}$ with a range of measurement $\sim 7.3 \times 10^{-5}$. The group index (n_g) of a dispersive can be related to the refractive index (n) of the material as follows [208];

$$\begin{aligned} n_g &= \frac{c}{v_g} \\ &= n - \lambda \frac{dn}{d\lambda}|_{\lambda=\lambda_\circ} \end{aligned} \tag{6.1}$$

Where c, v_g are the velocity of light in vacuum and group velocity of light in the sample material. Where $\lambda_\circ$ is the central wavelength of the photon wave packet traveling through the dispersive material. Eq. 6.1 equation suggests that in the regime of normal dispersion, the group index of material will always be lower than its refractive index. In HOM interference, if Δx is the optical delay introduced by the sample material having an effective interaction length of L, its group index can be written as follows;

$$n_g = \frac{\Delta x}{L} \tag{6.2}$$

From Eq. 6.2, it can be deduced that the precision of measuring the group index, n_g, of a specimen depends upon the precision of measuring the optical delay introduced by it and the precision with its length is known.

6.2 Experimental setup

The schematic of Fig. 6.1(a) shows the concept of quantum sensing using HOM interferometry. The detailed experiment scheme is the same as the experimental setup shown in Ref. [129]. A single-frequency, linearly polarized (vertical polarization), continuous-wave (CW), fiber-coupled diode laser providing 20 mW of output power at 405.4 nm is used as the pump laser in the experiment. The pump laser is focused

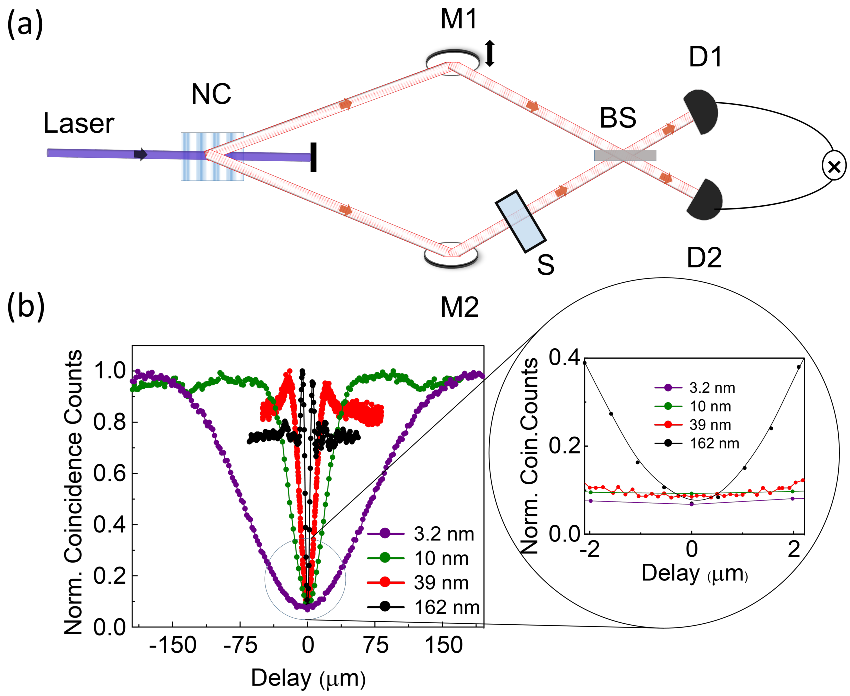

Figure 6.1: a) Schematic of the experimental setup. **NC**: PPKTP crystal of grating period = 3.425 μm, **NF**: notch filter, **S**: Specimen, **M1-2**: dielectric mirrors, **BS**: 50:50 beam splitter, **C1,2**: Fiber couplers, b) HOM curve profiles for the four cases of SPDC photons having different spectral bandwidth

at the center of the nonlinear crystal for the optimum rate of pair-photon generation. Two periodically poled $KTiOPO_4$ (PPKTP) crystals of the same aperture (1×2 mm^2) but of different interaction lengths, L = 1, and 20 are used as the nonlinear crystal

(NC) of the experiment. Both the nonlinear crystals have a single grating period of Λ = 3.425 µm designed for the degenerate, type-0 ($e \rightarrow e + e$) phase-matched parametric down-conversion (PDC) of 405 nm to 810 nm. To set out quasi-phase-matching, the PPKTP crystals are kept in an oven having dynamic temperature control over room temperature to 200°C with temperature stability of ± 0.1°C. After being separated from the pump, the non-collinear, down-converted pair photons are collimated and guided in two different paths to interfere with the balanced (50:50) beam splitter (BS).

To relative optical delay between the pair photons is adjusted using the optical delay line in the path of one of the photons. On the other hand, the sample, S, under study is placed in the path of another photon. The photons at the output ports of the BS are collected using single-mode fiber connected to the single-photon counting modules, D1 and D2 (AQRH-14-FC, Excelitas). Further, the time-to-digital converter, TDC (ID-800), is used to measure the single and coincidence counts. All optical components used in the setup are selected for optimal performance at both the pump and SPDC wavelengths. All the data is recorded at a coincidence window of 1.6 ns and a typical pump power of 0.25 mW.

6.3 Results and Discussions

We first studied the performance of the HOM interferometer for four different spectral widths of the pair photons. It is evident from Ref. [129] that the pair photons generated from PPKTP crystal of length, L = 1 mm, and 20 mm, have a spectral width of 162 $\pm$ 1.12 nm, and 39 $\pm$ 0.2 nm. To reduce the spectral width, we have filtered the pair-photons using interference filters with transmission bandwidths of 3.2 nm and 10 nm centered at 810 nm. Using the pair-photons with four different spectral bandwidths, we measured the HOM interference by recording the coincidence counts with the relative optical delay. The results are shown in Fig. 6.1(b). As expected from the previous report [129], the FWHM width of the HOM dip increases from 4.05 $\pm$ 0.01, 16.9 $\pm$ 0.03, 42.4 $\pm$ 0.06 and 144.5 $\pm$ 0.08 µm with the decrease of spectral bandwidth of the pair photons from 162 ± 1.12 nm (crystal length 1 mm), 39 ± 0.2 nm (crystal length 20 mm), 10 ± 0.01 (10 nm interference filter) and 3.2 ± 0.01 nm (3.2 nm interference filter). Interestingly, the HOM curve (purple color) for the pair-photons with a spectral bandwidth of 3.2 nm can be approximated by an inverted Gaussian profile. Such observation confirms that the pair photons carry a Gaussian temporal profile. On the other hand, we observe the oscillatory fluctuation of the coincidence counts (black dots) with diminishing amplitude away from the HOM dip in the case of broadband (spectral width of 162 nm) pair-photons due to the beating of the probability amplitudes of the two-photon wave packet [179]. To gain further perspective, we have magnified the minimum coincidence section of the HOM curves with the results shown in the inset of Fig. 6.1(b). It is interesting to note that for the optical delay in the range of ±2 μm, the minimum coincidence counts for pair-photons with spectral widths of 3.2 nm, 10 nm, and 39 nm are the same. As a result, one can encounter significant errors while determining the optical delay corresponding to the minimum coincidence counts and subsequent inaccuracies in the measurements of any physical parameter (e.g., the refractive index of a sample) while using the shift of HOM dip. On the other hand, the fast variation in coincidence counts with optical delay, as observed for the HOM curve (black dots) of pair-photons with broad spectra, results in relatively higher accuracy in identifying and measuring optical delay corresponding to the minimum coincidence. Therefore, the narrow HOM curve is preferred for high-accuracy measurements in quantum sensing applications.

Further, to establish the need for a narrow HOM curve for high-resolution HOM-based quantum sensors, we have used HOM interferometry to measure the optical delay between the pair photons introduced by a dispersive material with different group indexes. Using the measured group index and the dispersion relations, one can determine the refractive index of the material. For group index measurement, we have used five different samples (S), including the commonly used periodically poled nonlinear crystals, KTP (KTP), Mgo-doped stoichiometric grown lithium tantalate (SLT), and MgO-doped congruent grown lithium niobate (CLN) of lengths, 5.07, 5.18, and 10.03 mm, respectively and two glass slabs, named as Gls1 (Schott glass) and Gls2 (BK7) of

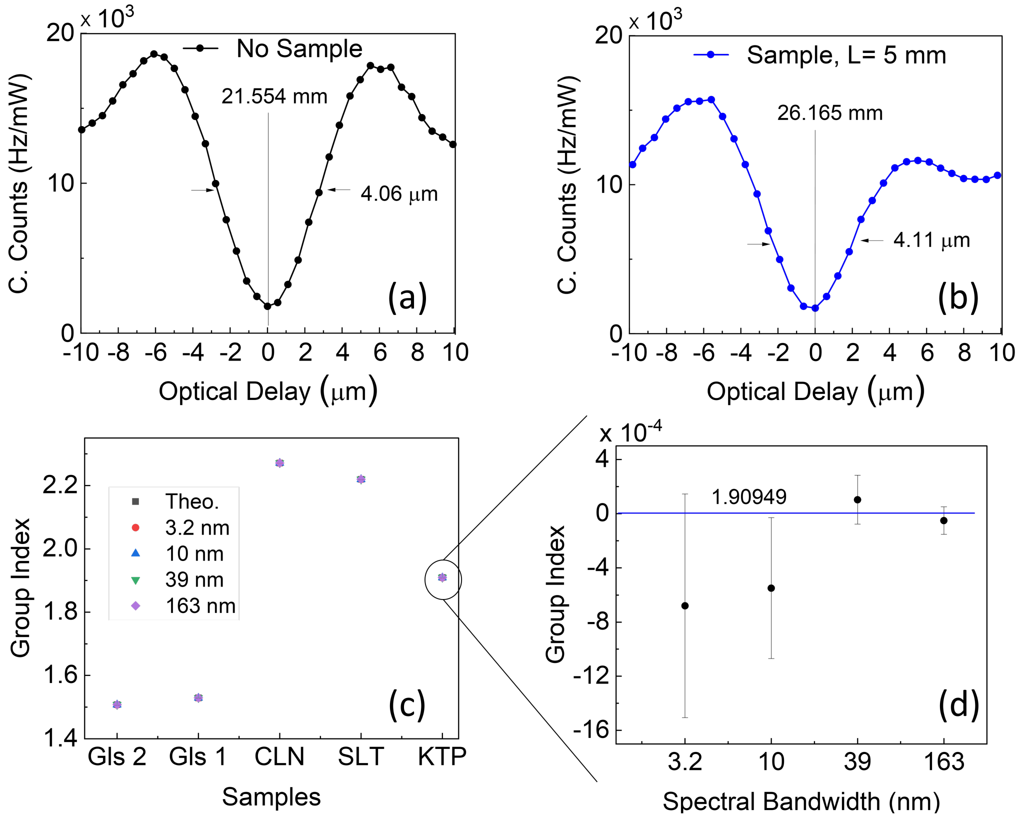

Figure 6.2: Group index measurements of PPKTP crystal with photons having different spectral bandwidth, b) Group index measurement for different sample materials with photons of different spectral bandwidth

lengths, 3.10, and 1.15 mm, respectively. As expected, the insertion of the sample (S) in one of the arms of the HOM interferometer shifts the HOM curve. We retrieved the HOM curve using the delay stage employed in the other arm of the HOM interferometer. Subsequently, using the overall shift (Δx) of the interference minima due to the presence of the samples for all four spectral widths of the pair-photons, we calculated the group index using Eq. 6.2. The results are shown in Fig. 6.2. As evident from Fig. 6.2(a), the pair photons generated by a PPKTP crystal of length 1 mm have a symmetric HOM curve in the absence of any sample with an FWHM width (obtained using Gaussian fit to the experimental data) of 4.06 ± 0.02 μm. The minimum coincidence point of the HOM curve is achieved for the linear stage reading of 21.554 mm. However, the insertion of the sample (PPKTP crystal of length, L = 5 mm) shifts the HOM curve, as shown in Fig. 6.2(b). The HOM curve has an asymmetry, but the FWHM width of 4.11 ± 0.03 μm is almost the same as the FWHM width of the HOM curve in the absence of the sample. Such observation confirms the dispersion cancellation property of the HOM interferometer [15]. The minimum coincidence point of the HOM curve in the presence of a 5 mm long PPKTP sample is obtained at a linear stage reading of 26.164 mm. The overall change in the optical delay can be written as Δx = (n_g-1)x L = 4.61 mm. Using this optical delay; we can measure the group index of the sample. We repeated the same measurement for different samples of varying lengths and the spectral width of the paired photon and measured the group index. The results are shown in Fig. 6.2(c). It is observed that the group index of all five samples measured (dots) using pair-photons of different spectral bandwidths matches the group index calculated using the respective Sellmeier equation (line). Such observation establishes the capability and reliability of the HOM interferometer as a potential refractometer to measure the group index of any dispersive materials. In this measurement, all materials were kept at room temperature. However, to observe the accuracy of the measured group index due to possible estimation errors in the measurement parameter, (Δx), while using different spectral widths of the pair-photons, we have magnified the scale of the group index data recorded for PPKTP crystal. The results are shown in Fig. 6.2(d). As evident from Fig. 6.2(d), the group index (dots) of the PPKTP crystal measured using different spectral widths of the pair-photons lies close to the theoretical value (blue line) calculated using the dispersion relations [156] of the PPKTP crystal. However, careful observation reveals that the improvement in the measurement precision from $\pm 8.3\times 10^{-4}$ to $\pm 1\times 10^{-4}$, an $8\times$ enhancement for the use of HOM interference with pair-photons of broad spectral width, 162 nm, over 3.2 nm. Such improvement can be attributed to the improved accuracy in measuring the HOM curve shift while using a narrow HOM dip due to the broad spectra of the pair-photons. However, the dispersion of the sample in the presence of different spectral widths of the pair photons showed almost no change in the resolution. This is due to the dispersion cancelation characteristics of the HOM interferometer, as evident from Fig. 6.2 and also observed in the case of two-photon interferometry-based quantum optical coherence tomography using ultra-broadband pair-photon [15].

Therefore, one can use the shift of the HOM curve as a pointer to measure the group index of any dispersive medium with an accuracy in the range of $\pm 1 \times 10^{-4}$ while using the broad spectral bandwidth of the pair-photons. Similar performances are observed for group index measurement of all the material. To better understand, we have tabulated all the group index measurement parameters in Table 6.1. The length of the samples is measured value in the lab using vernier calipers. These measured lengths exactly match the tolerance range specified by the supplier of the samples. The spectral width of the pair-photons used in this measurement is 162 nm. As evident from Table 6.1, the measurement accuracy of the group index of all the dispersive mediums with different lengths is expectedly in the range of $\pm 1 \times 10^{-4}$, similar to the order of precision achieved by optical coherence tomography (OCT) [209, 210]. However, we can not use this technique to measure the temperature-dependent group index (thermo-optic dispersion) variation of different nonlinear crystals useful for quasi-phase-matched nonlinear parametric processes due to their weak temperature dependence (in the range of 10^{-4} - 10^{-5}/°C. Therefore, we need the precision at least one order of magnitude lower, i.e., $\sim 10^{-6}$. On the other hand, we have demonstrated the measurement of static optical delay of 60 nm using HOM interferometry with pair photons of broad spectral width [129]. As the optical delay is defined as the product refractive index, n, and physical length, L, of a medium, i.e., n x L, one can easily measure the change in the refractive index smaller than $\sim 10^{-6}$ by suitably selecting the physical length of the medium.

Table 6.1: Group index (n_g) of different materials at room temperature.

Sample	Length (mm)	Theory n_g	Measured n_g	Accuracy	Sellmeier equation
PPKTP crystal	5.07	1.90949	1.90944	1.02×10^{-4}	[156]
PPSLT crystal	5.18	2.21997	2.21994	8.97×10^{-5}	[211]
MCLN crystal	10.03	2.27129	2.27132	8.04×10^{-5}	[211]
Schott Glass (Gls1)	1.15	1.52927	1.52924	1.05×10^{-4}	[212]
Glass slab (Gls2)	3.10	1.50778	1.50773	8.97×10^{-5}	[213]

To verify the possibility of measuring the temperature-dependent group index (thermo-optic dispersion) of periodically poled crystal, we have selected PPKTP crystal. Two advantages justify such selection; firstly, the experimental observations can be validated using standard data from available Sellmeier equations [156], and secondly, the PPKTP crystal exhibits $\sim$ 15 times less susceptibility to temperature fluctuations as compared to the other popular periodically poled crystals such as PPSLT and MCLN [211, 214].

However, before the experimental observations, we analytically calculated the variations in the group index of PPKTP crystal as a function of crystal temperature. Let us assume that $x(T_\circ)$ is the optical delay between the pair photons due to the PPKTP crystal of length L and group index n_g at initial temperature $T_\circ$. The $x(T_\circ)$ can be written as,

$$x(T_\circ) = n_g(T_\circ) \times L(T_\circ) \tag{6.3}$$

Now the change in crystal temperature by ΔT leads to the change in its group index and effective interaction length due to thermo-optic dispersion and thermal expansion, respectively. Therefore, the temperature-dependent the optical delay, $x(T_\circ + \Delta T)$, can be written as,

$$x(T_\circ + \Delta T) = (n_g(T_\circ) + \Delta n_g(\Delta T)) \times (L(T_\circ) + \Delta L(\Delta T)) \tag{6.4}$$

where $\Delta n_g(\Delta T)$ and $\Delta L(\Delta T)$ denote the change in group index and the effective interaction length of the crystal, respectively, due to the change in crystal temperature of ΔT. The net change in the relative optical delay corresponding to the change in crystal temperature can be written as,

$$\Delta x(\Delta T) = x(T_\circ + \Delta T) - x(T_\circ) \tag{6.5}$$

Using Eq. 6.3 and Eq. 6.4 in Eq. 6.5 and neglecting the term $\Delta n_g(\Delta T)\Delta L(\Delta T)$ due to its small (10^{-10}) magnitude as compared to the measurement accuracy, we can represent the temperature-dependent group index change as,

$$\Delta n_g(\Delta T) \simeq \frac{\Delta x(\Delta T) - n_g \Delta L(\Delta T)}{L} \tag{6.6}$$

The second term in the numerator of Eq. 6.6 accounts for the change in relative optical delay between the signal and idler of the paired photons due to the thermal expansion of the PPKTP crystal placed in one of the arms of the HOM interferometer. Since the refractive index and crystal lengths vary simultaneously with the temperature, we can measure one of the parameters at a time for a given value of the other parameter. Therefore, we used the available thermal expansion data of PPKTP crystal from the literature using Ref. [215] and measured the temperature-dependent group index variation of the PPKTP crystal.

As evident from Eq. 6.6, for a given crystal length, L, by measuring the change in optical delay, $\Delta x(\Delta T)$, one can easily find the temperature-dependent group index of the crystal. In doing so, we have reconstructed the HOM curve in the presence of the sample (PPKTP crystal of measured length, L = 30.12 mm) in one of the arms of the HOM interferometer. In this case, the temperature of the sample is kept fixed (26°C). As the presence of the sample does not change the width of the HOM curve due to its intrinsic dispersion cancellation property as observed in Fig. 6.2 and Ref. [15], we obtained the HOM curve of FWHM width same as the HOM curve presented in Fig. 6.2(b)).

Further, we adjusted the delay line such that the initial point corresponding to the crystal temperature, T_o = 26°C, results in an optical delay of +1 μm (see Fig. 6.2(b)). Such selection is purposefully made to access the majority of the linear range of the HOM curve, thus enhancing the measurement range. Now we change the temperature of the sample (PPKTP crystal) in a step of 0.1°C allowed by the oven. Since such small increments are close to the stability range of the oven, for each temperature rise, we allowed the oven and crystal sufficient time ($\sim$ 2 minutes) to settle the temperature rise and finally recorded the coincidence counts data for a total of 200 iterations to enhance the precision of measurement. Using these coincidence counts and comparing them with the HOM curve (see Fig. 6.2(b)), we estimate the optical delay as a function of the crystal temperature. The results are shown in Fig. 6.3. As evident from Fig. 6.3(a), the optical delay due to the change in the group index of the sample (PPKTP crystal) increases linearly with the crystal temperature in the range of 26 - 29°C with a

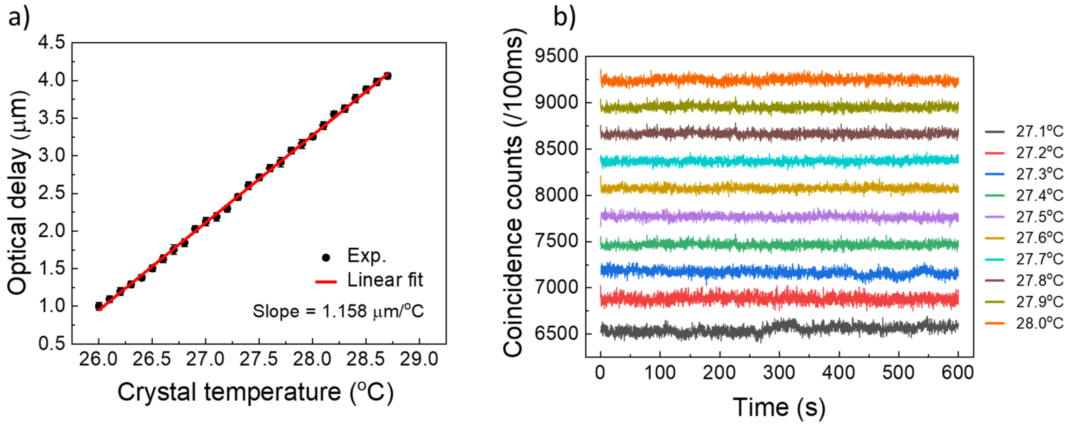

Figure 6.3: Variation in the coincidence counts of HOM interferometer with the relative optical delay between signal and idler introduced through the movement of mirror M2 (black dots), and through the temperature change of the crystal (red dots), b) Temporal stability of the coincidence counts for a period of 10 minutes at each increment in the crystal temperature

slop of 1.158 μm/°C of the crystal temperature. Further increase in crystal temperature pushes the optical delay out of the linearity range and provides arbitrary results. However, by adjusting the initial point, we can measure the group index of the nonlinear crystal over a range of 3°C. To confirm the reliability of the experiment, we recorded the variation of coincidence counts over 10 minutes for each step change (0.1°C) of the crystal temperature across 27.1 - 28°C. The results are shown in Fig. 6.3(b). It is evident from Fig. 6.3(b) that the change of crystal temperature by 0.1°C results in a change of the coincidence counts of more than 100 per 100 ms of integration time. Such a large change in the coincidence count, much higher than the dark count and accidental counts, confirms the possibility of measurement of the change of group index of nonlinear crystal with temperature change smaller than 0.1°C. We could not access the lower step of the temperature change due to the unavailability of a suitable oven in our lab. As observed previously [129], the temporal variation of the coincidence counts is due to various parameters, including the laser intensity fluctuation, air current, and local temperature instability in the laboratory. However, such change in coincidence counts resulting from different external perturbations is much smaller than the change in the coincidence counts due to the change in the group index of the sample (nonlinear crystal). Using the optical delay corresponding to change in crystal (length, L =

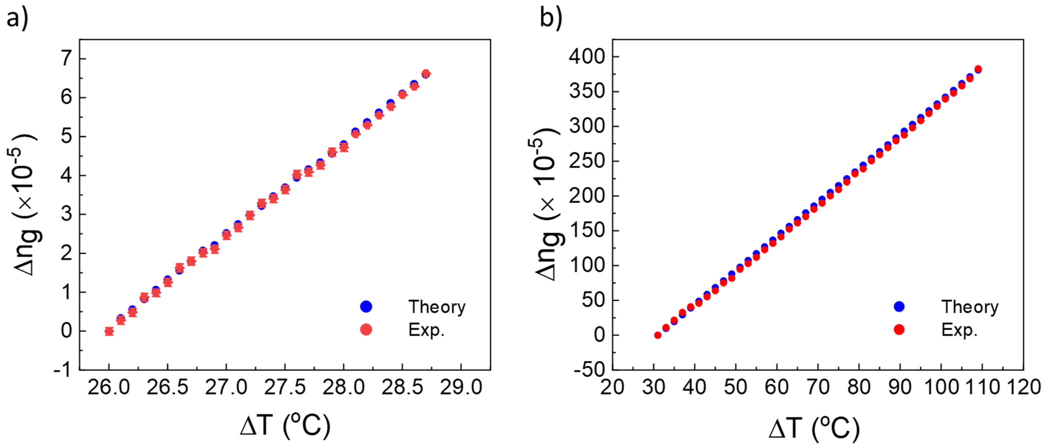

Figure 6.4: a),b) variation in the group index of PPKTP crystal with the change in its temperature measured using indistinguishable photons of spectral bandwidth 162, 39, 10, and 3.2 nm, respectively.

30.12 mm) temperature from Fig. 6.3(a), the group index value from Table 6.1 and the thermal expansion of the crystal, $\Delta L(\Delta T)$ from [215] in Eq. 6.6, we calculated the temperature-dependent group index, $\Delta n_g(\Delta$ T), of the PPKTP crystal. The results are shown in Fig. 6.4. As evident from Fig. 6.4(a), the temperature-dependent group index (red dots) measured using the HOM curve of FWHM width around 4.11 µm has a temperature range of 3°C at any initial point and the corresponding range group index variation of $\sim$7.3 $\times$ 10^{-5}. The measurement of group index for the minimum change of crystal temperature, 0.1°C, sets the resolution of the HOM-based quantum sensor to be $\sim 2.25 \times 10^{-6}$ for sample length of 30.12 mm. Using the dispersion relations of the PPKTP crystal from Ref. [156, 215], we calculated the temperature-dependent group index variation (blue dots) in close agreement with the experimental results (red dots). As compared to previous report on high precision group index measurements [17] of a sample (optical fiber) length of 50 cm having precision of 3 $\times 10^{-5}$/cm (absolute value of 6 $\times 10^{-7}$ for 50 cm sample) our measurement precision, 6.75 $\times 10^{-6}$/cm, show an unprecedented enhancement by $\sim$ 444%. Such enhancement was possible due to the narrow HOM-curve resulting from the control in the length of the nonlinear crystal producing broadband paired photons [129]. To measure the group index variation over a wider temperature range, we have repeated the measurement using the HOM curve with an FWHM width of 144.5 $\pm$ 0.08 µm with the results shown in Fig. 6.4(b). As expected, the experimental results (red dots) are closely matching with theoretical results (blue). It is also evident that the range of temperature and corresponding group index has increased to 80°C and $\sim 386.1 \times 10^{-5}$ but with lower resolution ($\sim 4.5 \times 10^{-5}$). To avoid the range-dependent resolution and enhance the range while keeping the high resolution ($\sim 2.25 \times 10^{-6}$), we have used the technique reported in Ref. [129] to calibrate the open loop piezo system. In this technique, we have used the HOM-curve of FWHM dip width of 4.11 µm and adjusted the optical delay corresponding to the initial crystal temperature at the middle of the linearity region of the HOM curve. Knowing the coincidence counts for the initial point; we have adjusted the optical delay stage to compensate for the temperature-dependent group, index-mediated coincidence counts. Since the entire HOM curve is not being used for this experiment, we can access the unlimited range with the finest accuracy determined by the narrow HOM curve. In the current experiment, we have measured the group index variation of the PPKTP crystal from room temperature to the allowed maximum temperature of 200°C with the precision of $\sim 2.25 \times 10^{-6}$.

6.4 Conclusion

In conclusion, we have successfully demonstrated a HOM interferometer-based quantum sensor for the measurement of group index variation of nonlinear crystals with high precision. Using the HOM curve of FWHM width of 4.11 µm resulting from the paired photons generated by a PPKTP crystal of length 1 mm, we have measured the temperature-dependent group index of PPKTP crystal over a temperature range of 3°C at any arbitrary initial temperature with a resolution of 6.75 $\times 10^{-6}$ per centimeter length of the sample. This resolution is >400% better than the previous group index measurement [17]. Such enhancement was possible due to the control of the spectral of the paired photon; thus, the width of the HOM curve using the optimized length of the nonlinear crystal produced paired photons with a high generation rate. Using compensation of group index mediated optical delay by the linear optical delay stage, we observed the possibility of measuring group index with high precision over an unlimited temperate range. The current demonstration opens up the possibility of HOM-based quantum sensors for quantum optical coherence tomography with high resolution and measurement range.

Chapter 7

Conclusions and Future Plans

7.1 Conclusions

This thesis is primarily focused on the study of the generation and characterization of pair photon sources based on spontaneous parametric down-conversion in non-linear crystals and their applications in quantum sensing applications. We addressed three key challenges of quantum sensing, such as low pair photon rate, low stability of the pair photon source, and lower measurement resolution.

In Chapter 3, we have investigated the effect of the phase-matching parameters, such as the pump beam waist (ω_p), collection beam waist (ω_c), and crystal temperature on the coincidence count collection, and the pair coupling efficiency to single mode fibers. A maximum coincidence count of 1692.3 $\pm$ 8.5 KHz/mW for ω_p = 42 µm and ω_c = 57 µm has been achieved at a crystal temperature of 29.5°C, while a maximum coupling efficiency of 32.1 $\pm$ 0.6 % is observed for ω_p = 84 µm and ω_c = 109 µm at a crystal temperature of 26°C. It is observed that both the pump intensity at the crystal center and the divergence of the SPDC photons play a crucial role in the collection of pair photons into single-mode fibers, while the pair coupling efficiency (η_c) is majorly controlled by the divergence of the pump and, thus, the divergence of SPDC photons. The rate of generation of photons does not seem to alter the pair coupling efficiency. This conclusion supports the experimental observation that for a fixed collection beam waist ω_c, the pump beam waist (ω_p) providing the maximum pair coupling efficiency is different from the ω_p providing maximum coincidence counts.

In Chapter 4, we have demonstrated a novel configuration for a spontaneous parametric down-conversion process to enhance the tolerance of generated pair photons against the perturbations in the phase-matching parameters such as pump wavelength, crystal temperature, and the tilt of the crystal w.r.t to the propagation direction of the pump beam. This new configuration involves a hybrid solution that incorporates a lens-axicon pair, commonly available in an optics laboratory, to transform the conventional SPDC annular ring into a new ring. This new SPDC ring enhances the tolerance of the SPDC ring to external perturbations in phase-matching parameters without sacrificing the spectral brightness of the source. The spectral brightness of the source is observed to be as high as 22.58$\pm$0.15 kHz/mW with a state fidelity of 0.95$\pm$0.02, yet requiring a crystal temperature stability of only $\pm$0.8°C, a 5$\times$ enhanced tolerance as compared to the conventional high brightness SPDC configurations. It also relaxes crystal tilt stability by more than 3$\times$ and the wavelength stability of the pump laser by more than 100 GHz. This new configuration for the generation of pair photons through SPDC is highly useful in quantum sensing experiments of QOCT, and the experiments required field deployment of pair photon source.

In Chapter 5, we characterized the Hong-Ou-Mandel interferometer for high-precision sensing of small changes in the optical delay between the indistinguishable photons. We experimentally demonstrated an easy control of the spectral bandwidth of the pair photons through proper selection of the length of the non-linear crystal used for the generation of pair photons. Using a 1 mm long PPKTP crystal, we have generated paired photons with spectral width as high as 163.42 $\pm$ 1.68 nm even in the presence of a single-frequency, CW, diode laser as the pump. The use of photon pairs with such a high spectral bandwidth in a HOM interferometer results in a narrow-width HOM interference dip having an FWHM of 4.01$\pm$0.04 μm enabling the real-time sensing of static displacement as low as 60 nm and threshold vibration amplitude as low as $\sim$205 nm with a resolution of $\sim$80 nm at a frequency measurement up to 8 Hz. Further, we experimentally observed the dependence of FI on the spectral bandwidth of the pair photons and hence the length of the nonlinear crystal. We observed a 17 times enhancement in the FI value while reducing the crystal length from 30 mm to 1 mm. Such an increase in the peak FI value (35.06 $\pm$ 1.65) x 10^{-4} μm^{-2}, which is nearly 24 times higher than the previous study, saturates the Cramér-Rao bound to achieve any arbitrary precision (say $\sim$5 nm) in a lower number of iterations ($\sim$ 3300), $\sim$11 times lower than the previous reports. The accessibility of high precision in lower iterations or time establishes the potential of HOM-based sensors for real-time, precision-augmented, in-field quantum sensing applications.

In Chapter 6, we successfully demonstrated the application of HOM interferometer-based quantum sensors for the measurement of group index variation of nonlinear crystals with high precision. Using the HOM curve of FWHM width of 4.11 μm resulting from the paired photons generated by a PPKTP crystal of length 1 mm, we have measured the temperature-dependent group index of PPKTP crystal over a temperature range of 3°C at any arbitrary initial temperature with a resolution of 6.75 $\times 10^{-6}$ per centimeter length of the sample. This resolution is >400% better than the previous group index measurement [17]. Such enhancement was possible due to the control of the spectral of the paired photon; thus, the width of the HOM curve using the optimized length of the nonlinear crystal produced paired photons with a high generation rate. Using compensation of group index mediated optical delay by the linear optical delay stage, we observed the possibility of measuring group index with high precision over an unlimited temperate range. The current demonstration opens up the possibility of HOM-based quantum sensors for quantum optical coherence tomography with high resolution and measurement range.

7.2 Future Plans

In the work presented here so far, we have explored HOM-based quantum sensing utilizing the time of arrival of pair photons on the beam splitter. However, as a prospect for future research, we intend to broaden the scope of HOM-based quantum sensing to include the polarization degree of freedom. The indistinguishable photons bunching on the beam splitter have the same polarization states. However, even a small change in the polarization state of any individual photon from the pair will render them again distinguishability, but now in their polarization degree of freedom. This further leads to an equivalent change in the coincidence counts, which can be used as a pointer to sense those small alterations in the polarization direction of the pair photons. Such kind of changes in the polarization direction of photons can be induced by propagating them through optically active materials, where circular birefringence of the optically active material rotates the polarization direction of light. This change in the polarization direction is a characteristic parameter of the material and intrinsically a measure of its optical activity. One such optical active material is a sample of sugar solution with a known concentration and interaction length. The previous approaches for optical activity measurements are based on classical light interferometry and have lower sensitivity for the optical activity, which necessitates either a high concentration of the optically active material or longer interaction lengths of the sample. We would like to extend the application of the high sensitivity of HOM-based quantum sensing for measuring the optical activity of an optically active material even with a low concentration of the sample or having shorter interaction sample lengths.

We would also like to explore quantum imaging in conjunction with HOM-based quantum sensing. It is a technique where a high-resolution 3-D surface profile of a sample material is constructed using shifts in relative optical delays of pair photons carrying the information about the surface depth profile of the sample. In contrast to classical imagining techniques, quantum imaging is benefitted from additional advantages such as robust sensing even with low light. The previous techniques for HOM-based quantum imaging are able to attain a surface depth profile with a maximum average resolution limit of $\sim$ 8 µm. This limit is decided by the sensitivity of the HOM-based sensor involved in the imaging process. However, we have developed a high-precision HOM-based sensor with the potential to measure the static displacement at a resolution of $\sim$ 60 nm. The application of our approach for HOM-based quantum sensing can greatly overcome the earlier attained resolution limits, which give rise to HOM-based quantum imaging with sub-micron resolution.

Bibliography

[1] BN Dwivedi. “James Clerk Maxwell and his equations”. In: *Resonance* 8.5 (2003), pp. 4–16.

[2] Arnold B Arons and MB Peppard. “Einstein’s Proposal of the Photon Concept—a Translation of the Annalen der Physik Paper of 1905”. In: *American Journal of Physics* 33.5 (1965), pp. 367–374.

[3] Gilbert N Lewis. “The conservation of photons”. In: *Nature* 118.2981 (1926), pp. 874–875.

[4] Paul Adrien Maurice Dirac. “The quantum theory of the emission and absorption of radiation”. In: *Proceedings of the Royal Society of London. Series A, Containing Papers of a Mathematical and Physical Character* 114.767 (1927), pp. 243–265.

[5] Albert Einstein, Boris Podolsky, and Nathan Rosen. “Can quantum-mechanical description of physical reality be considered complete?” In: *Physical review* 47.10 (1935), p. 777.

[6] John S Bell. “On the einstein podolsky rosen paradox”. In: *Physics Physique Fizika* 1.3 (1964), p. 195.

[7] John F Clauser et al. “Proposed experiment to test local hidden-variable theories”. In: *Physical review letters* 23.15 (1969), p. 880.

[8] Stuart J Freedman and John F Clauser. “Experimental test of local hidden-variable theories”. In: *Physical Review Letters* 28.14 (1972), p. 938.

[9] Alain Aspect, Jean Dalibard, and Gérard Roger. "Experimental test of Bell's inequalities using time-varying analyzers". In: *Physical review letters* 49.25 (1982), p. 1804.

[10] Dik Bouwmeester et al. "Experimental quantum teleportation". In: *Nature* 390.6660 (1997), pp. 575–579.

[11] MV Jabir and GK Samanta. "Robust, high brightness, degenerate entangled photon source at room temperature". In: *Scientific reports* 7.1 (2017), p. 12613.

[12] Bienvenu Ndagano et al. "Quantum microscopy based on Hong–Ou–Mandel interference". In: *Nature Photonics* 16.5 (2022), pp. 384–389.

[13] Urbasi Sinha et al. "Ruling out multi-order interference in quantum mechanics". In: *Science* 329.5990 (2010), pp. 418–421.

[14] Nicolas Gisin et al. "Quantum cryptography". In: *Reviews of modern physics* 74.1 (2002), p. 145.

[15] Masayuki Okano et al. "0.54 μm resolution two-photon interference with dispersion cancellation for quantum optical coherence tomography". In: *Scientific reports* 5.1 (2015), p. 18042.

[16] Ganwei Yan et al. "Metrological performance analysis of optical coherent tomography". In: *Measurement* 189 (2022), p. 110437.

[17] Mattis Reisner et al. "Quantum-limited determination of refractive index difference by means of entanglement". In: *npj Quantum Information* 8.1 (2022), p. 58.

[18] C Cohen-Tannoudji, J Dupont-Roc, and G Grynberg. "Photons and Atoms-Introduction to Quantum Electrodynamics Wiley-VCH". In: *February* 486 (1997), p. 1997.

[19] Marlan O Scully and M Suhail Zubairy. *Quantum optics*. 1999.

[20] Matthew D Eisaman et al. "Invited review article: Single-photon sources and detectors". In: *Review of scientific instruments* 82.7 (2011), p. 071101.

[21] Anthony Mark Fox and Mark Fox. *Quantum optics: an introduction*. Vol. 15. Oxford university press, 2006.

[22] Andrew Forbes. *Progress in quantum networks*. 2022.

[23] H. J. Kimble. "The quantum internet". In: *Nature* 453.7198 (2008), pp. 1023–1030.

[24] S Wehner, D Elkouss, and R Hanson. "Science 362, eaam9288 (2018)". In: *The author declares no competing interests* (2008).

[25] Bernd Fröhlich et al. "A quantum access network". In: *Nature* 501.7465 (2013), pp. 69–72.

[26] Stefano Pirandola et al. "Advances in quantum cryptography". In: *Advances in optics and photonics* 12.4 (2020), pp. 1012–1236.

[27] John G Rarity, PCM Owens, and PR Tapster. "Quantum random number generation and key sharing". In: *Journal of Modern Optics* 41.12 (1994), pp. 2435–2444.

[28] Stefano Pirandola et al. "Advances in photonic quantum sensing". In: *Nature Photonics* 12.12 (2018), pp. 724–733.

[29] Ulrike Lieberwirth et al. "Multiplex dye DNA sequencing in capillary gel electrophoresis by diode laser-based time-resolved fluorescence detection". In: *Analytical chemistry* 70.22 (1998), pp. 4771–4779.

[30] Jens-Peter Knemeyer, Nicole Marmé, and Markus Sauer. "Probes for detection of specific DNA sequences at the single-molecule level". In: *Analytical chemistry* 72.16 (2000), pp. 3717–3724.

[31] Dmitri N Gavrilov et al. "Dynamic range of fluorescence detection and base-calling accuracy in DNA sequencer based on single-photon counting". In: *Electrophoresis* 24.7-8 (2003), pp. 1184–1192.

[32] Ivan Rech et al. "Microelectronic photosensors for genetic diagnostic microsystems". In: *Sensors and Actuators B: Chemical* 100.1-2 (2004), pp. 158–162.

[33] Takashi Isoshima et al. “Ultrahigh sensitivity single-photon detector using a Si avalanche photodiode for the measurement of ultraweak biochemiluminescence”. In: *Review of scientific instruments* 66.4 (1995), pp. 2922–2926.

[34] TJ McIlrath et al. “Two-photon lidar technique for remote sensing of atomic oxygen”. In: *Applied optics* 18.3 (1979), pp. 316–319.

[35] Maurizio Viterbini, Alberto Adriani, and Guido Di Donfrancesco. “Single photon detection and timing system for a lidar experiment”. In: *Review of scientific instruments* 58.10 (1987), pp. 1833–1839.

[36] James C Tsang, Jeffrey A Kash, and David P Vallett. “Picosecond imaging circuit analysis”. In: *IBM Journal of Research and Development* 44.4 (2000), pp. 583–603.

[37] Franco Stellari et al. “High-speed CMOS circuit testing by 50 ps time-resolved luminescence measurements”. In: *IEEE Transactions on Electron Devices* 48.12 (2001), pp. 2830–2835.

[38] SD Personick. “Photon probe—An optical-fiber time-domain reflectometer”. In: *The bell system technical journal* 56.3 (1977), pp. 355–366.

[39] BF Levine, CG Bethea, and JC Campbell. “Room-temperature 1.3-μm optical time domain reflectometer using a photon counting InGaAs/InP avalanche detector”. In: *Applied physics letters* 46.4 (1985), pp. 333–335.

[40] Steven A Soper, Quincy L Mattingly, and Pradeep Vegunta. “Photon burst detection of single near-infrared fluorescent molecules”. In: *Analytical Chemistry* 65.6 (1993), pp. 740–747.

[41] Li-Qiang Li and Lloyd M Davis. “Single photon avalanche diode for single molecule detection”. In: *Review of Scientific Instruments* 64.6 (1993), pp. 1524–1529.

[42] Antonio Pifferi et al. “Time-resolved diffuse reflectance using small source-detector separation and fast single-photon gating”. In: *Physical review letters* 100.13 (2008), p. 138101.

[43] Brahim Lounis and Michel Orrit. "Single-photon sources". In: *Reports on Progress in Physics* 68.5 (2005), p. 1129.

[44] Satoshi Kako et al. "A gallium nitride single-photon source operating at 200 K". In: *Nature materials* 5.11 (2006), pp. 887–892.

[45] Stefan Strauf et al. "High-frequency single-photon source with polarization control". In: *Nature photonics* 1.12 (2007), pp. 704–708.

[46] Andrew J Shields. "Semiconductor quantum light sources". In: *Nature photonics* 1.4 (2007), pp. 215–223.

[47] T Gaebel et al. "Stable single-photon source in the near infrared". In: *New Journal of Physics* 6.1 (2004), p. 98.

[48] Romain Alléaume et al. "Experimental open-air quantum key distribution with a single-photon source". In: *New Journal of physics* 6.1 (2004), p. 92.

[49] Christian Maurer et al. "A single-photon source based on a single Ca+ ion". In: *New journal of physics* 6.1 (2004), p. 94.

[50] Charles Santori et al. "Single-photon generation with InAs quantum dots". In: *New Journal of Physics* 6.1 (2004), p. 89.

[51] Ravitej Uppu et al. "On-chip deterministic operation of quantum dots in dual-mode waveguides for a plug-and-play single-photon source". In: *Nature communications* 11.1 (2020), p. 3782.

[52] Alfred B U'Ren et al. "Efficient conditional preparation of high-fidelity single photon states for fiber-optic quantum networks". In: *Physical review letters* 93.9 (2004), p. 093601.

[53] Edo Waks, Eleni Diamanti, and Yoshihisa Yamamoto. "Generation of photon number states". In: *New Journal of Physics* 8.1 (2006), p. 4.

[54] Alexandre Soujaeff et al. "Quantum key distribution at 1550 nm using a pulse heralded single photon source". In: *Optics express* 15.2 (2007), pp. 726–734.

[55] Jingyun Fan and Alan Migdall. "A broadband high spectral brightness fiber-based two-photon source". In: *Optics express* 15.6 (2007), pp. 2915–2920.

[56] Elizabeth A Goldschmidt et al. "Spectrally bright and broad fiber-based heralded single-photon source". In: *Physical Review A* 78.1 (2008), p. 013844.

[57] Artur K Ekert. "Quantum cryptography based on Bell's theorem". In: *Physical review letters* 67.6 (1991), p. 661.

[58] Charles H Bennett. "Quantum cryptography using any two nonorthogonal states". In: *Physical review letters* 68.21 (1992), p. 3121.

[59] Vimlesh Kumar et al. "Imaging inspired characterization of single photons carrying orbital angular momentum". In: *AVS Quantum Science* 4.1 (2022), p. 015001.

[60] Sandeep Singh et al. "A Tolerance-Enhanced Spontaneous Parametric Downconversion Source of Bright Entangled Photons". In: *Advanced Quantum Technologies* 6.2 (2022), p. 2200121.

[61] Lucia Caspani et al. "Integrated sources of photon quantum states based on nonlinear optics". In: *Light: Science & Applications* 6.11 (2017), e17100–e17100.

[62] Robert W Boyd. *Nonlinear optics*. Academic press, 2020.

[63] CK Law and JH Eberly. "Analysis and interpretation of high transverse entanglement in optical parametric down conversion". In: *Physical review letters* 92.12 (2004), p. 127903.

[64] SP Walborn and CH Monken. "Transverse spatial entanglement in parametric down-conversion". In: *Physical Review A* 76.6 (2007), p. 062305.

[65] JG Rarity and PR Tapster. "Experimental violation of Bell's inequality based on phase and momentum". In: *Physical Review Letters* 64.21 (1990), p. 2495.

[66] Alois Mair et al. "Entanglement of the orbital angular momentum states of photons". In: *Nature* 412.6844 (2001), pp. 313–316.

[67] Paul G Kwiat et al. "Proposal for a loophole-free Bell inequality experiment". In: *Physical Review A* 49.5 (1994), p. 3209.

[68] Irfan Ali Khan and John C Howell. “Experimental demonstration of high two-photon time-energy entanglement”. In: *Physical Review A* 73.3 (2006), p. 031801.

[69] WH Louisell, A Yariv, and AE Siegman. “Quantum fluctuations and noise in parametric processes. I.” In: *Physical Review* 124.6 (1961), p. 1646.

[70] DN Klyshko and BY Zeldovich. “Field statistics in parametric luminescence”. In: *JETP Lett* 9.1 (1969), pp. 40–43.

[71] David C Burnham and Donald L Weinberg. “Observation of simultaneity in parametric production of optical photon pairs”. In: *Physical Review Letters* 25.2 (1970), p. 84.

[72] JY Cheung et al. “The quantum candela: a re-definition of the standard units for optical radiation”. In: *Journal of Modern Optics* 54.2-3 (2007), pp. 373–396.

[73] Jeremy L O’brien. “Optical quantum computing”. In: *Science* 318.5856 (2007), pp. 1567–1570.

[74] Morgan W Mitchell, Jeff S Lundeen, and Aephraem M Steinberg. “Super-resolving phase measurements with a multiphoton entangled state”. In: *Nature* 429.6988 (2004), pp. 161–164.

[75] Nijil Lal, Sarika Mishra, and RP Singh. “Indistinguishable photons”. In: *AVS Quantum Science* 4.2 (2022), p. 021701.

[76] Nicolaas Bloembergen. “Conservation laws in nonlinear optics”. In: *JOSA* 70.12 (1980), pp. 1429–1436.

[77] Grant R Fowles. *Introduction to modern optics*. Courier Corporation, 1989.

[78] ZY Ou, LJ Wang, and L Mandel. “Vacuum effects on interference in two-photon down conversion”. In: *Physical Review A* 40.3 (1989), p. 1428.

[79] DA Kleinman. “Theory of optical parametric noise”. In: *Physical Review* 174.3 (1968), p. 1027.

[80] L Mandel. “Complex representation of optical fields in coherence theory”. In: *JOSA* 57.5 (1967), pp. 613–617.

[81] Suman Karan et al. "Phase matching in β-barium borate crystals for spontaneous parametric down-conversion". In: *Journal of Optics* 22.8 (2020), p. 083501.

[82] Jong-Chan Lee and Yoon-Ho Kim. "Spatial and spectral properties of entangled photons from spontaneous parametric down-conversion with a focused pump". In: *Optics Communications* 366 (2016), pp. 442–450.

[83] Morton H Rubin. "Transverse correlation in optical spontaneous parametric down-conversion". In: *Physical Review A* 54.6 (1996), p. 5349.

[84] Todd B Pittman et al. "Optical imaging by means of two-photon quantum entanglement". In: *Physical Review A* 52.5 (1995), R3429.

[85] Stephen P Walborn et al. "Spatial correlations in parametric down-conversion". In: *Physics Reports* 495.4-5 (2010), pp. 87–139.

[86] Silvia Carrasco et al. "Spatial-to-spectral mapping in spontaneous parametric down-conversion". In: *Physical Review A* 70.4 (2004), p. 043817.

[87] Martin M Fejer et al. "Quasi-phase-matched second harmonic generation: tuning and tolerances". In: *IEEE Journal of quantum electronics* 28.11 (1992), pp. 2631–2654.

[88] Radhika Rangarajan, Michael Goggin, and Paul Kwiat. "Optimizing type-I polarization-entangled photons". In: *Optics express* 17.21 (2009), pp. 18920–18933.

[89] JA Armstrong et al. "Interactions between light waves in a nonlinear dielectric". In: *Physical review* 127.6 (1962), p. 1918.

[90] Paulina S Kuo, Varun B Verma, and Sae Woo Nam. "Demonstration of a polarization-entangled photon-pair source based on phase-modulated PPLN". In: *OSA continuum* 3.2 (2020), pp. 295–304.

[91] A Aadhi and GK Samanta. "High power, high repetition rate, tunable broadband mid-IR source based on single-pass optical parametric generation of a femtosecond laser". In: *Optics Letters* 42.15 (2017), pp. 2886–2889.

[92] John G Rarity and PR Tapster. "Fourth-order interference in parametric down-conversion". In: *JOSA B* 6.6 (1989), pp. 1221–1226.

[93] Sang Min Lee et al. "Polarization-entangled photon-pair source obtained via type-II non-collinear SPDC process with PPKTP crystal". In: *Optics express* 24.3 (2016), pp. 2941–2953.

[94] Piya Techateerawat. "A review on quantum cryptography technology". In: *International Transaction Journal of Engineering, Management & Applied Sciences & Technologies* 1 (2010), pp. 35–41.

[95] DGBJ Dieks. "Communication by EPR devices". In: *Physics Letters A* 92.6 (1982), pp. 271–272.

[96] William K Wootters and Wojciech H Zurek. "A single quantum cannot be cloned". In: *Nature* 299 (1982), pp. 802–803.

[97] Mikhail I Kolobov. "The spatial behavior of nonclassical light". In: *Reviews of Modern Physics* 71.5 (1999), p. 1539.

[98] Irfan Ali-Khan, Curtis J Broadbent, and John C Howell. "Large-alphabet quantum key distribution using energy-time entangled bipartite states". In: *Physical review letters* 98.6 (2007), p. 060503.

[99] Jacob Mower et al. "High-dimensional quantum key distribution using dispersive optics". In: *Physical Review A* 87.6 (2013), p. 062322.

[100] Chong-Ki Hong, Zhe-Yu Ou, and Leonard Mandel. "Measurement of subpicosecond time intervals between two photons by interference". In: *Physical review letters* 59.18 (1987), p. 2044.

[101] Sudhakar Prasad, Marlan O Scully, and Werner Martienssen. "A quantum description of the beam splitter". In: *Optics communications* 62.3 (1987), pp. 139–145.

[102] ZY Ou, CK Hong, and L Mandel. "Relation between input and output states for a beam splitter". In: *Optics communications* 63.2 (1987), pp. 118–122.

[103] H Fearn and R Loudon. "Quantum theory of the lossless beam splitter". In: *Optics communications* 64.6 (1987), pp. 485–490.

[104] JG Rarity and PR Tapster. "Nonclassical effects in parametric downconversion". In: *Photons and Quantum Fluctuations*. CRC Press, 2020, pp. 122–150.

[105] Agata M Brańczyk. "Hong-ou-mandel interference". In: *arXiv preprint arXiv:1711.00080* (2017).

[106] Edward B Flagg et al. "Interference of single photons from two separate semiconductor quantum dots". In: *Physical Review Letters* 104.13 (2010), p. 137401.

[107] Kaoru Sanaka et al. "Indistinguishable photons from independent semiconductor nanostructures". In: *Physical Review Letters* 103.5 (2009), p. 053601.

[108] Rainer Kaltenbaek et al. "Experimental interference of independent photons". In: *Physical review letters* 96.24 (2006), p. 240502.

[109] Benjamin Vest et al. "Anti-coalescence of bosons on a lossy beam splitter". In: *Science* 356.6345 (2017), pp. 1373–1376.

[110] Asher Peres. "How the no-cloning theorem got its name". In: *Fortschritte der Physik: Progress of Physics* 51.4-5 (2003), pp. 458–461.

[111] Tian-Ming Zhao et al. "Entangling different-color photons via time-resolved measurement and active feed forward". In: *Physical Review Letters* 112.10 (2014), p. 103602.

[112] Keiichi Edamatsu, Ryosuke Shimizu, and Tadashi Itoh. "Measurement of the photonic de Broglie wavelength of entangled photon pairs generated by spontaneous parametric down-conversion". In: *Physical review letters* 89.21 (2002), p. 213601.

[113] Kevin T McCusker and Paul G Kwiat. "Efficient optical quantum state engineering". In: *Physical review letters* 103.16 (2009), p. 163602.

[114] Ashley Lyons et al. "How fast is a twisted photon?" In: *Optica* 5.6 (2018), pp. 682–686.

[115] Grace Richard et al. “Twisting waves increase the visibility of nonlinear behaviour”. In: *New Journal of Physics* 22.6 (2020), p. 063021.

[116] Frédéric Bouchard et al. “Observation of subluminal twisted light in vacuum”. In: *Optica* 3.4 (2016), pp. 351–354.

[117] Daniel Giovannini et al. “Spatially structured photons that travel in free space slower than the speed of light”. In: *Science* 347.6224 (2015), pp. 857–860.

[118] Magued B Nasr et al. “Demonstration of dispersion-canceled quantum-optical coherence tomography”. In: *Physical review letters* 91.8 (2003), p. 083601.

[119] Magued B Nasr et al. “Dispersion-cancelled and dispersion-sensitive quantum optical coherence tomography”. In: *Optics express* 12.7 (2004), pp. 1353–1362.

[120] Dorilian Lopez-Mago and Lukas Novotny. “Quantum-optical coherence tomography with collinear entangled photons”. In: *Optics letters* 37.19 (2012), pp. 4077–4079.

[121] Ayman F Abouraddy et al. “Quantum-optical coherence tomography with dispersion cancellation”. In: *Physical Review A* 65.5 (2002), p. 053817.

[122] Julian Hofmann et al. “Heralded entanglement between widely separated atoms”. In: *Science* 337.6090 (2012), pp. 72–75.

[123] XuBo Zou, K Pahlke, and W Mathis. “Teleportation implementation of non-deterministic quantum logic operations by using linear optical elements”. In: *Physical Review A* 65.6 (2002), p. 064305.

[124] Emanuel Knill. “Quantum gates using linear optics and postselection”. In: *Physical Review A* 66.5 (2002), p. 052306.

[125] Stefan Scheel et al. “Quantum gates and decoherence”. In: *Quantum Coherence: From Quarks to Solids* (2006), pp. 47–81.

[126] Ryo Okamoto et al. "Realization of a Knill-Laflamme-Milburn controlled-NOT photonic quantum circuit combining effective optical nonlinearities". In: *Proceedings of the National Academy of Sciences* 108.25 (2011), pp. 10067–10071.

[127] Paul G Kwiat et al. "New high-intensity source of polarization-entangled photon pairs". In: *Physical Review Letters* 75.24 (1995), p. 4337.

[128] Nicolas Gisin and Rob Thew. "Quantum communication". In: *Nature photonics* 1.3 (2007), pp. 165–171.

[129] Sandeep Singh et al. "Near-video frame rate quantum sensing using Hong-Ou-Mandel interferometry". In: *arXive* (2023).

[130] K Muhammed Shafi et al. "Multi-bit quantum random number generator from path-entangled single photons". In: *arXiv preprint arXiv:2202.10933* (2022).

[131] Ilhwan Kim, Donghwa Lee, and Kwang Jo Lee. "Numerical investigation of high-purity polarization-entangled photon-pair generation in non-poled KTP isomorphs". In: *Applied Sciences* 11.2 (2021), p. 565.

[132] Masoud Ghalaii and Stefano Pirandola. "Quantum communications in a moderate-to-strong turbulent space". In: *Communications Physics* 5.1 (2022), p. 38.

[133] Pablo Yepiz-Graciano et al. "Quantum Optical Coherence Microscopy for Bioimaging Applications". In: *Phys. Rev. Appl.* 18 (3 2022), p. 034060.

[134] Adrià Sansa Perna et al. "Visible-wavelength polarization-entangled photon source for quantum communication and imaging". In: *Applied Physics Letters* 120.7 (2022), p. 074001.

[135] A Halevy et al. "The biaxial nonlinear crystal BiB 3 O 6 as a polarization entangled photon source using non-collinear type-II parametric down-conversion". In: *Optics Express* 19.21 (2011), pp. 20420–20434.

[136] Aitor Villar, Alexander Lohrmann, and Alexander Ling. "Experimental entangled photon pair generation using crystals with parallel optical axes". In: *Optics express* 26.10 (2018), pp. 12396–12402.

[137] Heonoh Kim, Osung Kwon, and Han Seb Moon. “Pulsed Sagnac source of polarization-entangled photon pairs in telecommunication band”. In: *Scientific reports* 9.1 (2019), p. 5031.

[138] Shin Arahira, Tadashi Kishimoto, and Hitoshi Murai. “1.5-μm band polarization entangled photon-pair source with variable Bell states”. In: *Optics express* 20.9 (2012), pp. 9862–9875.

[139] Nicolas Schwaller et al. “Optimizing the coupling efficiency of spontaneous parametric down-conversion photon pairs into single-mode fibers”. In: *Phys. Rev. A* 106 (4 2022), p. 043719.

[140] M. V. Jabir, Manoj Apurv Chaitanya N.and A. Aadhi, and G. K. Samanta. “Generation of “perfect” vortex of variable size and its effect in angular spectrum of the down-converted photons”. In: *Scientific Reports* 6.1 (2017), p. 21877.

[141] Gregor Weihs et al. “Violation of Bell’s inequality under strict Einstein locality conditions”. In: *Physical Review Letters* 81.23 (1998), p. 5039.

[142] H-J Briegel et al. “Quantum repeaters: the role of imperfect local operations in quantum communication”. In: *Physical Review Letters* 81.26 (1998), p. 5932.

[143] Grégoire Ribordy et al. “Long-distance entanglement-based quantum key distribution”. In: *Physical Review A* 63.1 (2000), p. 012309.

[144] AV Sergienko and GS Jaeger. “Quantum information processing and precise optical measurement with entangled-photon pairs”. In: *Contemporary Physics* 44.4 (2003), pp. 341–356.

[145] Xiaojiong Chen et al. “Quantum entanglement on photonic chips: a review”. In: *Advanced Photonics* 3.6 (2021), p. 064002.

[146] Yin Juan et al. “Entanglement-based secure quantum cryptography over 1,120 kilometres”. In: *Nature* 582.7813 (2020), pp. 501–505.

[147] Paul G. Kwiat et al. “Ultrabright source of polarization-entangled photons”. In: *Phys. Rev. A* 60 (2 Aug. 1999), R773–R776.

[148] Marco Fiorentino et al. "Spontaneous parametric down-conversion in periodically poled KTP waveguides and bulk crystals". In: *Opt. Express* 15.12 (June 2007), pp. 7479–7488.

[149] M. V. Jabir, Manoj Apurv Chaitanya N.and Mathew, and G. K. Samanta. "Direct transfer of classical non-separable states into hybrid entangled two photon states". In: *Scientific Reports* 7.1 (2017), p. 7331.

[150] Fabian Steinlechner et al. "Efficient heralding of polarization-entangled photons from type-0 and type-II spontaneous parametric downconversion in periodically poled KTiOPO4". In: *J. Opt. Soc. Am. B* 31.9 (Sept. 2014), pp. 2068–2076.

[151] Alessandro Fedrizzi et al. "A wavelength-tunable fiber-coupled source of narrowband entangled photons". In: *Opt. Express* 15.23 (Nov. 2007), pp. 15377–15386.

[152] Xin-Yi Pan et al. "Temperature insensitive type II quasi-phasematched spontaneous parametric downconversion". In: *Applied Physics Letters* 119.2 (2021), p. 021107.

[153] Guang-Wen Huo et al. "Optimizing the phase-matching parameters of a BIBO crystal for ultrafast spontaneous parametric down conversion". In: *Photonics and Optoelectronics Meetings (POEM) 2011: Optoelectronic Devices and Integration*. Vol. 8333. SPIE. 2012, pp. 261–270.

[154] Andreas Christ et al. "Parametric down-conversion". In: *Experimental Methods in the Physical Sciences*. Vol. 45. Elsevier, 2013, pp. 351–410.

[155] Bedington Robert, Arrazola Juan Miguel, and Ling Alexander. "Progress in satellite quantum key distribution". In: *npj Quantum Information* 3.1 (2017), pp. 1–13.

[156] Kiyoshi Kato and Eiko Takaoka. "Sellmeier and thermo-optic dispersion formulas for KTP". In: *Appl. Opt.* 41.24 (Aug. 2002), pp. 5040–5044.

[157] H. Hellwig, J. Liebertz, and L. Bohatý. "Linear optical properties of the monoclinic bismuth borate BiB3O6". In: *Journal of Applied Physics* 88.1 (2000), pp. 240–244.

[158] A Srinivasa Rao and GK Samanta. "On-axis intensity modulation-free, segmented, zero-order Bessel beams with tunable ranges". In: *Optics Letters* 43.13 (2018), pp. 3029–3032.

[159] Pravin Vaity and Leslie Rusch. "Perfect vortex beam: Fourier transformation of a Bessel beam". In: *Optics letters* 40.4 (2015), pp. 597–600.

[160] J. Goodman. *Laser diode modulation and noise*. Vol. 3rd Edn. Roberts and company publishers, 2004.

[161] Jonathan Pinnell, Valeria Rodríguez-Fajardo, and Andrew Forbes. "How perfect are perfect vortex beams?" In: *Opt. Lett.* 44.22 (Nov. 2019), pp. 5614–5617.

[162] Salla Gangi Reddy et al. "Divergence of optical vortex beams". In: *Appl. Opt.* 54.22 (Aug. 2015), pp. 6690–6693.

[163] Fabio Antonio Bovino et al. "Effective fiber-coupling of entangled photons for quantum communication". In: *Optics Communications* 227.4-6 (2003), pp. 343–348.

[164] Ali Anwar et al. "Selecting the pre-detection characteristics for fiber coupling of parametric down-converted biphoton modes". In: *Optics Communications* 382 (2017), pp. 219–224.

[165] Brigitta Septriani et al. "Thick-crystal regime in photon pair sources". In: *Optica* 3.3 (2016), pp. 347–350.

[166] Daniel F. V. James et al. "Measurement of qubits". In: *Phys. Rev. A* 64 (5 Oct. 2001), p. 052312.

[167] Ana Predojević, Stephanie Grabher, and Gregor Weihs. "Pulsed Sagnac source of polarization entangled photon pairs". In: *Opt. Express* 20.22 (Oct. 2012), pp. 25022–25029.

[168] Wakana Ueno et al. “Entangled photon generation in two-period quasi-phase-matched parametric down-conversion”. In: *Optics Express* 20.5 (2012), pp. 5508–5517.

[169] Paulina S Kuo et al. “Characterization of type-II spontaneous parametric down-conversion in domain-engineered PPLN”. In: *Advances in Photonics of Quantum Computing, Memory, and Communication IX*. Vol. 9762. SPIE. 2016, pp. 108–116.

[170] Ke Bian et al. “Nanoscale electric-field imaging based on a quantum sensor and its charge-state control under ambient condition”. In: *Nature Communications* 12.1 (2021), p. 2457.

[171] Moeta Tsukamoto et al. “Accurate magnetic field imaging using nanodiamond quantum sensors enhanced by machine learning”. In: *Scientific Reports* 12.1 (2022), p. 13942.

[172] J Hendricks et al. “The emerging field of quantum based measurements for pressure, vacuum and beyond”. In: *journal of physics: conference proceedings* 1065.16 (2018), p. 162017.

[173] Kosuke Kakuyanagi et al. “Submicrometer-scale temperature sensing using quantum coherence of a superconducting qubit”. In: *New Journal of Physics* (2023).

[174] Lan Shi et al. “Quantum effect-based flexible and transparent pessure sensors with ultrahigh sensitivity and sensing density”. In: *Nature Communications* 11.1 (2020), p. 3529.

[175] C. L. Degen, F. Reinhard, and P. Cappellaro. “Quantum sensing”. In: *Rev. Mod. Phys.* 89 (3 2017), p. 035002.

[176] Aephraim M. Steinberg, Paul G. Kwiat, and Raymond Y. Chiao. “Dispersion cancellation and high-resolution time measurements in a fourth-order optical interferometer”. In: *Phys. Rev. A* 45 (9 1992), pp. 6659–6665.

[177] Katiúscia N Cassemiro, Kaisa Laiho, and Christine Silberhorn. “Accessing the purity of a single photon by the width of the Hong–Ou–Mandel interference”. In: *New Journal of Physics* 12.11 (2010), p. 113052.

[178] Ashley Lyons et al. “Attosecond-resolution hong-ou-mandel interferometry”. In: *Science advances* 4.5 (2018), eaap9416.

[179] Yuanyuan Chen et al. “Hong-Ou-Mandel interferometry on a biphoton beat note”. In: *npj Quantum Information* 5.1 (2019), p. 43.

[180] Michał Lipka and Michał Parniak. “Single-photon hologram of a zero-area pulse”. In: *Physical Review Letters* 127.16 (2021), p. 163601.

[181] N. Fabre and S. Felicetti. “Parameter estimation of time and frequency shifts with generalized Hong-Ou-Mandel interferometry”. In: *Phys. Rev. A* 104 (2 2021), p. 022208.

[182] Sara Restuccia et al. “Photon bunching in a rotating reference frame”. In: *Physical Review Letters* 123.11 (2019), p. 110401.

[183] C Radhakrishna Rao. “Information and the accuracy attainable in the estimation of statistical parameters”. In: *Reson. J. Sci. Educ* 20 (1945), pp. 78–90.

[184] Harald Cramér. *Mathematical methods of statistics*. Vol. 26. Princeton university press, 1999.

[185] Natapon Harnchaiwat et al. “Tracking the polarisation state of light via Hong-Ou-Mandel interferometry”. In: *Optics express* 28.2 (2020), pp. 2210–2220.

[186] Spencer J Johnson et al. “Toward vibration measurement via frequency-entangled two-photon interferometry”. In: *Quantum Sensing, Imaging, and Precision Metrology*. Vol. 12447. SPIE. 2023, pp. 263–268.

[187] Kyle M Jordan, Raphael A Abrahao, and Jeff S Lundeen. “Quantum metrology timing limits of the Hong-Ou-Mandel interferometer and of general two-photon measurements”. In: *Physical Review A* 106.6 (2022), p. 063715.

[188] Danilo Triggiani, Giorgos Psaroudis, and Vincenzo Tamma. "Ultimate Quantum Sensitivity in the Estimation of the Delay between two Interfering Photons through Frequency-Resolving Sampling". In: *Physical Review Applied* 19.4 (2023), p. 044068.

[189] Hannah Scott et al. "Beyond coincidence in Hong-Ou-Mandel interferometry". In: *Phys. Rev. A* 102 (3 2020), p. 033714.

[190] Hannah Scott et al. "Noise limits on two-photon interferometric sensing". In: *Phys. Rev. A* 104 (5 2021), p. 053704.

[191] DN Klyshko. "Coherent photon decay in a nonlinear medium". In: *ZhETF Pisma Redaktsiiu* 6 (1967), p. 490.

[192] M Ebrahimzadeh and MH Dunn. "Optical parametric oscillators". In: *OSA Handbook of Optics* 4 (2001), pp. 22–1.

[193] Ritwick Das et al. "Broadband, high-power, continuous-wave, mid-infrared source using extended phase-matching bandwidth in MgO:PPLN". In: *Opt. Lett.* 34.24 (2009), pp. 3836–3838.

[194] Changjia Chen et al. "Broadband fiber-based entangled photon-pair source at telecom O-band". In: *Optics Letters* 46.6 (2021), pp. 1261–1264.

[195] Byoung S Ham. "Coherence interpretation of the Hong-Ou-Mandel effect". In: *arXiv preprint arXiv:2203.13983* (2022).

[196] Pablo Yepiz-Graciano et al. "Spectrally resolved Hong–Ou–Mandel interferometry for quantum-optical coherence tomography". In: *Photonics Research* 8.6 (2020), pp. 1023–1034.

[197] Daniel Ljunggren and Maria Tengner. "Optimal focusing for maximal collection of entangled narrow-band photon pairs into single-mode fibers". In: *Physical Review A* 72.6 (2005), p. 062301.

[198] Robert W Boyd. *Nonlinear optics*. Academic press, 2020.

[199] Roberto Ramirez-Alarcon, Hector Cruz-Ramirez, and Alfred B U'Ren. "Effects of crystal length on the angular spectrum of spontaneous parametric down-conversion photon pairs". In: *Laser Physics* 23.5 (2013), p. 055204.

[200] Magued B. Nasr et al. "Ultrabroadband Biphotons Generated via Chirped Quasi-Phase-Matched Optical Parametric Down-Conversion". In: *Phys. Rev. Lett.* 100 (18 May 2008), p. 183601.

[201] Miaolei Zhou et al. "High precise fuzzy control for piezoelectric direct drive electro-hydraulic servo valve". In: *Journal of Advanced Mechanical Design, Systems, and Manufacturing* 6.7 (2012), pp. 1154–1167.

[202] Dariusz Grzybek and Andrzej Sioma. "Creep Phenomenon in a Multiple-Input Single-Output Control System of a Piezoelectric Bimorph Actuator". In: *Energies* 15.21 (2022), p. 8267.

[203] Laurent Vivien and Lorenzo Pavesi. *Handbook of silicon photonics*. Taylor & Francis, 2016.

[204] Eric Dulkeith et al. "Group index and group velocity dispersion in silicon-on-insulator photonic wires". In: *Optics express* 14.9 (2006), pp. 3853–3863.

[205] Dominik G Rabus. *Integrated ring resonators*. Springer, 2007.

[206] Haitao Zhou et al. "Hydrothermal growth of KTiOPO4 crystal for electro-optical application". In: *Light: Science & Applications* 12.1 (2023), pp. 1–20.

[207] Govindhan Dhanaraj et al. *Springer handbook of crystal growth*. Vol. 2. Springer, 2010.

[208] Venkata R Miriampally. "2D Optical Fiber Wave Guide Design for Multi Haul Applications". In: *International Journal of Informatics and Communication Technology (IJICT)* 5.3 (2016), pp. 94–105.

[209] Shyam Singh. "Refractive index measurement and its applications". In: *Physica Scripta* 65.2 (2002), p. 167.

[210] Andrew D Yablon. "Multifocus tomographic algorithm for measuring optically thick specimens". In: *Optics Letters* 38.21 (2013), pp. 4393–4396.

[211] S Manjooran et al. “Phase-matching properties of PPKTP, MgO: PPSLT and MgO: PPcLN for ultrafast optical parametric oscillation in the visible and near-infrared ranges with green pump”. In: *Laser Physics* 22 (2012), pp. 1325–1330.

[212] Mikhail N. Polyanskiy. *Refractive index database*. Accessed on 2023-07-14.

[213] Fuxi Gan. “Optical properties of fluoride glasses: a review”. In: *Journal of Non-Crystalline Solids* 184 (1995), pp. 9–20. ISSN: 0022-3093.

[214] HB Lin et al. “Extended Sellmeier equation for the extraordinary refractive index of 5% MgO-doped congruent LiNbO3 at high temperature”. In: *AIP Advances* 7.9 (2017), p. 095201.

[215] Shai Emanueli and Ady Arie. “Temperature-dependent dispersion equations for KTiOPO 4 and KTiOAsO 4”. In: *Applied optics* 42.33 (2003), pp. 6661–6665.